

Université de Québec
Institut National de la Recherche Scientifique
Énergie Matériaux Télécommunications

**THE INVESTIGATIONS OF HOST/GUEST
STRUCTURES BASED ON COVALENT ORGANIC
FRAMEWORKS AT SOLUTION/SOLID INTERFACES**

Daling Cui

Thèse présentée pour l'obtention du grade de
Philosophiæ Doctor (Ph.D.)
en Sciences de l'énergie et des matériaux

Members Du Jury

Director of research: Prof. Federico Rosei, INRS-EMT, Université of Québec
Examineur interne: Prof. Andreas Ruediger, INRS-EMT, Université of Québec
Examineur externe: Prof. Louis Cuccia, Université de Montréal
Examineur externe: Prof. Antonella Badia, Université Concordia

ABSTRACT

Covalent organic frameworks (COFs) have gained significant attention in many applications due to their porous crystalline structures with high architectural and chemical robustness and customized topologies. A high-quality extended two-dimensional (2D) hexagonal porous COF-1 network can be obtained through cyclocondensation of three 1,4-benzenediboronic acid (BDBA) monomers by using excess water as the chemical-equilibrium-manipulating agent on a highly oriented pyrolytic graphite (HOPG) substrate. The surface-confined COF-1 can be used as template to recognize different guest molecules, allowing formation of a host/guest (H/G) structure. The intrinsic features of H/G structures lead to their wide applications in molecular recognition, catalysis, gas storage, separation and directed crystallization. Driven by the potential applications, the present work in this thesis concentrates on the preparation and properties of H/G structures based on COF-1 templates at the solution/solid interface.

Firstly, scanning tunneling microscopy (STM) images show that the surface-supported two-dimensional COF-1 can act as a host architecture for C₆₀ fullerene molecules, predictably trapping the molecules under a range of conditions. C₆₀ adsorbs in the COF-1 template in two different sites, the top-site (T) and the pore-site (P). The fullerenes occupy the COF-1 lattice at the heptanoic acid/HOPG interface, and in dried films of the COF-1/fullerene network that can be synthesized through either

drop-deposition of fullerene solution or by a dipstick-type synthesis in which the surface-supported COF-1 is briefly dipped into the fullerene solution.

COF-1 can be synthesized from different solvents. When 1,2,4-trichlorobenzene (TCB) is used, STM images reveal the adsorption of TCB in the hexagonal pore of COF-1 template at TCB/HOPG interface. A well-defined loop boundary formed by a chain of pentagonal and heptagonal pores allowed us to investigate the effect of pore shape and size on TCB adsorption, suggesting that both geometrical and size effects are important in binding the TCB. When both C_{60} and TCB are present at the TCB/HOPG interface, TCB molecules are selectively trapped in the pore-site, whereas fullerenes adsorb on the top-site of COF-1. While the former structure is stabilized by Cl...H hydrogen bonds, the latter is controlled by van der Waals (vdW) interactions. These results suggest that surface-supported 2D porous COFs can selectively bind different molecules at specific sites *via* different types of interactions and COFs may offer a powerful platform for the recognition and patterning of guest molecules.

Moreover, a 2D COF-1 can template solution-processed C_{60} guest molecules to form several solvent-dependent structural arrangements and morphologies *via* a 2D to 3D growth process. When TCB is used as solvent, C_{60} molecules form a template-defined close packed structure. When heptanoic acid is used as solvent, a range of lower density architectures that deviate from the template-defined close packing are observed. This difference is attributed to the co-adsorption of the heptanoic acid

solvent molecules, which is only achieved in the presence of the template. This work demonstrates the possibility to precisely control molecular self-assembly to form designed 3-dimensional (3D) structures through the synergistic combination of template and solvent effects.

ACKNOWLEDGEMENTS

Foremost, I would like to thank my supervisor, Prof. Federico Rosei for the continuous support of my Ph.D study and research activities. He has created a warm and free research environment allowing me to explore my interest in a forefront and fascinating scientific field. Without whom, I could not have made it possible. Being able to study under his supervision is one of the most important achievements in my life.

I would like also to express my sincere gratitude to Dr. Jennifer M. Macleod and Dr. Maryam Ebrahimi. They have made vital contributions to most of my work and given me invaluable help and comments on my research and thesis writing.

I also acknowledge Prof. Dmitrii Perepichka, from McGill University, for the comments and discussions and Dr. Catalin Harnagea for the assistance in the maintenance of STM facilities and Dr. Josh Lipton-Duffin for the design and production of the reactor.

I would like to also thank my colleagues, Fabrizio De Marchi and Gianluca Galeotti, for their help throughout the duration of my Ph.D. I would like to thank Sarah Xing for the translation of french section.

I am grateful to all my friends who have made the last five years so enjoyable: Shun Li, Yue Huang, Wei Huang, Haiguang Zhao, Xin Chai, Fan Yang, Qingzhe Zhang, Mengyang Fan, Joyprokash Chakrabartty, Chao Wang, Qiliang Wei, Xin Tong, Yufeng Zhou *et al.*

Finally, I thank to the departmental and technical staff at INRS-EMT.

CONTENTS

ABSTRACT.....	I
ACKNOWLEDGEMENTS.....	IV
LIST OF TABLES	IX
LIST OF FIGURES	X
Chapter 1. Introduction	1
1.1. Molecular self-assembly on 2D surfaces.....	1
1.2. Covalent Organic Frameworks.....	12
1.3. Host/Guest chemistry based on 2D templates	17
1.4. Thesis objectives and organizations	25
Chapter 2. Experimental techniques	27
2.1. COF synthesis on HOPG and guest molecule.....	27
2.2. Scanning Tunneling Microscopy (STM).....	31
Chapter 3. Solution and air stable host/guest architectures from a single layer covalent organic framework.....	38
3.1. Introduction	38
3.2. Results and discussions	40
3.3. Conclusions and perspectives.....	47
3.4. Experimental methods.....	48
3.5. Calculations	50
Chapter 4. Selective binding in different adsorption sites of a 2D covalent organic	

framework template.....	53
4.1. Introduction	53
4.2. Results and discussions	55
4.3. Conclusions and perspectives.....	64
4.4. Experimental methods.....	65
4.5. Calculations	66
Chapter 5. Control of fullerene crystallization from 2D to 3D through combined solvent and template effects	71
5.1. Introduction	71
5.2. Results and discussions	75
5.2.1. C ₆₀ self-assembly at heptanoic acid/HOPG interface	77
5.2.2. Identification of the solvent co-adsorption effect	86
5.2.3. Additional solvent effects on film packing and morphology.....	96
5.3. Conclusions and perspectives.....	100
5.4. Experimental methods.....	101
5.5. Calculations	103
5.5.1. COF-1/graphene bilayer.....	104
5.5.2. C ₆₀ molecules adsorbed on COF-1/graphene bilayer.....	105
5.5.3. Bader charge calculation.....	111
5.5.4. Solvent molecule (heptanoic acid) adsorption on COF-1/graphene bilayer.....	111

5.5.5. The co-adsorption of heptanoic acid in shift structures and template defined close packing structures	113
Chapter 6. Conclusions and perspectives.....	116
6.1. Conclusions	116
6.2. Perspectives	119
Appendix A Abbreviations.....	122
Appendix B RÉSUMÉ.....	125
L'Introduction	125
Résultats et discussions.....	131
Conclusions.....	150
References	153

LIST OF TABLES

Table 1.1 Intermolecular interactions of self-assembly ²⁴	7
Table 4.1 Van der Waals radii ¹⁴⁰ and calculated inter-atom distance*	70
Table 5.1 The adsorption and total cohesive energy of 2D-to-3D growth of C ₆₀ (1st, 2nd, and 3rd layer of C ₆₀ formed of one, two, and three C ₆₀ molecular layers, respectively) on COF-1/graphene bilayer	110
Table 5.2 The Bader charge for top-site and shift structures	111
Table 5.3 Adsorption energy of one heptanoic acid at three adsorption sites	112
Table 5.4 Total cohesive energies of T-layer C ₆₀ , shift structures and template-defined structures with co-adsorption of heptanoic acid molecules	114

LIST OF FIGURES

Figure 1.1 (a) Schematic representation of change in the density of state in one band according to the size of material (metal and semiconductor). (b) The density of state in one band of a semiconductor as a function of dimension. Reproduced with permission from the Science. ⁴2

Figure 1.2 Two methods (top-down vs bottom-up) to produce matter at the nanoscale. Top-down methods, such as lithography, writing or stamping, are used to define the desired features. The bottom-up techniques use self-processes to produce ordered patterns of supramolecular or solid-state architectures from the atomic to the mesoscopic scale. Reproduced with permission from the Nature Publishing Group. ⁵ .3

Figure 1.3 Schematic illustration of the possible 17 plane groups in 2D, describing the symmetry of monolayer molecular self-assembly. An arrow indicates each asymmetric unit, and unit cells are denoted with gray lines. Reproduced with the permission from American Chemical Society. ¹⁵5

Figure 1.4 (a) STM image of self-assembly of C₁₈ISA molecules at 1-octanol/graphite interface. The value of ΔL_1 corresponds to interdigitated C₁₈ISA, identical with the one in (c). The value of ΔL_2 corresponds to the width of the lamella formed by 1-octanol molecules. Image size is 10 × 10 nm². (b) Molecular model represents the area indicated in (a). The unit cell for 1-octanol molecules coadsorption in two-dimensional packing of C₁₈ISA molecules was proposed. (c) STM image of self-assembly of C₁₈ISA molecules at 1-phenyloctane /graphite interface. Image size is

$10.7 \times 10.7 \text{ nm}^2$. (d) Molecular model represents the area indicated in (c), showing no solvent coadsorption. Reproduced with the permission from American Chemical Society.³³ **9**

Figure 1.5 (a) (Top) The STM image and models for chickenwire structure of TMA. STM image was collected at the heptanoic acid/HOPG interface. Image size: $15 \times 15 \text{ nm}^2$. (Bottom) The STM image and models for flower structure of TMA. STM image was collected at the pentanoic acid/HOPG interface. Image size: $15 \times 15 \text{ nm}^2$.³⁸ (b) Schematic representation of the seeding process for the oblique pattern (left) and the chickenwire motif (right) with the BTB dimer as the repeating unit forming. The count represents the number of polar functional groups exposed to the solvent, and those in the brackets represent the number of BTB molecules involved in the assembly. (c) Schematic representation of the properties for the series of alkanolic acids from butanoic to nonanoic acid and the respective interfacial monolayer polymorphs. Reproduced with the permission from American Chemical Society.³⁷ **11**

Figure 1.6 (a) The “node” approach for synthesis of 2D COFs. Examples are given on the right: cyclocondensation of three boronic acids molecules and tetramerization of four 1,2,4,5-tetracyanobenzene (TCNB) molecules with one Fe atom. (b) The spacer approach for synthesis of 2D COFs according to the symmetries of builders. Corresponding examples are given on the right for the construction of 2D COFs: the condensation reaction between boronic acids and diols, the Schiff-based reaction, polyamide formation, polyimide formation, polyester condensation, Ullmann coupling,

*and Glaser coupling. Reproduced with the permission from Wiley.*⁴²13

Figure 1.7 *Enthalpic diagram showing the different transition states during polymerization reaction. The energies (in eV) are relative to the monomers. After each transition, a water molecule is released (arrows). Reproduced with the permission from Wiley.*⁴⁷15

Figure 1.8 *Synthesis of high-quality 2D COF-1 monolayer polymers. (a) BDBA monomer self-condenses onto crystalline metal surfaces in UHV to form COF-1 monolayer which containing various pentagonal and heptagonal ring defects (middle). The improvement in the order of the film can be initiated through annealing this film in a humid environment (right). (b) Pre-prepared COF-1 nanocrystals in solution were dropcasted onto HOPG surface (middle). Similar annealing can provide a monolayer with improved long-range order (right). Reproduced with the permission from the Nature Publishing Group.*⁵¹16

Figure 1.9 (a) *Schematic of conjugated oligothiophene macrocycle, which is intrinsically porous. (b) STM image of a monolayer of macrocycles on HOPG. The adsorption of C₆₀ is indicated with white arrow. Image area: 11.6 nm × 8.7 nm; Scanning conditions: V = -700 mV, I = 44 pA. (c) Calculated model of a closely packed monolayer of assembled template with intrinsic porous host molecules with a hexagonal arrangement. Inset picture exhibits side view of the calculated energy minimum conformation of a oligothiophene-C₆₀ complex. Reproduced with the permission from Wiley.*⁵⁴ (d) *Illustration of the TMA chickenwire host, which is*

extrinsically porous. TMA molecules are drawn with the vdW surfaces of the atoms. The extrinsic single cavity stabilized by hydrogen bonds is indicated in the right enlarged sketch. (e) STM constant current image of the TMA-C₆₀ host-guest structures. The diameter of the pores is 1.1 nm, and the unit cell of the hexagonal network is $a=b=1.6\pm0.1$ nm and $\gamma=60\pm1^\circ$ as depicted in the upper right corner. The adsorption of two C₆₀ molecules inside the pores of the TMA host network appear as bright protrusions. Image dimensions: 10×10 nm². Reproduced with the permission from American Chemical Society.⁵⁵18

Figure 1.10 *The chemical structures of the NN4A and guest molecules: (a) NN4A, (b) coronene, (c) C₆₀. (d) The STM image of coronene/C₆₀/NN4A ternary architecture at alternate bias and current. Image dimensions: 41×41 nm² The line at which the bias changed is marked by a green arrow. The scanning conditions of upper area and lower one are $I=1055$ pA, $V=516$ mV and $I=128$ pA, $V=968$ mV, respectively. (e) A molecular model of coronene and C₆₀ molecules co-adsorbed on NN4A networks. Reproduced with the permission from Wiley.⁶³21*

Figure 1.11 *Graphic representation of a FET chemical sensor.⁷¹22*

Figure 1.12 *(a) Schematic illustration of the random rhombus tiling formed by the terphenyl-3,3'',5,5''-tetracarboxylic (TPTC) acid framework. Different hexagonally ordered network of pores is highlighted by A-E. (b) STM image of TPTC network after a deposition of C₆₀. The locations of C₆₀ are visible as bright spots in the image and the underlying TPTC network is not visible. Scale bar: 16 nm; (c) STM image of*

*TPTC bilayer immediately collected after C₆₀ deposition. The co-adsorption structure of C₆₀ and bilayer TPTC framework can be identified. The first layer of TPTC framework is visible with an altered contrast and the second TPTC molecules appear with the long axis of the molecules as bright, rod-like features. Scale bar: 11 nm. (d) Schematic representation of the co-adsorption of C₆₀-bilayer structure consisting of two overlying pores of type A. Reproduced with the permission from the Nature Publishing Group.*⁷⁹**24**

Figure 2.1 (a) *The scheme of COF-1 and the chemical reaction for synthesizing template: self-condensation of BDBA monomers gives rise to 2D COF-1 template wherein defects are recovered through the reversible reaction that occurs in the presence of water. The scheme of the boroxine ring is enlarged in the inset circle.*⁸⁰ (b) *The schematic illustration of the setup of synthesizing COF-1 on HOPG substrate...***27**

Figure 2.2 *STM image of HOPG. Image dimensions: 4.2 × 4.2 nm². Tunneling conditions: V = -19 mV, I = 1000 pA. The hexagonal lattice constant of HOPG is 0.246 nm.*.....**29**

Figure 2.3 *Scheme of C₆₀ guest molecule.*.....**30**

Figure 2.4 *Schematic diagram of the scanning tunneling microscopy, produced by Michael Schmid and Grzegorz Pietrzak, and used under CC BY-SA 2.0 AT.***32**

Figure 2.5 *An illustration of STM mechanism: the one-dimensional metal-vacuum-metal tunneling junction. The sample (left) and the tip (right) are modeled as semi-infinite pieces of free-electron metal. The work function is*

represented as ϕ , defined as the minimum thermodynamic work required to remove an electron from the bulk to the vacuum level. Neglecting the thermal excitation, the Fermi level, E_F , is the upper limit of the occupied states in a bulk metal. Here, the work functions of tip and sample are assumed to be equal. The bias voltage leading to the realignment of Fermi levels of sample and tip is represent as eV . The spatial width of vacuum (energy barrier) is indicated as S .⁹⁰33

Figure 2.6 The Bardeen approach of tunneling theory.⁹⁰35

Figure 3.1 (a) Image revealing molecular resolution of the COF-1 structure (top) and atomic resolution of the underlying HOPG (bottom). Image conditions: bias voltage $V=-800$ mV, tunneling current $I=100$ pA (top); $V=-19$ mV, $I=1000$ pA (bottom). (b) Autocorrelation of the image shown in (a). The small lattice (HOPG) and the large lattice (COF-1) have a clear commensurate relationship. The COF-1 aligns with the HOPG along both lattice directions, with each unit vector having an identical length of six HOPG lattice constants.40

Figure 3.2 H/G structures at the solution/solid interface. The images in (a) and (b) show the observed fullerene adsorption geometries, denoted as top site and pore site, respectively. The structures in (c) and (d) show proposed models for these adsorption sites. Scanning conditions: bias voltage $V=-800$ mV, tunneling current $I=100$ pA. Image widths (a) 5.3 nm and (b) 7.7 nm.42

Figure 3.3 Consecutive STM images of H/G architecture: (a) the starting geometry with a small domain of C_{60} guest molecules inside the host template; (b) final

geometry in the same area with C_{60} molecules in a new distribution which demonstrates a transfer of guest molecules induced by STM tip. Image width: 8.5 nm.

Scanning conditions: bias voltage $V=-800$ mV, tunneling current $I=100$ pA.....**44**

Figure 3.4 H/G structures at the air/solid interface. The images in (a) and (b) show top site adsorption and image in (c) shows pore site adsorption, respectively. (a) shows an isolated fullerene molecule and (b) is a stable domain of top site adsorption of C_{60} molecules at air/solid interface. Imaging parameters: voltage $V=-800$ mV, tunneling current $I=100$ pA. Image width: (a) 5.6 nm (b) 17.2 nm (c) 5.4 nm.....**45**

Figure 3.5 Schematic illustration of dipstick synthesis of COF-1/fullerene H/G structure. The image in (b) shows the as-synthesized COF-1 on HOPG. Following immersion into a solution of C_{60} in heptanoic acid (a) and subsequent drying, STM images like that in (c) reveal COF-1 populated with C_{60} guest molecules. Imaging parameters: voltage $V=-800$ mV, tunneling current $I=100$ pA.....**46**

Figure 3.6 molecular mechanics calculated geometries for pore site adsorption (a), top site adsorption over a phenyl ring (b) and top site adsorption over a boroxine ring (c). Oxygen atoms are represented by red, carbon atoms (fullerene and COFs) are represented by blue and carbon atoms (graphite) are represented by green.....**52**

Figure 4.1 (a) STM image of COF-1 synthesized in TCB, collected at the air/solid interface. Image width: 60 nm. Scanning conditions: $V= -1000$ mV, $I= 100$ pA. (b) STM image of COF-1 synthesized in heptanoic acid, collected at the interface of

heptanoic acid and HOPG. A small domain of Phase II is marked by black circle.

Image width: 60 nm. Scanning conditions: $V = -800$ mV, $I = 100$ pA.55

Figure 4.2 (a) COF-1 STM image showing the grain boundary consisting of pentagon and heptagon rings, connecting two domains rotated by $30 \pm 1^\circ$ with respect to one another, as shown by the dashed and solid black lines. The image was collected at the interface of TCB and HOPG. Image width: 15 nm. Scanning conditions: $V = -1000$ mV, $I = 100$ pA. (b) The epitaxy of COF-1 and HOPG at grain boundary region. Phase I: $a_1 = a_2 = 1.476$ nm; Phase II: $b_1 = b_2 = 1.42$ nm. Image width: 9.6 nm. (c) Schematic structure of the rotational grain boundary identified in (b), i.e., a loop defect with C_6 symmetry. Five- and sevenfold rings are shaded by blue and green, respectively. (d) Line profile of the measured height along the black solid line in (a). The positions of benzene rings in COF-1 are marked as \times and the positions of adsorbed TCB molecules are marked as \circ56

Figure 4.3 (a) The detailed STM image of one TCB molecule adsorbing into the hexagonal ring formed by COF-1. Image width: 2.1 nm. Scanning conditions: $V = -1000$ mV, $I = 100$ pA. (b) DFT-calculated structure of one TCB in hexagonal pore (M06-2X/LANL2DZ). Dashed blue and black lines represent the interactions of Cl...H and Cl...O, respectively.58

Figure 4.4 (a-c) The sequential collection of STM images showing the evolution of adsorption of TCB in the grain boundary defects. Different geometries are marked by different dashed color circle: heptagonal ring (green circle); hexagonal ring (red

circle); pentagonal ring (blue circle). Image width: 5.8 nm. Scanning conditions: $V = -1000$ mV, $I = 100$ pA.60

Figure 4.5 (a) The top-site selective formation in $C_{60}/COF-1$ system. Image width: 12 nm. Scanning conditions: $V = -800$ mV, $I = 100$ pA. (b) Schematic image of top-site selective formation in $C_{60}/COF-1$ system. The shaded blue circles over benzene rings represent the closed packed background in STM image. Top-site C_{60} molecules are placed over boroxine rings, corresponding to the large bright spots in (a).62

Figure 4.6 (a) Molecular electrostatic potential (ESP) map (M06-2X/LANL2DZ) for isolated TCB in the gas phase (3D view). (b) Molecular ESP map of optimized geometry (M06-2X/LANL2DZ) for TCB in COF-1 hexagonal pore. The ESP maps for a and b are expressed in atomic units (a.u., Rydberg/e) on 0.0004 e/Bohr³ and 0.004 e/Bohr³ isodensity surfaces, respectively. The color scale from blue (+ve) to red (-ve) spans the following ranges: ± 0.01 a.u. for both a and b. (c) Optimized geometry of one TCB in hexagonal pore (M06-2X/LANL2DZ), with marking the distances of Cl...H (dashed blue line) interatomic contacts. (Only showing the distances less than the sum of the vdW radii for Cl...H contacts)67

Figure 4.7 Indicative geometry for TCB in pentagonal pore. All H...H distances between hydrogens on the TCB molecule and hydrogens on the COF-1 pore are below 2 vdW radii for hydrogen ($2r_H = 2.4$ Å),¹⁴⁰ suggesting that the TCB molecule cannot be accommodated in a planar adsorption geometry in the pentagonal pore.68

Figure 4.8 Optimized geometry for two TCB molecules in a heptagonal pore. This

geometry allows for Cl...H (dashed blue line) interactions between the TCB and the COF-1 pore as well as Cl...Cl (dashed green line) interactions between the two TCB molecules. However, bond distances for Cl...H interactions are shorter than expected (i.e., shorter than the optimized distances found for a single TCB in a hexagonal pore, see Table 4.1), and unfavourably short H...H (dashed brown line) interactions exist between hydrogen atoms on the TCB molecules and the COF-1 pore (i.e., distances shorter than $2r_{\text{H}}=2.4 \text{ \AA}$). These closer interactions suggest that perhaps the epitaxial heptagonal pore is expanded somewhat from the gas-phase dimensions reflected in this geometry. The inter-atom distances for Cl...Cl, Cl...H and H...H are marked accordingly. (Only showing those less than the sum of the vdW radii)69

Figure 5.1 (a) Sub-molecularly resolved COF-1 template STM image collected at air/solid interface. Tunnelling conditions: $V=-800 \text{ mV}$, $I=100 \text{ pA}$. Image dimensions: $7.1 \times 7.1 \text{ nm}^2$. (b) Schematic image of honeycomb COF-1 with unit cell shaded blue and a boroxine ring together with three neighbor benzenes specified with dashed black circle. DFT optimized top-site (c) and pore-site (d) positioning of a guest C_{60} molecule within the COF-1 host. The substrate graphene bilayer has been omitted for better visibility. Detailed simulation results are given in calculation section.75

Figure 5.2 (a) STM image with P-T bilayer structure collected at the heptanoic acid/HOPG interface. Tunnelling conditions: $V=-776 \text{ mV}$, $I=42.25 \text{ pA}$. Image dimensions: $19 \times 19 \text{ nm}^2$. (b) STM image collected at the heptanoic acid/HOPG interface showing quasi-HCP triple layer structure and $R1_{\text{T}}$ layer shifts in A and B

patterns. Tunnelling conditions: $V=-800$ mV, $I=33$ pA. Image dimensions: 15.4×15.4 nm². (c) The schematic image corresponding to (b). Different architectures are marked by indicators. (d) Model of the P-T bilayer. (e) Model of the quasi-HCP triple layer structure. The two fullerene molecules marked with “1” are adsorbed in the quasi-same position. (f) Models of the shift of a single R1_T layer molecule with respect to the T layer in A and B patterns. (g) The DFT calculated structure of A-pattern shift, as shown in top view and side view. The relative positions of T-site and R1 C₆₀ are specified in side view. For a better visualization, the radius of C₆₀ carbon atoms is enhanced.77

Figure 5.3 A comparison of quasi-HCP (left), HCP (middle) and standard-HCP (right). Similar arguments can also be assigned for the face-centred cubic (FCC) packing. The quasi-structure is associated with the shift behavior of R1 fullerenes (marked 1 in the orange circle) with respect to the given T-layer fullerene (marked 2). Note that, in the quasi-HCP and HCP here, the intralayer C₆₀ molecules are spaced with a distance of 1.476 nm. This is different from standard-HCP, where all the molecules are spaced in a distance of ~1 nm.¹⁶⁵ The standard-FCC close packing C₆₀ can be formed on bare HOPG, see Figure 5.10.79

Figure 5.4 STM images of a single R1 fullerene shift collected at heptanoic acid/solid interface, where the COF-1 lattice is represented by the black honeycomb, and the yellow and orange circles indicate T layer and R1 layer fullerene molecules respectively. (a) A-pattern shift. (b) B-pattern shift. (c) Geometry of the shifts, where

the epitaxial COF-1 lattice constant is $a=1.476$ nm according to our previous work.

(d) The collective assembly of R1 fullerenes, parallel-shift. Tunnelling conditions: $V=-800$ mV, $I=33$ pA. Image dimensions: 6.5×6.5 nm².**80**

Figure 5.5 (a) STM image collected at the heptanoic acid/HOPG interface. The black dashed line encloses a region of the crystal with one missing C₆₀ molecule. The inset image shows the plan view schematic of the black dashed box region, according to the parallel shift model. The white dashed line marks a rotated-shift region. Tunnelling conditions: $V=-800$ mV, $I=100$ pA. Image dimensions: 24.4×24.4 nm². (b) Detailed STM image collected at heptanoic acid/HOPG interface showing a moiré pattern caused by rotation of the R1 layer relative to the underlying T layer. Tunnelling conditions: $V=-800$ mV, $I=100$ pA. Image dimensions: 11.8×11.8 nm². (c) The schematic image corresponding to (b). Orange circles represent the R1 layer molecules and yellow circles represent the T layer molecules. (d) The schematic image of geometrical considerations of the region (spin centre) enclosed by the dashed box in image (c), showing the geometry of the rotation of the R1 layer relative to the T layer.....**81**

Figure 5.6 Moiré pattern of R1 layer rotated by $\theta = 26.746^\circ$ (indicated by lines at the bottom) with respect to the underlying T layer. The vectors of the Moiré pattern t_1 , t_2 are shown by arrows and labeled accordingly. The lattice vectors a_1 , a_2 of the underlying T monolayer are sketched at the lower right, where a magnification by a factor 3 is applied for better visibility. Specifically, the region of Figure 5.5b is

marked by colour of blue in a unit cell, where the centre of spin defined in Figure 5.5c is marked with orange triangle. The calculated model is available in experimental section.84

Figure 5.7 (a) STM image collected at heptanoic acid/HOPG interface showing multiple crystallization geometries for three layer structures. Tunnelling conditions: $V=-800$ mV, $I=200$ pA. Image dimensions: 17.3×17.3 nm². (b) The schematic of (a). (c) The schematic showing position of the R2 layer relative to the R1 layer. (d) The DFT optimized geometries of A-FCC and A-HCP. Schematic showing the positions of C₆₀ in the T layer (bottom), R1 layer (middle) and R2 layer (top) relative to each other for an R1 layer with A-pattern shift (e) and B-pattern shift (f).85

Figure 5.8 (a) STM image showing the co-adsorption of heptanoic acid and T-layer C₆₀ collected at the heptanoic acid/HOPG interface. Tunnelling conditions: $V=-1000$ mV, $I=50$ pA. Image dimensions: 12×12 nm². The hexagonal lattice represents the COF-1 template. A single missing C₆₀ is marked by a large black open circle. The features at the bottom of missing C₆₀ site are assigned as COF-1 template. Three small bright spots assigned as solvent molecules are marked by small black open circles; similar adsorption occurs throughout the lattice, but has not been indicated to allow clearer visualization of the contrast modulation associated with these features. One site without this small bright feature is marked by a black arrow. (b) Optimized structure of T-layer C₆₀ with co-adsorption of heptanoic acid at both P-site and T-site (See section 5.5). The T-site heptanoic acid molecules appear at each of the three

boroxine rings in the COF-1 template. Only one P-site adsorbed heptanoic acid appears per pore, consistent with the slightly off-centre adsorption of the T-site C_{60} molecule. For a better illustration of the model matching with the experimental data, scheme (b) has been modified from the actual DFT data by taking off the features missing from the STM image (a). (c) STM image collected at the supernatant (TCB)/HOPG interface. Image dimensions: $9.6 \times 5.4 \text{ nm}^2$. Tunnelling conditions: $V = -1000 \text{ mV}$, $I = 50 \text{ pA}$. Here, R1 C_{60} adsorbs in a template-defined close-packed geometry. (d) Schematic of (c) with TCB molecules in the pores of the COF-1 template. The STM images (e and f) showing the co-adsorption of heptanoic acid in T-layer C_{60} obtained in a same collection. (e) is the forward-scan image and (f) is the backward-scan image. Tunnelling conditions: $V = -1000 \text{ mV}$, $I = 50 \text{ pA}$. Image dimensions: $11.72 \times 11.72 \text{ nm}^2$. (g, h) are magnified images corresponding to the regions marked by dashed black squares in (e) and (f) respectively. Image dimensions: $2.8 \times 2.8 \text{ nm}^2$. The black arrows in the images indicate the direction of scan. (f) is also shown in (a).88

Figure 5.9 (a-c) Successive STM images of same region collected from the TCB supernatant/HOPG interface. Image dimensions: $80 \times 80 \text{ nm}^2$. Tunnelling conditions: $V = -1200 \text{ mV}$, $I = 50 \text{ pA}$. (d-f) Successive STM images of same region collected from the heptanoic acid supernatant/HOPG interface. Image dimensions: $60 \times 60 \text{ nm}^2$. Tunnelling conditions: $V = -800 \text{ mV}$, $I = 100 \text{ pA}$. The domain morphology of the C_{60} films in TCB varies with time, in contrast to the films formed from heptanoic acid. In

the latter (d-f), individual vacancies vary from image to image, but the overall domain structure and occupancy remains relatively constant.91

Figure 5.10 (a) XRD spectra of bare HOPG (black) and C₆₀ crystal on HOPG (red).

The peak at $2\theta = 10.8^\circ$ ($d \sim 0.82$ nm) corresponds to the (111) face of standard-FCC fullerene ($a = 1.42$ nm). This is also consistent with (002) of standard-HCP fullerene with $a = 1.00$ nm and $c = 1.64$ nm, but in this case we should also observe the weaker (001) reflection at 10.2° . The asterisk indicates the peak from HOPG.¹⁷⁴ (b) Scanning

electron microscopy image of an asymmetric C₆₀ hexagonal-shaped disk on bare HOPG, prepared by drop-deposition method with a solution (1.942×10^{-3} M) of C₆₀ in heptanoic acid.93

Figure 5.11 Schematically illustration of the control of fullerene crystallization from 2D to 3D through combined solvent and template effects.96

Figure 5.12 STM images collected from supernatant solutions of C₆₀. (a) STM image at the heptanoic acid supernatant/HOPG interface. Tunnelling conditions: $V = -1200$ mV, $I = 50$ pA. Image dimensions: 60×60 nm². (b) STM image at the TCB supernatant/HOPG interface. Tunnelling conditions: $I = 100$ pA, $V = -800$ mV. Image dimensions: 60×60 nm². (c) Domain size distribution of (b). The coverage (P) of C₆₀ in STM image is 55.4%.98

Figure 5.13 The optimized geometry of COF-1 on graphene bilayer.104

Figure 5.14 The DFT-calculated geometry for C₆₀ on COF-1/graphene bilayer. (a) C₆₀ over boroxine ring (T-layer), (b) C₆₀ over phenyl ring, (c) Pore-site C₆₀ (P-layer),

(d) P-T bilayer C₆₀.106

Figure 5.15 (a) Cartesian coordinate system for off-centred adsorption simulation, where origin is defined as the position of optimized pore-site. X and Y axes represent zigzag and armchair directions of COF-1 template. (b) The plot of energy change of different off-centred positions (along X and Y axes) with respect to optimized centred pore-site position (P-site Table 5.1, which gave -1.59 eV adsorption energy here under the accuracy described above). The distance of each step is 0.5 Å.107

Figure 5.16 The DFT calculated geometry of R1 layer C₆₀ on T layer/COF-1/graphene bilayer. (a) A-pattern shift. (b) B-pattern shift. (c) A- close packing. (d) B- close packing.....108

Figure 5.17 The DFT calculated geometry of R1 and R2 layer C₆₀ on T layer/COF-1/graphene bilayer. (a) A-FCC architecture. (b) A-HCP architecture. (c) B-FCC architecture. (d) B-HCP architecture.109

Figure 5.18 Optimized structures of adsorption of solvent molecules on COF-1/graphene bilayer. Heptanoic acid adsorbed at the pore-site (a), top phenyl-ring site (b) and top boroxine-ring site (c).113

Figure 5.19 Comparing A-pattern shift (a, b) and A-close packing (c, d) optimized structures in the absence and presence of heptanoic acid molecules (P- and T- sites). The structures shown in (a) and (c) are the same structure as Figure 5.16a and Figure 5.16c, respectively. The height of R1 C₆₀ in (b) is about 0.9 Å lower than (a), and that of (d) is about 3.0 Å higher than (c)..... 114

Figure 6.1 Scheme of (a) C_{60} , (b) C_{70} , (c) Coronene, and (d) Corannulene molecules.

..... **119**

Figure 6.2 Schematically illustration of binary guest molecule systems in COF-1. (a)

The system includes fullerene and coronene guest molecules. (b) The system includes

fullerene and corannulene. The planar and curved circulene guest molecules will

interact with COF-1 template and fullerene differently. **121**

Chapter 1. Introduction

1.1. Molecular self-assembly on 2D surfaces

Instigated by the famous “Plenty of Room at the Bottom” talk given by Feynman in 1959,¹ tremendous work has been devoted over the past few decades to make things small. “Nanostructured materials” are those typically defined by size spanning from subnanometer to several hundred nanometers.² In this size range, classical and quantum behaviors are mixed and materials can exhibit physical properties different from those of bulk materials; the study of these phenomena is collectively known as nanoscience.³ For example, at the nanometer scale, electronics band structures can be tuned through quantum confinement effects achieved by varying the size and dimension of nanoparticles (*Figure 1.1*).⁴ Another important aspect is that making functional units small can result in a significant decrease in device energy consumption and more efficient production processes. However, even if nanomaterials can exhibit remarkable properties, they can be applied into practical use only if suitable economical nanotechnology is viable. Thus, the development of methods to realize mass-controlled fabrication and integration of functional nanodevices into usable macroscopic systems is essential.

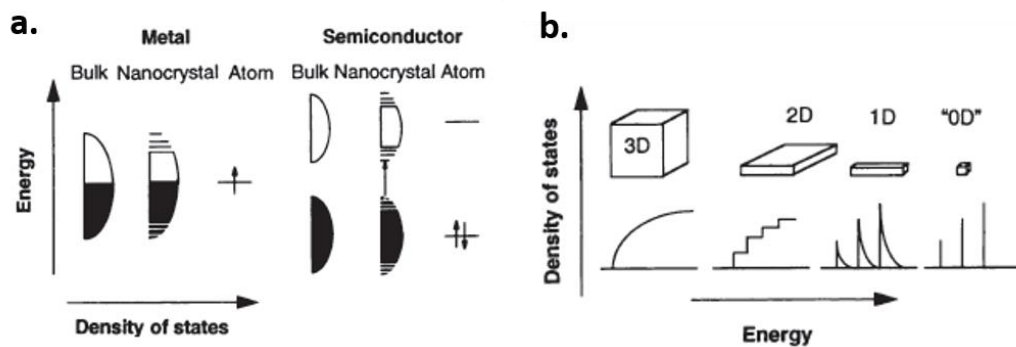


Figure 1.1 (a) Schematic representation of change in the density of state in one band according to the size of material (metal and semiconductor). (b) The density of state in one band of a semiconductor as a function of dimension. Reproduced with permission from the Science.⁴

There are two common methods to generate nanostructured materials and fabricate nanoscale structures in a controlled and repeatable manner, top-down and bottom-up (Figure 1.2).⁵ Top-down methods impose a structure or pattern on the substrate through an external process. In contrast, bottom-up methods aim to guide the assembly of components into organized structures through processes inherent in the system. The top-down approach includes serial and parallel techniques to create features typically in 2D over a large scale. To date, several excellent top-down-type approaches including photolithography and scanning beam lithography have been used to produce nanostructures.⁶ However, these conventional techniques have the limitations which have restricted their applicability, such as the high capital and operating costs in accessing the facilities and a general paucity of applicable materials. Moreover, as device features advance through the sub-10-nm regime, these top-down

approaches have begun to approach their resolution limit.⁷ The physical limits of defining nanoscale features is also problematic for future size reductions in nanostructures; for example a layer of silicon dioxide must be at least four to five atoms thick to function as an insulator.⁸ Because of these challenges to both traditional nanotechnology and nanoscience, interest has been growing in the alternative approach, *i.e.*, bottom-up methods.⁹

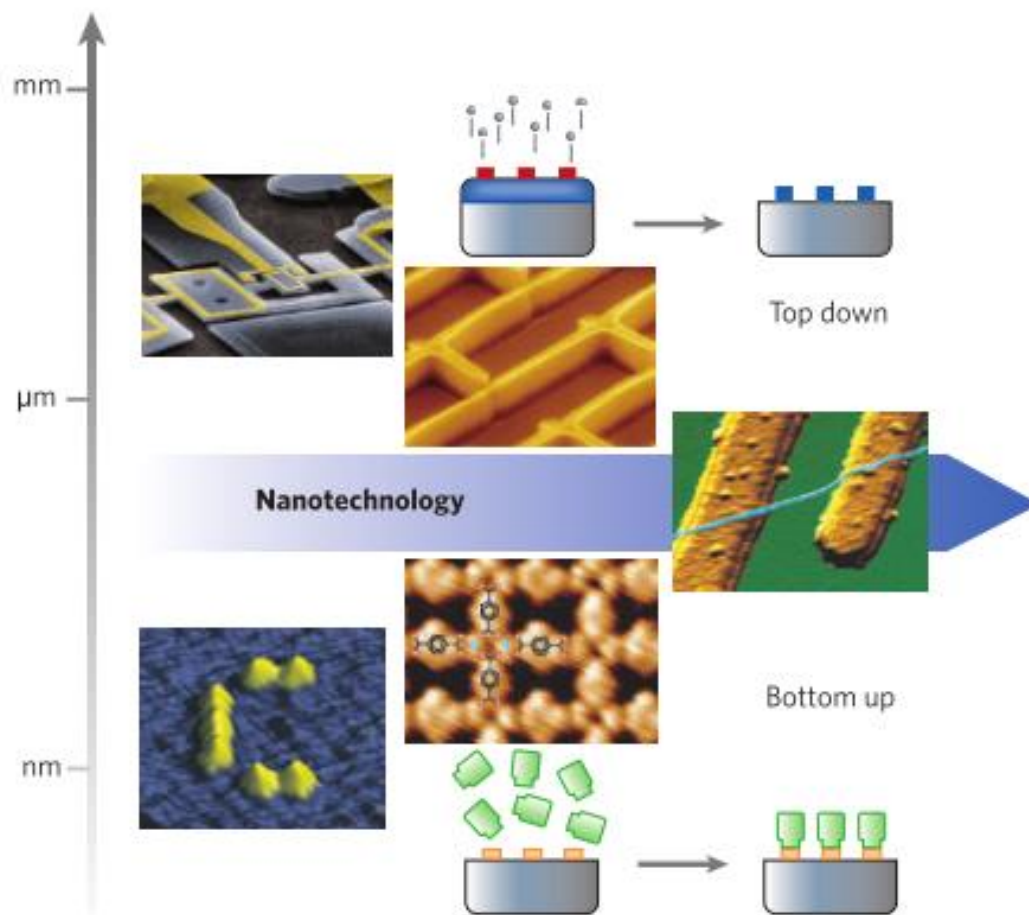


Figure 1.2 Two methods (top-down vs bottom-up) to produce matter at the nanoscale.

Top-down methods, such as lithography, writing or stamping, are used to define the desired features. The bottom-up techniques use self-processes to produce ordered

*patterns of supramolecular or solid-state architectures from the atomic to the mesoscopic scale. Reproduced with permission from the Nature Publishing Group.*⁵

Molecular self-assembly is a promising bottom-up methodology for large-scale fabrication of functional nanostructures, defined as a process in which molecules (or parts of molecules) spontaneously form ordered aggregates without human intervention.¹⁰ It is the pathway of lowest energy consumption and one of the few practical strategies for making ensembles of nanostructures. In addition, the study of molecular self-assembly is appealing because self-assembly is one of the basic process employed by biological systems, meaning that an understanding of self-assembly can help to unveil the mystery of the origin of life. The investigation of the spontaneous formation of ordered patterns can also bridge the study of distinct individual constituents and the investigation of systems as a whole.¹¹

Confinement of building block molecules onto a 2D surface is often necessary for the applications of many organic electronic and optoelectronic devices, where the substrate can play an important functional role such as the electrode for organic light-emitting diodes (OLEDs) or photovoltaic solar cells.¹² The substrate properties can also be tuned by deposition of molecules that self-assemble. For example, the assembly of organic acceptor tetracyano-*p*-quinodimethane has been demonstrated to p-dope graphene substrate through charge-transfer¹³ and induce a structural rearrangement at copper surfaces.¹⁴

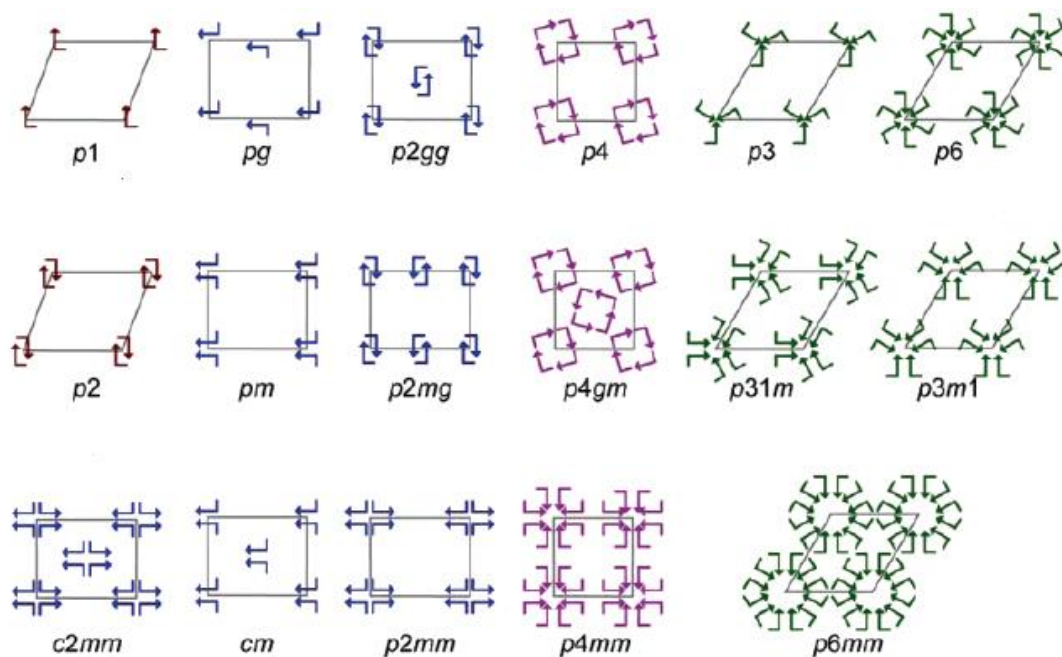


Figure 1.3 Schematic illustration of the possible 17 plane groups in 2D, describing the symmetry of monolayer molecular self-assembly. An arrow indicates each asymmetric unit, and unit cells are denoted with gray lines. Reproduced with the permission from American Chemical Society.¹⁵

Moreover, the reduced dimensionality of assembly on a surface can dramatically simplify the system with only 17 plane groups possible in 2D crystallization as compared to 230 space groups in 3D crystallization (Figure 1.3).¹⁵ The presence of the surface can also introduce extra effects impossible in 3D, such as the concentration-dependent polymorphism.¹⁶ Confining molecular self-assembly to a 2D surface offers the advantage of the application of some specialized characterization techniques. For example, using scanning tunneling microscopy (STM), the molecular arrangement on solid surfaces can be imaged in real space with submolecular

resolution, which provides a wealth of detailed information.¹⁷

2D molecular self-assembly under ultra-high vacuum (UHV) conditions depends critically on two types of interaction: molecule-substrate interactions stabilizing the molecules on the surface and molecule-molecule interactions that define the relationship between neighboring molecules.¹² However, when it occurs at solution/solid interface, the solvate-solvent and substrate-solvent interactions can also play an important role in the determination of 2D ordered patterns.¹⁸

The interaction between adsorbates and solid substrate can determine molecular adsorption geometries, sites and orientations. The role of surface will become more and more dominant when interactions move from weakly physisorbed to chemisorbed organic molecules.¹⁹⁻²⁰ For the surfaces with ordered arrays of dislocation networks,²¹ steps or patches with different chemical composition,²² the inhomogeneity of the molecule substrate-interaction can act as guidance for the growth of molecular nanostructures whose motif structure can be uniquely defined by adsorption-site selectivity. Thus, through the decoration or designation of the surface structure, it is possible to realize the precise control of the deposited molecular self-assembly.²³

Intermolecular interactions are another important factor that can influence molecular self-assembly. The interactions and motif structures of self-assembly depend on the nature and spatial arrangement of functional groups in the periphery of the backbone of molecular building block. According to the strength, intermolecular interactions can be divided as two types, non-covalent interactions and covalent interactions.

Table 1.1 Intermolecular interactions of self-assembly²⁴

Type of interaction	Strength (kJ/mol)	Character
Covalent bond	350	irreversible
Coordination binding	50-200	directional
Hydrogen bond	5-65	Selective, directional
van der Waals interaction	<5*	Non-selective, non-directional

*strength scales with the number of atom involved in the interaction

Since non-covalent interactions are weak and have the advantage of the reversibility of bonding, organic molecules can interact with each other to form long range ordered structures. In this context, the chemical nature of the individual molecules is preserved in the assembly and non-bonding interactions, such as hydrogen bonds,²⁵ van der Waals (vdW) interaction,²⁶ halogen bonds²⁷ and metal-organic coordination²⁸ (Table 1.1), drive the self-assembly process. However, these weak intermolecular interactions are also a limitation in these fragile structures. Such supramolecular assemblies are difficult to modify without losing their structure:

- (i) Modification of the functional groups typically will alter the interactions between the constituents and thus lead to different assemblies;
- (ii) performing chemistry on these assemblies is difficult without destroying their structural integrity;
- (iii) the thermal and chemical robustness of their structure puts a limit on their

applications.²⁹

By using covalent interactions to enhance the mechanical rigidity of structures, these disadvantages can be overcome (discussed in section 1.2). In addition, conjugated polymers can have semiconductive properties with a high efficiency of charge transport, which is desirable for electronic device applications.³⁰

Molecular self-assembly at the liquid/solid interface are more convenient and straightforward experimental approaches compared with those that require UHV conditions.¹⁸ Besides molecule-substrate and molecule-molecule interactions, the arrangement and stability of self-assembled structures at the liquid/solid interface also depends critically on the solvent used. The delicate balance among interactions between solvent, solvate and substrate would give rise to the competitive or coadsorption deposition of solvent molecules with adsorbate.

Solvents can be physisorbed or even self-assemble on the surface to form 2D structures.³¹⁻³² This requires solvent molecules have a higher affinity for the substrate than the solvate. The solvents can also be coadsorbed at the liquid/solid interface *via* vdW interactions with the substrate, or hydrogen bond or vdW interactions with the adsorbate molecules. For example, the carboxyl functional groups of 5-octadecyloxyisophthalic acid (C₁₈ISA) were observed to form hydrogen bonds with 1-octanol solvent molecules, leading to observed self-assembly with solvent co-adsorption. However, when 1-phenyloctane was used as the solvent, no coadsorption of solvent molecules could be observed. This variation implied that

hydrogen bond formation was the main reason for the solvent coadsorption (Figure 1.4).³³

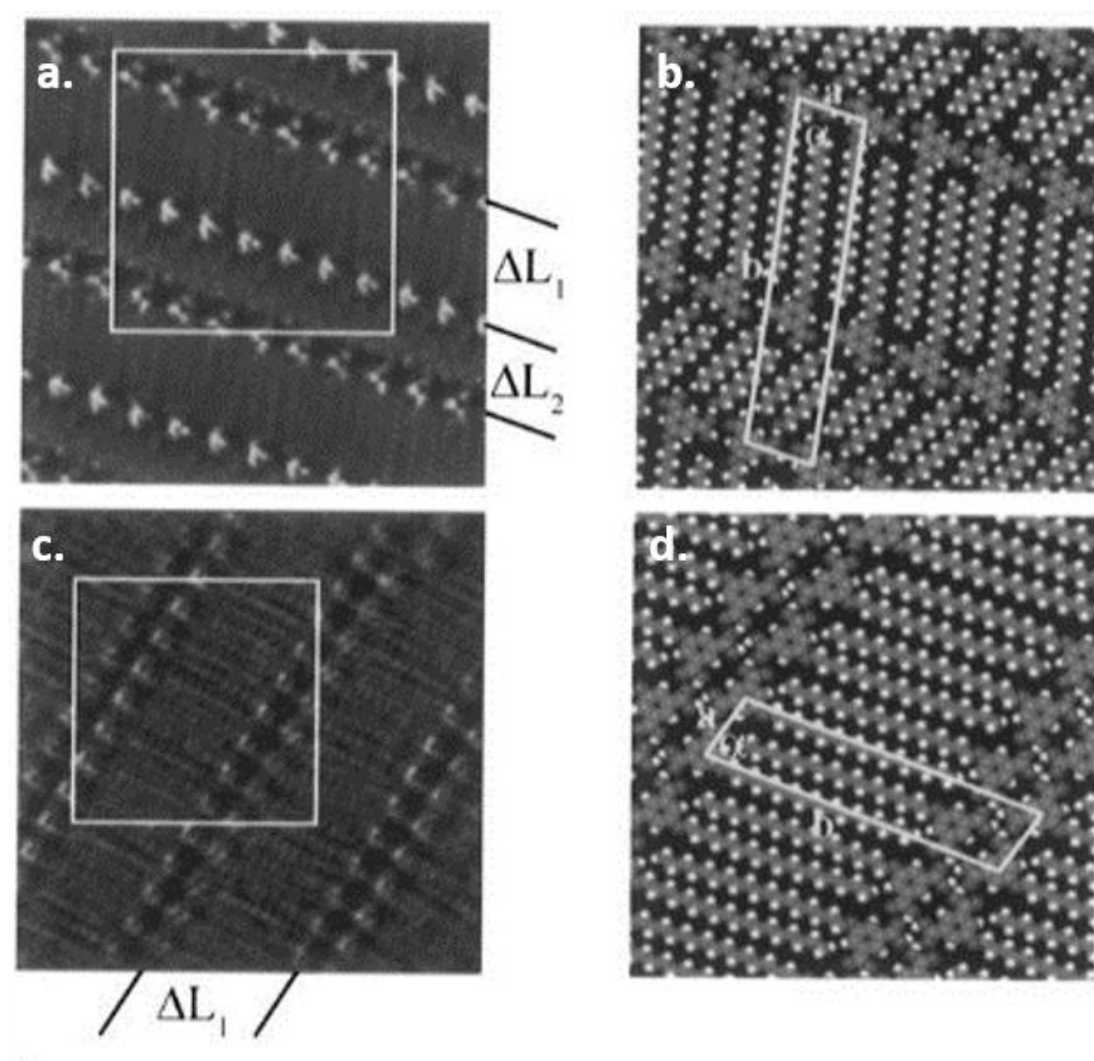


Figure 1.4 (a) STM image of self-assembly of $C_{18}ISA$ molecules at 1-octanol/graphite interface. The value of ΔL_1 corresponds to interdigitated $C_{18}ISA$, identical with the one in (c). The value of ΔL_2 corresponds to the width of the lamella formed by 1-octanol molecules. Image size is $10 \times 10 \text{ nm}^2$. (b) Molecular model represents the area indicated in (a). The unit cell for 1-octanol molecules coadsorption in two-dimensional packing of $C_{18}ISA$ molecules was proposed. (c) STM image of self-assembly of $C_{18}ISA$

*molecules at 1-phenyloctane /graphite interface. Image size is $10.7 \times 10.7 \text{ nm}^2$. (d) Molecular model represents the area indicated in (c), showing no solvent coadsorption. Reproduced with the permission from American Chemical Society.*³³

Solvents can also provide different microenvironments for the solute to self-assemble at the interfaces. The properties of solvent (viscosity, polarity, *etc.*) and solubility of solvate are all important factors to control the polymorphism of self-assembly through thermodynamic or kinetic effects.³⁴⁻³⁵ For example, trimesic acid (TMA) is a building block which can construct “chickenwire” structure (dimer motif) and “flower” structure (mixed dimer/trimer motif), both stabilized by hydrogen bonds on HOPG surfaces (*Figure 1.5a*).³⁶ The solvent induced polymorphism was studied by applying a series of alkyl acid solvents with different dielectric constants as solvent. “Chickenwire” structure is favored in less polar solvent (low solubility) and “flower” structure is favored in more polar solvent (high solubility). The possible explanation for this variation in monolayer identity is the stabilization of a TMA trimer solution phase nucleation species (precursor for “flower” structure) in the solvent with high solubility, but a TMA dimer (precursor for “chickenwire” structure) in the solvent with low solubility. In the same context, the self-assembly of 1,3,5-benzenetribenzoic acid (BTB), a bigger analogue of TMA, was also found to depend on the solvent in use. BTB can form two different structures, “chickenwire” structure and “oblique” structure (*Figure 1.5b*), which differ in their hydrogen bonding pattern but both have the dimer motif.³⁷ Experiments conducted to compare between the solvent molecules

with and without hydrophilic functional groups suggest a different mechanism, depending on whether the solvent can or cannot exert strong hydrogen bonds, for the formation of the interfacial monolayer structures at the liquid/solid interface. If the structure exposes a lower number of polar groups during the growth, then it will be preferred in a solvent of low dielectric constant and vice versa. Since the “oblique” structure exposes more free hydrogen bonds during the growth process, thus it was observed in more polar solvents. Although the above mechanisms were proposed in the TMA and BTB studies, the possibility of solvent co-adsorption cannot be ruled out, because the porous self-assembled structures can enable the interactions between solvent and substrate.

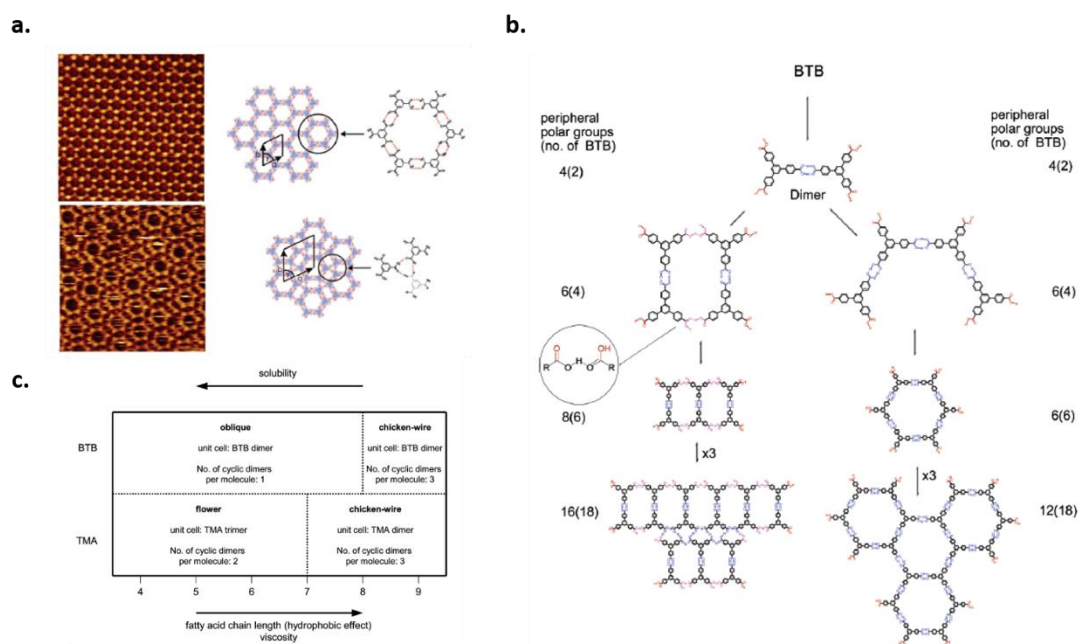


Figure 1.5 (a) (Top) The STM image and models for chickenwire structure of TMA. STM image was collected at the heptanoic acid/HOPG interface. Image size: $15 \times 15 \text{ nm}^2$. (Bottom) The STM image and models for flower structure of TMA. STM image was

collected at the pentanoic acid/HOPG interface. Image size: $15 \times 15 \text{ nm}^2$.³⁸ (b) Schematic representation of the seeding process for the oblique pattern (left) and the chickenwire motif (right) with the BTB dimer as the repeating unit forming. The count represents the number of polar functional groups exposed to the solvent, and those in the brackets represent the number of BTB molecules involved in the assembly. (c) Schematic representation of the properties for the series of alkanolic acids from butanoic to nonanoic acid and the respective interfacial monolayer polymorphs. Reproduced with the permission from American Chemical Society.³⁷

1.2. Covalent Organic Frameworks

Extended crystalline covalent organic frameworks (COFs) were first routinely synthesized from solution in a sealed reactor, where the reversible formation of covalent bonds provides the mechanism for error correction.³⁹ Since producing 2D COFs can potentially deliver single sheets of organic material, similar to highly popular graphene, but with a tunable structural motif, 2D COFs have been synthesized on surface using various approaches including Ullmann dehalogenation,⁴⁰ carbon-carbon covalent bond formation and dehydration reactions⁴¹ with the method of on-surface synthesis. Topologically, a 2D COF monolayer is composed of nodes and spacers. The cross-linked 2D network can be obtained with different symmetric building block molecules through “node” condensation or “spacer” condensation, as schematically presented in *Figure 1.6*.⁴² The successful realization of COF materials

through molecular building blocks can provide porous covalent frameworks that could be functionalized into lightweight materials optimized for gas storage, photonic, and catalytic applications based on host/guest chemistry.²⁹

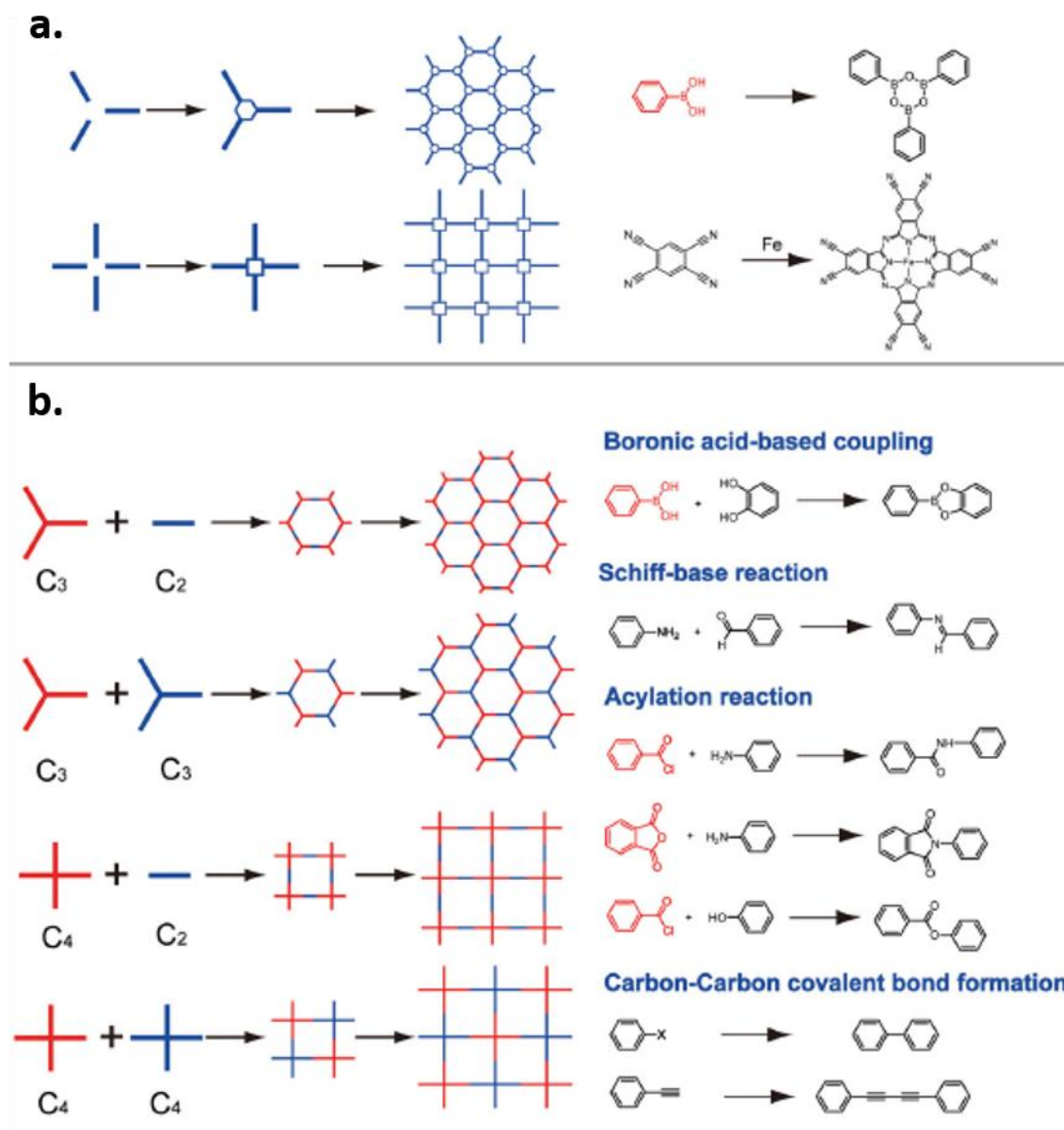


Figure 1.6 (a) The “node” approach for synthesis of 2D COFs. Examples are given on the right: cyclocondensation of three boronic acids molecules and tetramerization of four 1,2,4,5-tetracyanobenzene (TCNB) molecules with one Fe atom. **(b)** The spacer approach for synthesis of 2D COFs according to the symmetries of builders.

Corresponding examples are given on the right for the construction of 2D COFs: the condensation reaction between boronic acids and diols, the Schiff-based reaction, polyamide formation, polyimide formation, polyester condensation, Ullmann coupling, and Glaser coupling. Reproduced with the permission from Wiley.⁴²

Boronic acid-based building molecules were initially used to produce 2D COFs on Au(111) surface using the “node” construction mode in UHV conditions,⁴³ following on the first bulk COFs materials.³⁹ Three 1,4-benzenediboronic acid (BDDBA) monomers can form one boroxine (B_3O_3) ring through cyclocondensation (*Figure 2.1a*),⁴⁴ whereas intact BDDBA molecules can form a hydrogen-bond stabilized self-assembly on metal surface. Starting from this supramolecular self-assembly, the synthesis of COF-1 through tip- or electron beam -induced surface polymerization of BDDBA molecules was also developed.⁴⁵ However, since covalent bonds lack the degrees of reversibility under UHV conditions, several kinds of defects, such as pentagon and heptagon pores, were inherently formed, and the polymer structure always deviated from an ideal honeycomb two-dimensional network.⁴⁶ Therefore, the synthesis of larger-scale high-quality COFs is desirable.

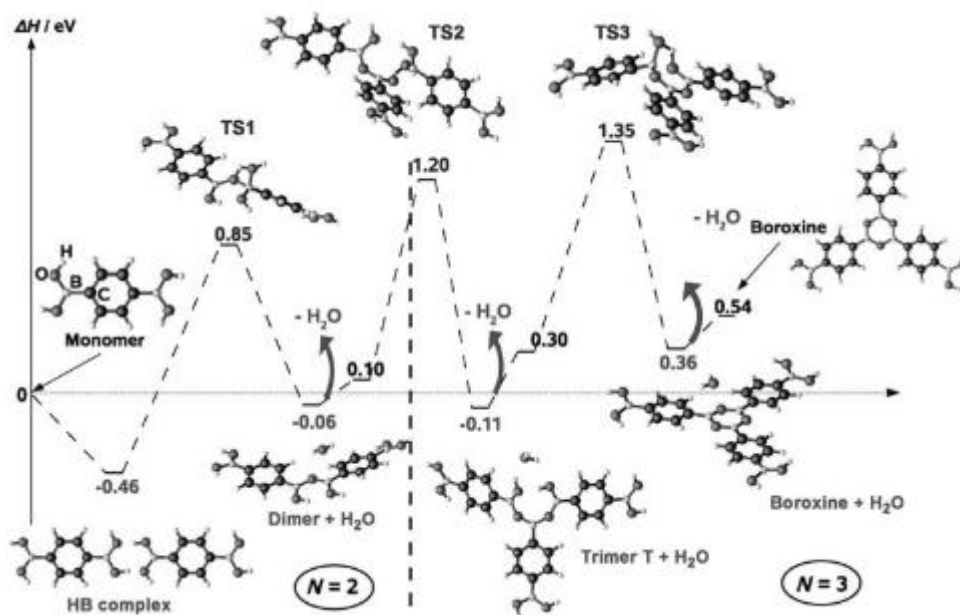


Figure 1.7 Enthalpic diagram showing the different transition states during polymerization reaction. The energies (in eV) are relative to the monomers. After each transition, a water molecule is released (arrows). Reproduced with the permission from Wiley.⁴⁷

Based on the dehydration reaction of boronic acids and thermodynamic-equilibrium control strategy, Li's and Lackinger's groups have succeeded in constructing large-scale high-quality COFs by using excess water as the chemical-equilibrium-manipulating agent in the closed and open environment conditions respectively (Figure 1.8).⁴⁸⁻⁵⁰ The large 2D COFs arrangements observed experimentally are stabilized through the entropic contribution of the water molecules released during 2D polymerization process of BDBA molecules (Figure 1.7).⁴⁷ Thus, the important effect of water in the formation process of an ordered 2D COF can be understood by Le Chatelier's principle. The presence of excess H₂O during the

poly-condensation changes the free energy of the reaction and favors a reverse reaction to a certain extent by pushing the equilibrium backward. The enhanced reversibility can improve the self-correcting abilities of the COFs and result in the formation of highly ordered honeycomb molecular nanostructures. Eventually, after excess water is removed, the ordered porous networks gain their robustness by ceasing bond reversibility.

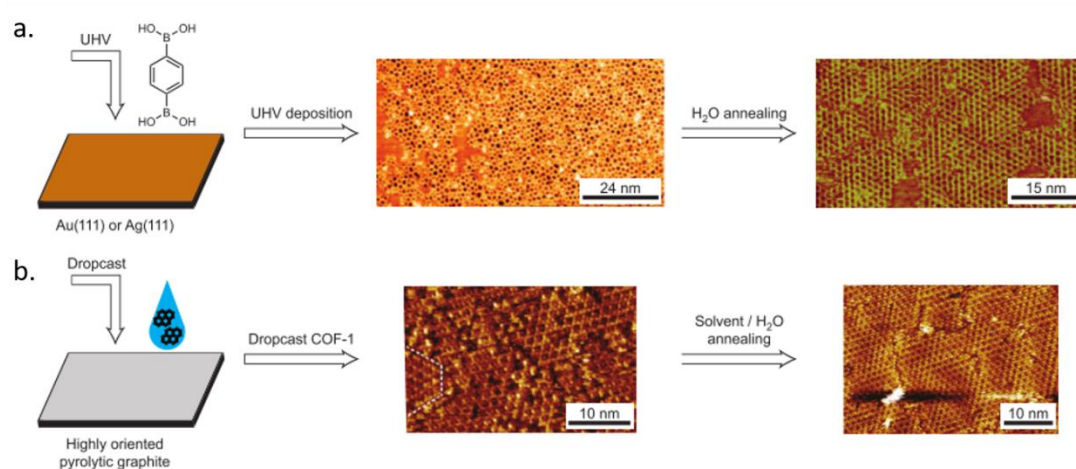


Figure 1.8 Synthesis of high-quality 2D COF-1 monolayer polymers. **(a)** BDBA monomer self-condenses onto crystalline metal surfaces in UHV to form COF-1 monolayer which containing various pentagonal and heptagonal ring defects (middle). The improvement in the order of the film can be initiated through annealing this film in a humid environment (right). **(b)** Pre-prepared COF-1 nanocrystals in solution were dropcasted onto HOPG surface (middle). Similar annealing can provide a monolayer with improved long-range order (right). Reproduced with the permission from the Nature Publishing Group.⁵¹

COFs processed under ambient conditions with monomer deposition from solution by

drop-casting offer much convenience for further applications,⁴⁹ but still bear many disadvantages, for examples: inhomogeneous coverages, including unwanted bilayers; insufficient reproducibility; contaminations; solubility issues, which can limit the size of the domains. Recently, in order to further improve the quality of COF-1, a new synthesis procedure of using vapor deposition instead of solution-deposition was developed. The progressively smaller length characterization on samples manifested that the sample prepared by vapor deposition protocol similarly yields high quality COF-1 monolayers, but significantly reduces sample contamination.⁵²

1.3. Host/Guest chemistry based on 2D templates

H/G chemistry is the important concept in supramolecular chemistry which describes the formation of unique structural complexes composed of two or more molecules or ions held together *via* non-covalent interactions. The mutually specific recognition between the host network and the guest molecules is the core idea of H/G chemistry. Although historically developed in organic and aqueous solutions, the principles of supramolecular H/G chemistry have been successfully implemented in self-assembled systems on solid surfaces.²² The reason why single layer molecular host/guest (H/G) architectures on surface have attracted a lot of attention is because they can provide a novel route towards porous materials that may find applications in molecular recognition, catalysis, gas storage and separation.^{51, 53}

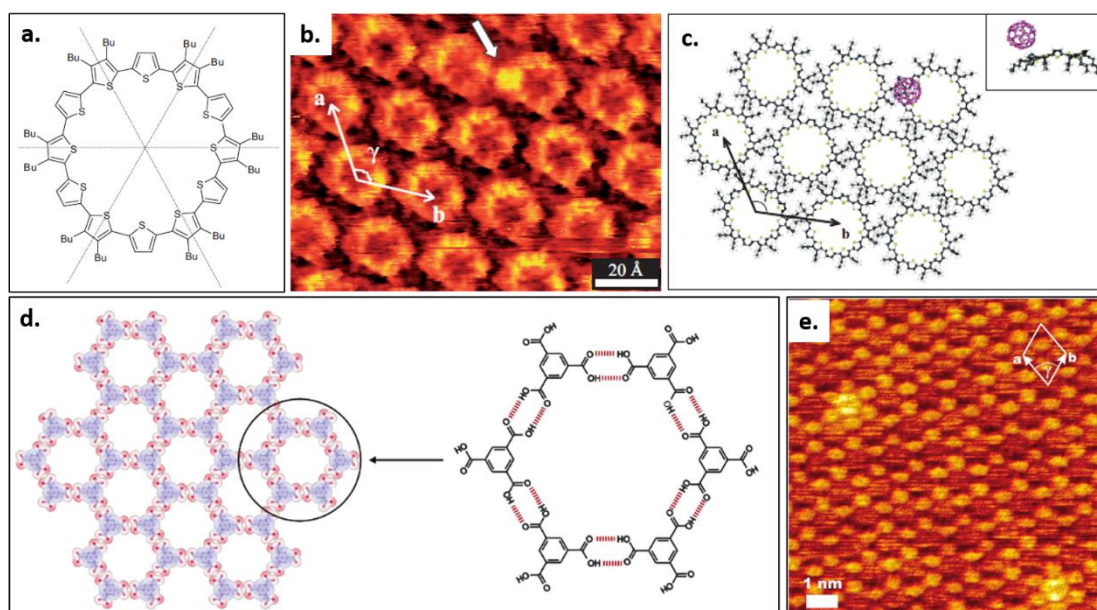


Figure 1.9 (a) Schematic of conjugated oligothiophene macrocycle, which is intrinsically porous. (b) STM image of a monolayer of macrocycles on HOPG. The adsorption of C_{60} is indicated with white arrow. Image area: $11.6 \text{ nm} \times 8.7 \text{ nm}$; Scanning conditions: $V = -700 \text{ mV}$, $I = 44 \text{ pA}$. (c) Calculated model of a closely packed monolayer of assembled template with intrinsic porous host molecules with a hexagonal arrangement. Inset picture exhibits side view of the calculated energy minimum conformation of a oligothiophene- C_{60} complex. Reproduced with the permission from Wiley.⁵⁴ (d) Illustration of the TMA chickenwire host, which is extrinsically porous. TMA molecules are drawn with the vdW surfaces of the atoms. The extrinsic single cavity stabilized by hydrogen bonds is indicated in the right enlarged sketch. (e) STM constant current image of the TMA- C_{60} host-guest structures. The diameter of the pores is 1.1 nm , and the unit cell of the hexagonal network is $a = b = 1.6 \pm 0.1 \text{ nm}$ and $\gamma = 60 \pm 1^\circ$ as depicted in the upper right corner. The adsorption of two C_{60} molecules inside the pores of the TMA host network appear as bright

*protrusions. Image dimensions: 10 × 10 nm². Reproduced with the permission from American Chemical Society.*⁵⁵

Surface-confined H/G structures rely on hierarchical interactions: the interactions binding the host monomer together are stronger than the interactions binding the guest to the host.⁵⁶ The presence of a solid surface can also provide additional stability for the resultant H/G structures through the molecule-substrate interactions. The 2D porous host networks can be constructed in intrinsic or extrinsic ways. The intrinsic porosity is inherent to the chemical structure of the constituent molecules, whereas extrinsic porosity results from non-covalent (or covalent) assembly of the constituent molecules, which usually do not bear porosity in isolation (*Figure 1.9*). The intrinsic porous self-assembled host template is typically stabilized by vdW interactions,^{54, 57} while an extrinsic porous self-assembled host template can be stabilized through several different interactions (Table 1.1). Although based on hierarchical interactions of H/G, rigid host templates with fixed pore sizes, such as those sustained by hydrogen bonding or metal-ligand interactions, are favorable for guest selectivity, flexible host networks stabilized by vdW interactions also provide reasonably high selectivity. Because of the ability to design interactions in a host network *via* judiciously chosen molecular components, the majority of H/G studies carried on solid surfaces have focused on extrinsically porous systems. For example, isorecticular scalability of COF cavities can be achieved through simply increasing the size of the molecular building blocks.²²

H/G structures can offer spatially controlled fixation, observation, and precise manipulation of matter down to the single molecule level, which is an essential requirement for nanotechnology applications.⁵⁸ The manipulation of a single molecule^{55, 59} can be carried out by STM at the liquid/solid interface without the need for experimentally challenging UHV techniques. For example, the proof of principle work has been reported by Griessl, where the adsorption site of C₆₀ molecule in a TMA template can be manipulated by varying the tunneling current through an STM tip.⁵⁵

H/G chemistry is also associated with the study of selective recognition of a molecule (guest) by another molecule (host) *via* the formation of non-covalent interactions. Several strategies for selectivity in guest bonding have been developed based on the geometry of host, such as pore size,⁶⁰⁻⁶¹ shape⁶²⁻⁶³ and chirality⁶⁴ or chemical environment of host⁶⁵. For example, two different shape species can be trapped by a nanotemplate at the same time (*Figure 1.10*). A novel hydrogen bonding molecular network with two different cavities can be formed from tetra-acidic azobenzene (NN4A). The coronene (CORO) molecule is only entrapped in the hexagonal cavity due to the pore size and shape and C₆₀ will be entrapped in exclusively in the triangular cavities. The network can serve as a supramolecular nanoporous template to simultaneously accommodate C₆₀ and coronene molecules, forming a coronene/C₆₀/NN4A ternary architecture. Based on similar selective recognition principles, a number of multicomponent H/G systems were also reported, wherein

either the host template or the guest species can comprise more than one type of molecular building blocks.⁶⁶⁻⁶⁸ For example, the complexity of H/G self-assembly was extended to a three component H/G architecture assembling at the solution-solid interface. Instead of using a single of type of guest, a heteromolecular guest cluster composed of coronene and isophthalic acid (ISA) could be immobilized in host network formed by dehydrobenzo annulene (DBA) derivative.⁶⁹

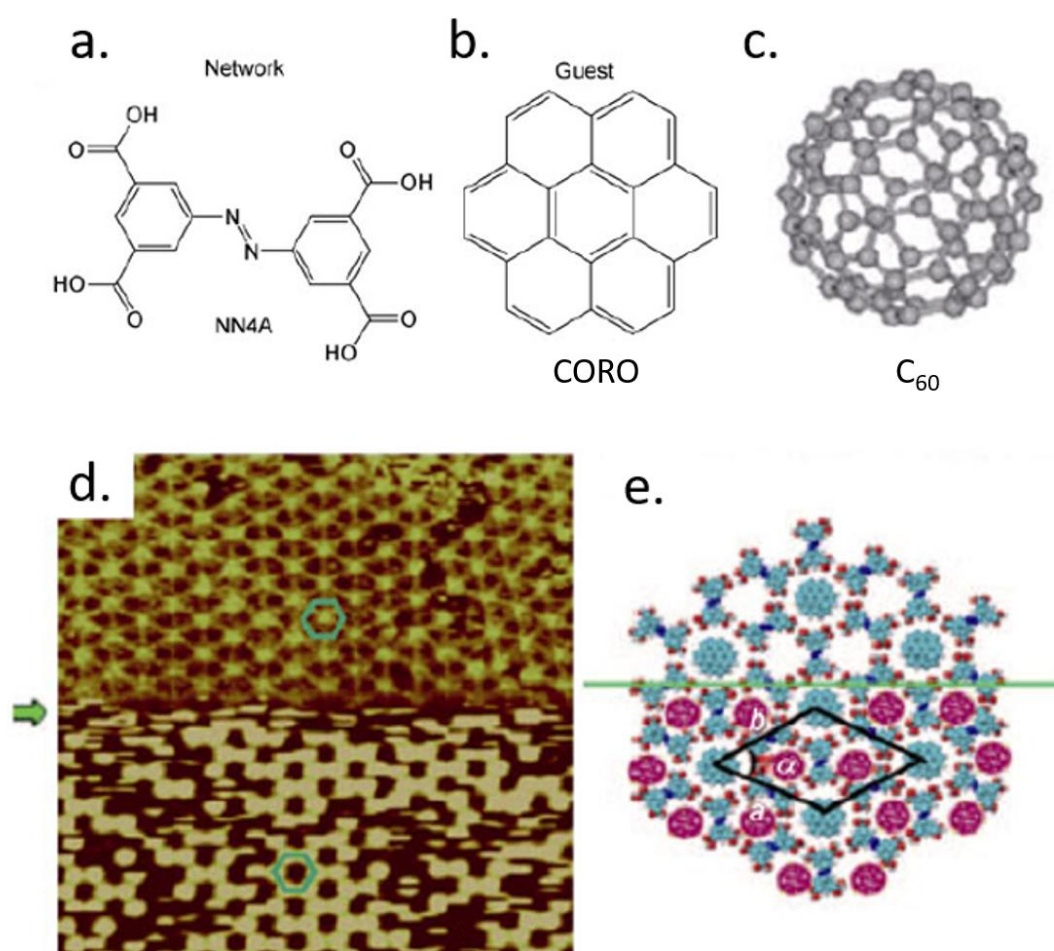


Figure 1.10 The chemical structures of the NN4A and guest molecules: (a) NN4A, (b) coronene, (c) C₆₀. (d) The STM image of coronene/C₆₀/NN4A ternary architecture at alternate bias and current. Image dimensions: 41 × 41 nm² The line at which the bias

changed is marked by a green arrow. The scanning conditions of upper area and lower one are $I=1055\text{ pA}$, $V=516\text{ mV}$ and $I=128\text{ pA}$, $V=968\text{ mV}$, respectively. (e) A molecular model of coronene and C_{60} molecules co-adsorbed on NN4A networks. Reproduced with the permission from Wiley.⁶³

Molecular recognition in H/G chemistry can constitute proof-of-concept for the design of sensors.⁷⁰ For example, the modulation of the conductivity of the active conducting materials upon the H/G binding event can be transduced into electric signals, as shown in *Figure 1.11*.⁷¹ Confining a guest in a 2D host structure represents the ultimate limit of design for an organic field effect transistor-based sensor, where devices with thin active layers are used for their high response speed and sensitivity to target molecules.⁷²

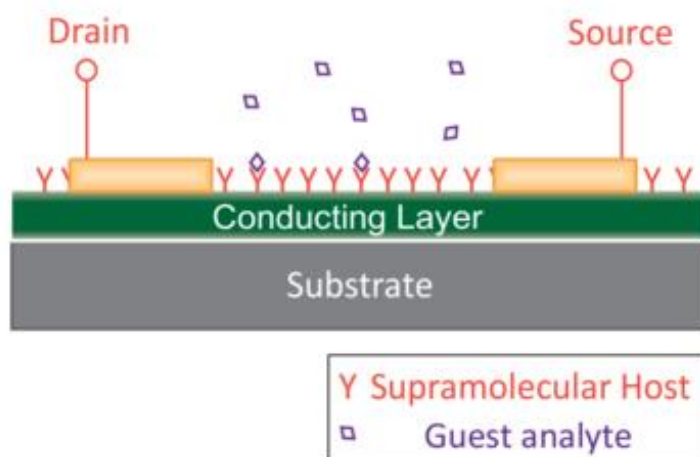


Figure 1.11 Graphic representation of a FET chemical sensor.⁷¹

In addition, the growth of template networks, able to form H/G structures,²² has also

been an important methodology for controlling crystallization into the third dimension using molecular building blocks. For example, a bilayer H-bonded Kagomé structure⁷³ and self-aggregation of π -stacked heterocirculenes⁷⁴ have been observed based on 2D H/G structure. Moreover, fullerenes and their derivatives with non-planar geometry, when stabilized by weak interaction on 2D templates, can promote configurations defined by the template that deviate from standard close-packing.^{23, 75-78} The cooperative interaction of H and G species was manifested through the observation of the induced growth of a second layer of a supramolecular framework by the trapped fullerenes (*Figure 1.12*).⁷⁹ Although H/G structures have so many potential applications, the COFs based H/G structure have not been investigated intensively.

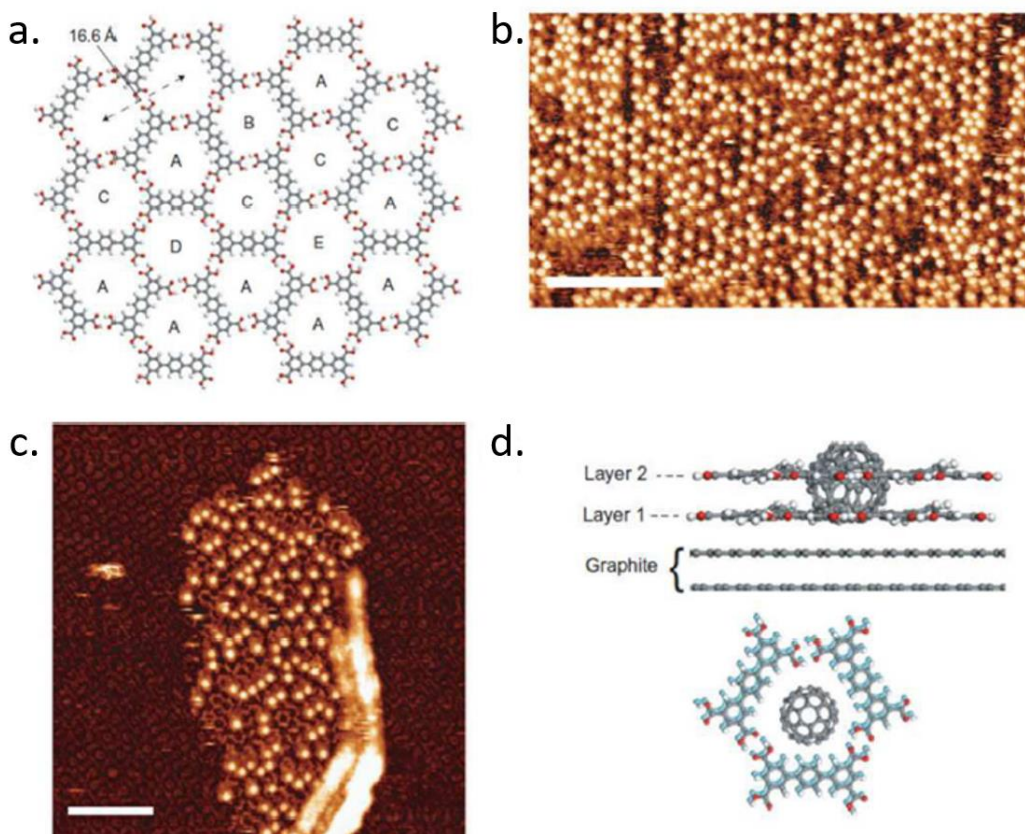


Figure 1.12 (a) Schematic illustration of the random rhombus tiling formed by the terphenyl-3,3'',5,5''-tetracarboxylic (TPTC) acid framework. Different hexagonally ordered network of pores is highlighted by A-E. (b) STM image of TPTC network after a deposition of C₆₀. The locations of C₆₀ are visible as bright spots in the image and the underlying TPTC network is not visible. Scale bar: 16 nm; (c) STM image of TPTC bilayer immediately collected after C₆₀ deposition. The co-adsorption structure of C₆₀ and bilayer TPTC framework can be identified. The first layer of TPTC framework is visible with an altered contrast and the second TPTC molecules appear with the long axis of the molecules as bright, rod-like features. Scale bar: 11 nm. (d) Schematic representation of the co-adsorption of C₆₀-bilayer structure consisting of two overlying pores of type A. Reproduced with the permission from the Nature Publishing Group.⁷⁹

1.4. Thesis objectives and organizations

My thesis focuses on the development of H/G structures based on COFs.³⁹ Since COFs acting as template have not been intensively investigated, this project offers a first look at the stability and architectures accessible through a COF/guest system. The successful direct synthesis of single layer 2D COF-1³⁹ on highly ordered pyrolytic graphite (HOPG)⁴⁹⁻⁵⁰ is foundational to this work.

The goal of this investigation is to explore a range of different architectures of H/G based on COFs template. The spherical C₆₀ is used as a model guest molecule, as shown in *Figure 2.3*. The method of characterization is mainly STM. This thesis will offer both fundamental understanding and a novel methodology for H/G structures based on COF-1 template, opening the gate for a range of further investigations of applications-targeted H/G structures.

In Chapter 2, the synthesis method of COF-1 and the basic principle of STM characterization are introduced.

In Chapter 3, COF-1 acts as a robust host for C₆₀ fullerene guest molecules at the solution/solid interface and under ambient conditions, demonstrating the possibility for COF-based host/guest architectures at monolayer thickness. At both the solution/solid interface and in dried films, COF-1 presents a lattice with two distinct fullerene adsorption sites: a pore site, where the C₆₀ molecule is adsorbed on the underlying HOPG, and a top site, where the fullerene is adsorbed on the boroxine ring.

In Chapter 4, the effect of pore shape and size on the solvent adsorption has been investigated. The results show that different solvent molecules can present distinctive influence on the adsorbed position of C_{60} molecules, suggesting that COF-1 lattice can separate guest molecules, opening opportunities for applications in molecular patterning and recognition.

In Chapter 5, COF-1 shows the capability to serve as the template for a 3D nanofabrication with atomic precision. The template-defined packing, which deviates from standard close packing, depends on the solvent for the fullerene molecules: a template-defined close-packing motif is achieved using 1,2,4-trichlorobenzene (TCB) as solvent, whereas lower-density quasi-close-packed polymorphs are observed when using heptanoic acid as solvent. The solvent-dependent polymorphism and morphologies can be described in terms of a template-driven solvent co-adsorption effect.

Finally, in Chapter 6, the conclusion and perspectives are given.

Chapter 2. Experimental techniques

2.1. COF synthesis on HOPG and guest molecule

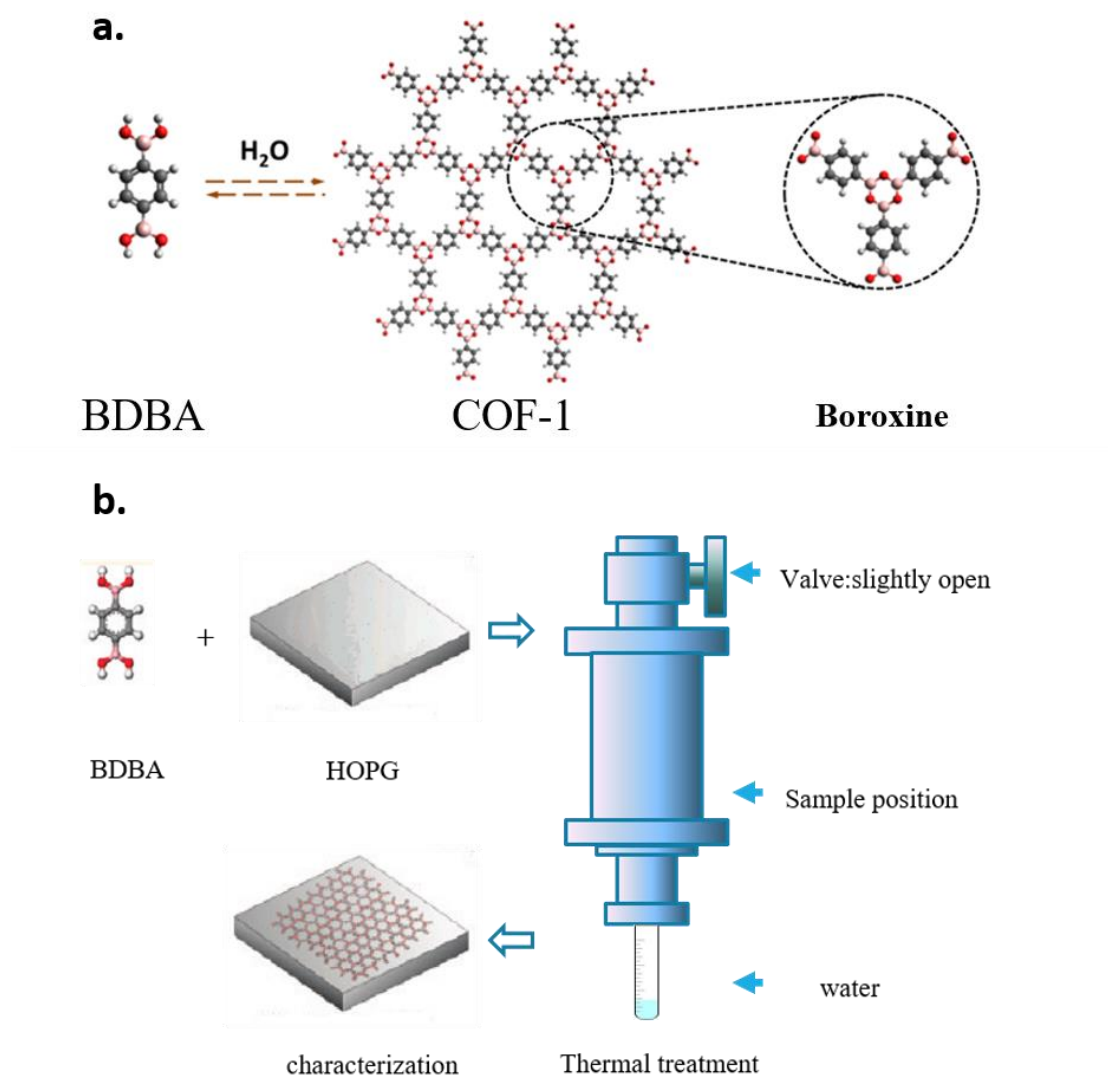


Figure 2.1 (a) The scheme of COF-1 and the chemical reaction for synthesizing template: self-condensation of BDBA monomers gives rise to 2D COF-1 template wherein defects are recovered through the reversible reaction that occurs in the

presence of water. The scheme of the boroxine ring is enlarged in the inset circle.⁸⁰ (b)

The schematic illustration of the setup of synthesizing COF-1 on HOPG substrate.

BDBA COFs were formed following procedures described previously.⁴⁹⁻⁵⁰ 1 mg of 1,4-benzenediboronic acid (Tokyo Chemical Industry Co. Ltd) was added to 1.5 ml heptanoic acid (or 1,2,4-trichlorobenzene), and then sonicated for approximately 30 min. This step produced a whitish suspension. 7.5 μ l of this BDBA suspension was dropped onto freshly cleaved HOPG (Structure Probe International, grade SPI-1 or SPI-2, *Figure 2.2*) and put into a reactor with a volume of ~16 ml. 130 μ l deionized water was added to the bottom of the reactor, and a valve to ambient was left slightly open to maintain an open system. The entire reactor was placed in an oven preheated to 125 °C and left for 60 min.

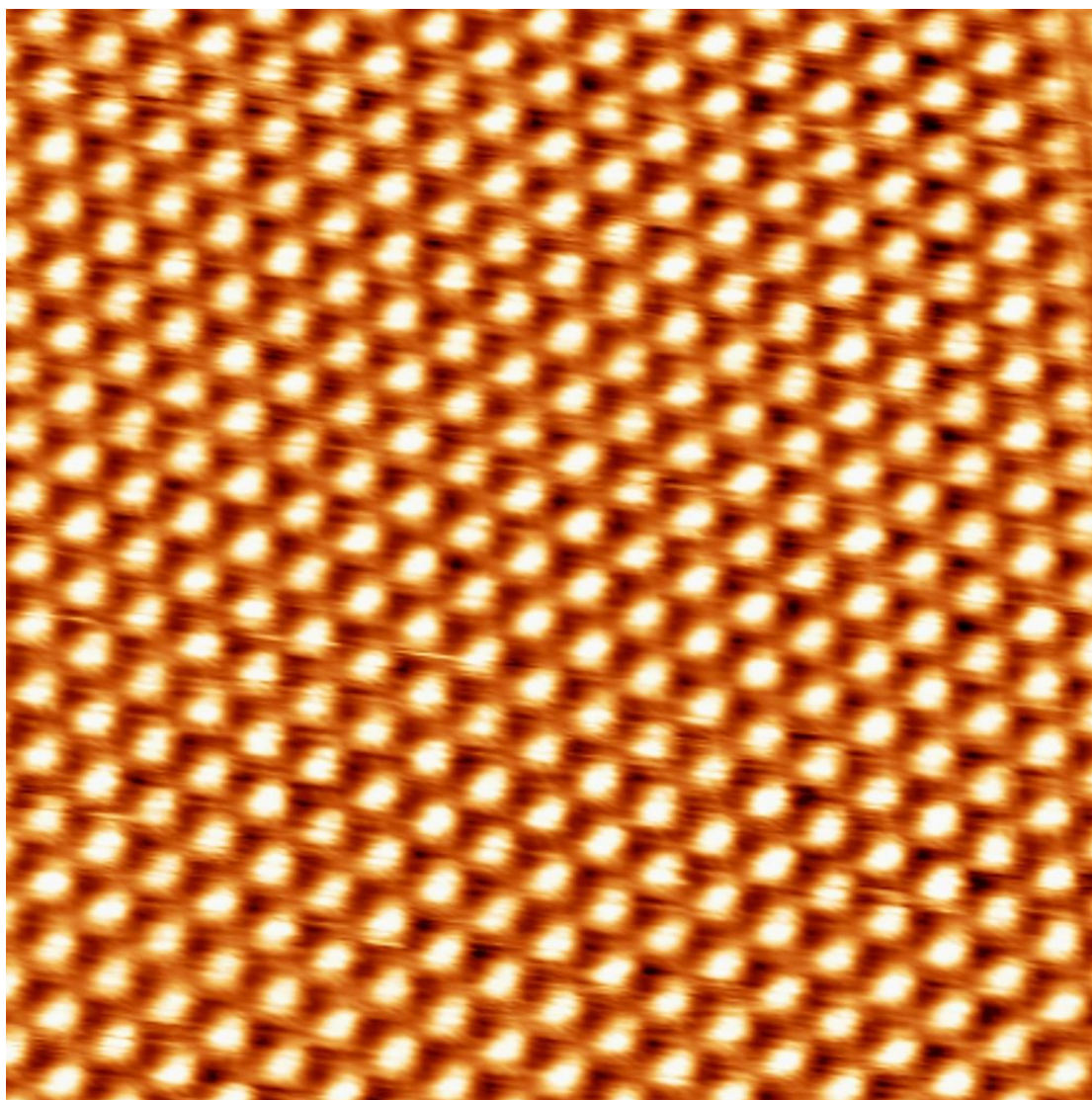


Figure 2.2 STM image of HOPG. Image dimensions: $4.2 \times 4.2 \text{ nm}^2$. Tunneling conditions: $V=-19 \text{ mV}$, $I= 1000 \text{ pA}$. The hexagonal lattice constant of HOPG is 0.246 nm .

After the thermal treatment, the reactor was taken out of oven and allowed to cool for at least 20 min before the samples were removed. The synthesis procedure is schematically shown in *Figure 2.1b*. Subsequently, the samples were characterized by STM at the air/solid interface. The scheme of reaction is shown in *Figure 2.1a*.

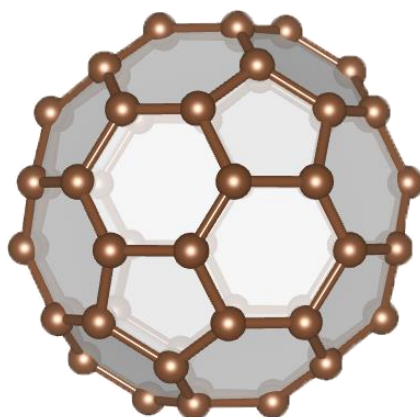


Figure 2.3 Scheme of C_{60} guest molecule.

After the presence of COF-1 is confirmed with STM, an amount of C_{60} guest molecules in different solvent with a known concentration was applied onto the HOPG substrate.

C_{60} is the one of the most widely used guest molecules in 2D H/G investigation.^{54, 60, 81-83} Since its discovery in 1985,⁸⁴ C_{60} has received tremendous attention due to its unique structure and properties. It consists of 20 hexagonal and 12 pentagonal rings arranged with icosahedral symmetry (*Figure 2.3*). Carbon atoms are bonded to each other through sp^2 hybridized bonds, but double bonds tend not to be present at the pentagonal rings. This results in poor electron delocalization and electron deficient property, permitting the formation of charge-transfer complexes with suitable donors. Thus C_{60} has been regarded as a potential molecular building block in molecular engineering, novel materials synthesis, and supramolecular chemistry for the

applications of photovoltaics and field effect transistors.⁸⁵⁻⁸⁷

2.2. Scanning Tunneling Microscopy (STM)

The STM is capable of imaging surfaces with an atomic resolution. It was invented by Gerd Binnig and Heinrich Rohrer in 1981 at IBM Zürich.⁸⁸⁻⁸⁹ They received the Nobel Prize in Physics five years later for the many implications of STM on surface characterization. *Figure 2.4* shows the essential elements of STM. A metallic probe tip, usually made of W or Pt-Ir alloy, is attached to piezoelectric transducers. By placing the tip very close (a few of Angstroms) to the conductive surface and applying a bias voltage between them, there is a probability that an electron will transfer from the tip towards surface or from the surface to the tip, due to the overlap of electron wavefunctions in the tip and sample. Such a current is a quantum-mechanical phenomenon, *tunneling*, as discussed in detail below.

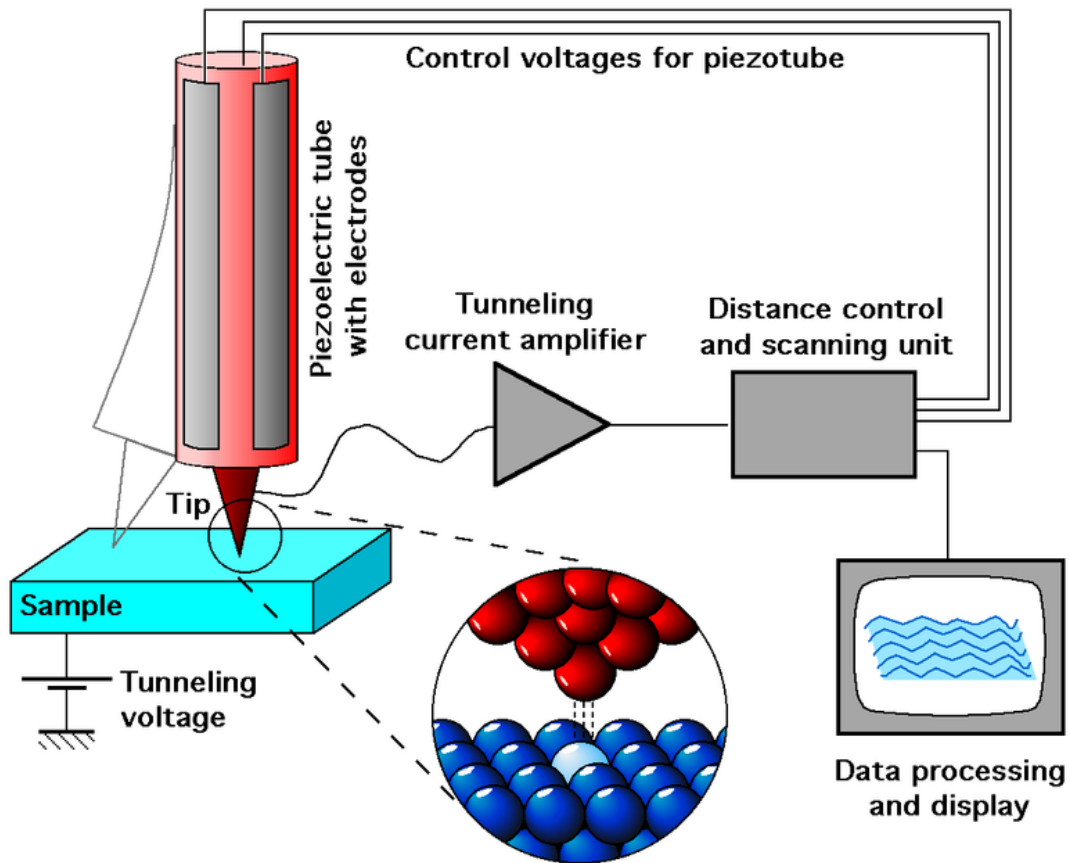


Figure 2.4 Schematic diagram of the scanning tunneling microscopy, produced by Michael Schmid and Grzegorz Pietrzak, and used under CC BY-SA 2.0 AT.¹

From an elementary model, the basic features of the tip-vacuum-sample junction tunneling can be described, as shown in *Figure 2.5*. In quantum mechanics, the static state of an electron in the potential described by $U(z)$ can be represented by a wavefunction $\psi(z)$ which satisfies time-independent Schrödinger's equation,

$$-\frac{\hbar^2}{2m} \frac{d^2}{dz^2} \psi_n(z) + U(z)\psi_n(z) = E\psi_n(z), \quad (2.1)$$

When $E > U(z)$, Eq. (2.1) has a solution

¹ <https://creativecommons.org/licenses/by-sa/2.0/at/deed.en>

$$\psi_n(z) = \psi_n(0)e^{\pm ikz}, \quad (2.2)$$

where

$$k = \frac{\sqrt{2m(E-U(z))}}{\hbar}, \quad (2.3)$$

is the wave vector and n is the quantum number.

When $E < U(z)$, Eq. (2.1) has a solution

$$\psi_n(z) = \psi_n(0)e^{\pm \kappa z}, \quad (2.4)$$

where

$$\kappa = \frac{\sqrt{2m(U(z)-E)}}{\hbar}, \quad (2.5)$$

is the decay constant.

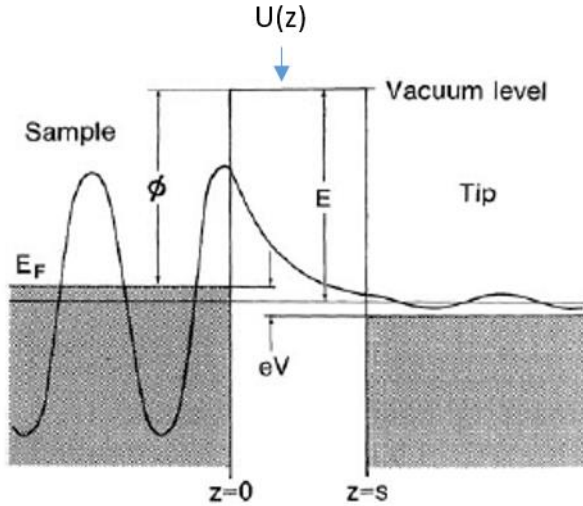


Figure 2.5 An illustration of STM mechanism: the one-dimensional metal-vacuum-metal tunneling junction. The sample (left) and the tip (right) are modeled as semi-infinite pieces of free-electron metal. The work function is represented as ϕ , defined as the minimum thermodynamic work required to remove an electron from the bulk to the vacuum level. Neglecting the thermal excitation, the

Fermi level, E_F , is the upper limit of the occupied states in a bulk metal. Here, the work functions of tip and sample are assumed to be equal. The bias voltage leading to the realignment of Fermi levels of sample and tip is represent as eV . The spatial width of vacuum (energy barrier) is indicated as S .⁹⁰

By applying a bias voltage V , the electrons at the state ψ_n with energy level E_n lying between $E_F - eV$ and E_F have a chance to tunnel into the tip. The probability, η , for an electron in the n th state to penetrate a certain barrier of S is

$$\eta \propto |\psi_n(0)|^2 e^{-2\kappa S}. \quad (2.6)$$

We can assume that bias V is much smaller than the value of the work function, *i.e.*, $eV \ll \phi$, then

$$\kappa = \frac{\sqrt{2m\phi}}{\hbar}, \quad (2.7)$$

is the decay constant of the sample states close to Fermi level in the energy barrier region.

The tunneling current is directly related to the number of states on the sample surface within the energy interval eV . It is convenient to define *the local density of states* (LDOS), $\rho_s(z, E)$, as the number of electrons per unit volume per unit energy at a given point in space and a given energy.

$$\rho_s(z, E) = \frac{1}{\varepsilon} \sum_{E_n=E-\varepsilon}^E |\psi_n(z)|^2. \quad (2.8)$$

Including all the energy states within the energy interval, the tunneling current can be written in terms of the LDOS of the sample or tip (depend on the direction of bias voltage):

$$I \propto V \rho_s(0, E_F) e^{-2\kappa S}. \quad (2.9)$$

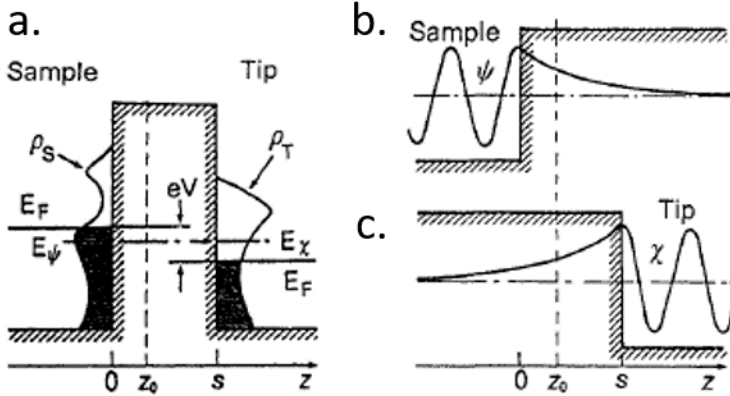


Figure 2.6 The Bardeen approach of tunneling theory.⁹⁰

However, this elementary model does not consider the thermal activation and solving Schrödinger's equation of whole system is typically difficult. Instead of trying to solve the equation for the coupled system (*Figure 2.6a*), Bardeen developed an approach based on perturbation theory⁹¹ starting with two free subsystems (*Figure 2.6b and c*) to calculate the tunneling current through the overlap of the wavefunctions of free systems using Fermi's golden rule.

With a bias voltage V , the total tunneling current is

$$I = \frac{4\pi e}{\hbar} \int_0^{eV} [f(E_F - eV + \epsilon) - f(E_F + \epsilon)] \times \rho_s(E_F - eV + \epsilon) \rho_T(E_F + \epsilon) |M|^2 d\epsilon, \quad (2.10)$$

where $f(E) = \{1 + \exp[(E - E_F)/k_B T]\}^{-1}$ is the Fermi distribution function, and $\rho_s(E)$ and $\rho_T(E)$ are the density of states (DOS) of the sample and the tip. M is the tunneling matrix element determined by the overlap of the surface wavefunctions of the two subsystems at a separation surface, expressed as

$$M = \frac{\hbar}{2m} \int_{z=z_0} (\chi^* \frac{\partial \psi}{\partial z} - \psi^* \frac{\partial \chi}{\partial z}) dS, \quad (2.11)$$

where χ and ϕ are the wavefunctions of tip and sample.

According to Eq. 2.10, the intensity of tunneling current is determined by the LDOS of sample and tip (ρ_S and ρ_T), bias voltage ($E_F - eV$) and tip-surface distance (M). When STM is conducted in the constant current mode, for a given bias voltage, the measured signal actually is the convolution of LDOS within the energetic interval ($E_F - eV$) and the topology (z position). Therefore, an STM image is not a purely topographic image, but also contains the LDOS information. By changing the bias voltage, the involved energetic interval LDOS ($E_F - eV$) can be modified. Thus, different bias voltage typically will give different image contrast.

In practice, STM requires an extremely flat substrate, down to atomic level, because STM tips have difficulties in scanning very steep features. For ambient conditions, HOPG is the most commonly used substrate since it is a naturally layered inert material and the fresh large flat surface can be easily prepared through peeling away the top layer by an adhesive tape.

If STM is performed at the solution/solid interface, the organic solvents in use typically comply with the following requirements: (1) for the sake of convenience, they should have a low vapor pressure so that the STM measurements are performed under a relatively constant environment without the need of a closed cell, (2) under the experimental conditions (applied bias between tip and sample), they should be electrochemically inert, (3) the compound of interest can be dissolved in them, and (4) they have a low affinity for adsorption on the substrate used unless solvent adsorption

is explicitly desired.¹⁶¹

Chapter 3. Solution and air stable host/guest architectures from a single layer covalent organic framework

Daling Cui, Jennifer M. Macleod, Maryam Ebrahimi, Dmitrii F. Perepichka and Federico Rosei. *Chem. Commun.* **2015**, *51*, 16510-16513.

Daling Cui's contribution: the collection and analysis of data, drafting manuscript.

3.1. Introduction

COFs have gained considerable attention, since first being synthesized in 2005,³⁹ as robust porous crystalline solids that can be synthesized to incorporate application-specific functionalization.⁹²⁻⁹³ By employing precursor molecules with different functional groups, boronic acid(BA)-based COFs can be tailored for specific applications, for example the storage of hydrogen⁹⁴⁻⁹⁵ and other gases,⁹⁶⁻⁹⁷ or photoconductivity.⁹⁸⁻⁹⁹ A number of investigations, both experimental¹⁰⁰⁻¹⁰¹ and theoretical,¹⁰²⁻¹⁰³ have focused on bulk heterojunctions formed by COFs with ordered charge donors and acceptors, targeting applications in photovoltaics.

The layered structure of COFs is analogous to the packing of graphene into graphite, with non-covalent (dispersive and electrostatic) interactions stabilizing the basal planes defined by the 2D COFs¹⁰⁴ into 3D crystals. There is hence considerable interest in isolating 2D sheets of COF, motivated by analogy with the exceptional

materials properties of graphene.¹⁰⁵⁻¹⁰⁶ COF platelets several layers thick can be produced by delaminating 3D COFs through sonication¹⁰⁷⁻¹⁰⁸ or mechanical exfoliation.¹⁰⁹ The direct synthesis of single layer 2D COFs on a substrate addresses the advantage of defining the orientation of the COFs, which is necessary for most device applications,¹¹⁰⁻¹¹¹ and allows for the use of tailored vapor-solid reactions to produce 2D COFs.¹¹²

The surface-confined synthesis of COFs has previously been carried out by self-condensation of BDBA under UHV. Under these conditions, the rapid removal of the by-product water molecules precludes reversibility and leads to a relatively disordered network of poly(BDBA),^{45, 113} a single layer of COF-1.³⁹ When synthesized on-surface under ambient pressure and elevated humidity, defect correction within the COF lattice leads to improved structural order.⁴⁸⁻⁴⁹ As has been demonstrated in 3D COFs,¹¹⁴ the range of available BA derivatives allows to tune the structural properties of surface-synthesized COFs.⁵⁰

On the other hand, extensive work has been carried out on surface-confined, single layer H/G architectures where the host is a noncovalent porous molecular network stabilized by, *e.g.*, hydrogen bonds,^{55, 76, 81} vdW interactions,^{54, 57, 115} or metal-organic coordination.¹¹⁶ The formation and characterization of these H/G networks has been performed under both UHV conditions^{59, 76, 115-116} and at the solution/solid interface.^{54-55, 81} Compared with these non-covalent networks, the robustness of COFs presents an advantage for preparation of systems with covalent guest molecules,

opening the door to a range of new functional host-guest materials.

In this chapter, we report on the synthesis of a single-layer H/G structure that uses HOPG-supported COF-1 as the host template. This template stabilizes fullerene guests at the solution/solid interface; in turn, the solution/solid structure can be dried to produce an air-stable H/G architecture. The insertion of guest molecules can also be implemented using a “dipstick” method, wherein substrate-supported COF-1 is dipped into a solution of fullerene molecules and allowed to dry. These results indicate that single-layer COFs may be suitable for applications in molecular sensing or trapping as H/G architectures, and reveal a simple synthesis route that can be applied to the fabrication of 2D donor/acceptor networks.

3.2. Results and discussions

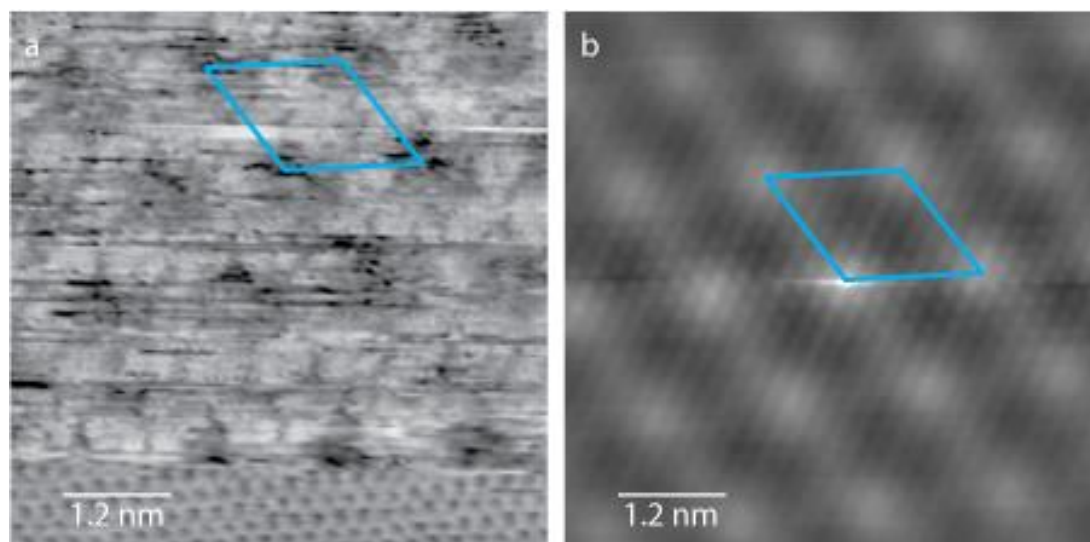


Figure 3.1 (a) Image revealing molecular resolution of the COF-1 structure (top) and atomic resolution of the underlying HOPG (bottom). Image conditions: bias voltage $V=-800$ mV, tunneling current $I=100$ pA (top); $V=-19$ mV, $I=1000$ pA (bottom). (b)

Autocorrelation of the image shown in (a). The small lattice (HOPG) and the large lattice (COF-1) have a clear commensurate relationship. The COF-1 aligns with the HOPG along both lattice directions, with each unit vector having an identical length of six HOPG lattice constants.

The COF-1 template was prepared on HOPG according to methods previously described in the literature (see Experimental Methods).⁴⁹⁻⁵⁰ Boroxine (B_3O_3) rings are formed through cyclocondensation of three BDBA monomers to produce an extended structure of COF-1, which consists of hexagonal cavities. STM measurements that simultaneously reveal the atomic lattice of HOPG and the COF-1 mesh indicate that COF-1 aligned with HOPG with a 6×6 epitaxial unit cell, as shown in *Figure 3.1*. This corresponds to a lattice parameter of 1.476 nm, and suggests a slight compression with respect to x-ray diffraction measured periodicity of 1.54 nm for bulk COF-1 solid.³⁹ In all experiments, the presence of COF-1 on the HOPG surface was confirmed using STM, which revealed the distinctive honeycomb lattice extending over domains tens of nanometers in size.

After confirming the presence of COF-1 on the surface, a solution of C_{60} fullerene in heptanoic acid was applied drop-wise to the COF. Following the application of the fullerene solution, COF-1 was still evident in STM images, and stable adsorption of fullerenes was observed.

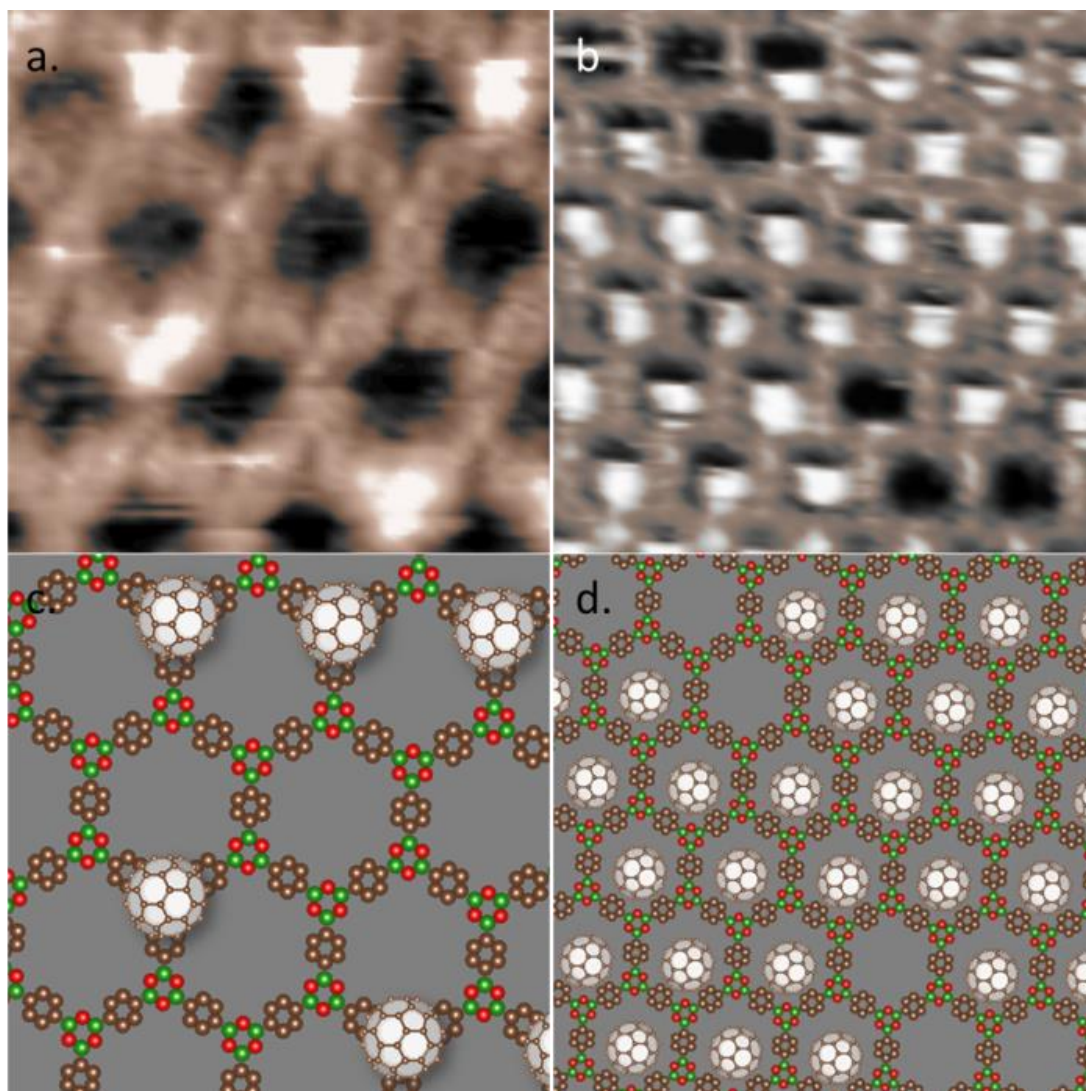


Figure 3.2 *H/G structures at the solution/solid interface. The images in (a) and (b) show the observed fullerene adsorption geometries, denoted as top site and pore site, respectively. The structures in (c) and (d) show proposed models for these adsorption sites. Scanning conditions: bias voltage $V=-800$ mV, tunneling current $I=100$ pA. Image widths (a) 5.3 nm and (b) 7.7 nm.*

Using a dilute fullerene solution (2×10^{-5} M), a relatively low fullerene guest occupation density was obtained, allowing the position of the fullerene guest

molecules to be discerned clearly, as shown in *Figure 3.2a* and *b*. Two different fullerene adsorption sites can be identified. In *Figure 3.2a*, COF-1 is discernible as a low-contrast hexagonal template, whereas bright protrusions indicate the positions of the fullerene molecules. In this image, the fullerene molecules do not lie within the pores of the host structure, as is typically observed for other systems;^{55, 60, 115} instead, each fullerene molecule is adsorbed on top of a boroxine ring of the COF. We denote this site, shown schematically in *Figure 3.2c*, as a top site. A similar adsorption on top of the host framework was observed for C₆₀ adsorption on oligothiophene macrocycles, where a stable 1:1 donor-acceptor complex is formed between the C₆₀ and the electron rich oligothiophene macrocycle.⁵⁴ Electrostatic forces are also significant in COF-1 as evident from the bulk 3D crystal structure of COF-1. The latter exhibits *ABAB* (staggered) packing of the 2D basal planes, which positions a benzene ring above each boroxine ring.³⁹

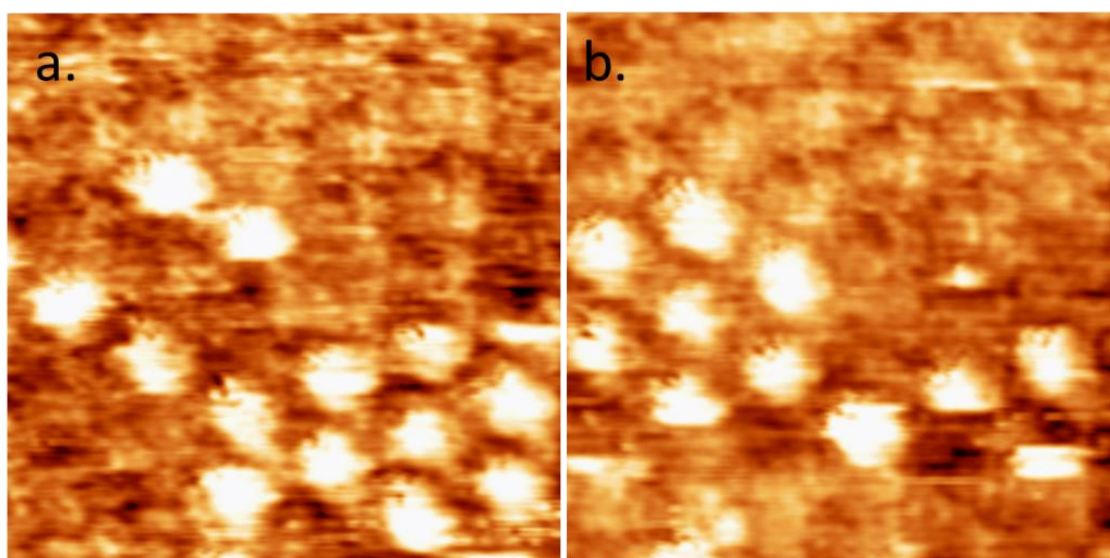


Figure 3.3 Consecutive STM images of H/G architecture: **(a)** the starting geometry with a small domain of C_{60} guest molecules inside the host template; **(b)** final geometry in the same area with C_{60} molecules in a new distribution which demonstrates a transfer of guest molecules induced by STM tip. Image width: 8.5 nm. Scanning conditions: bias voltage $V=-800$ mV, tunneling current $I=100$ pA.

The fullerene guests can also adsorb within the pores of the BDBA mesh. We denote this adsorption site as the pore site and assign it as slightly off-center within the BDBA pore (*Figure 3.2d*). In *Figure 3.2b*, the fullerene guests appear localized at the lower side of the COF-1 pores. Since this image was acquired by scanning in an upward direction, we interpret the asymmetric appearance of the guests as resulting from an off-centre adsorption (rather than, *e.g.*, attractive tip-sample interaction, which we would expect to lead to bright contrast at the top of the pores). The tip-sample interaction effect is shown in *Figure 3.3*. The adsorption site appears to occupy the same position within the pore for all fullerene guests observed in *Figure 3.2b*. We previously observed similar domain-wide positioning of fullerene guests in hydrogen-bonded oligothiophene host networks, where we attributed the domain-wide organization to the electrostatic ordering resulting from a partial charge transfer to the fullerene.⁸³

Although we did not perform a systematic study, we anecdotally observed a preference for top-site adsorption of fullerenes (top-site adsorption is observed approximately ten times more frequently than pore-site adsorption). Adsorption of

heptanoic acid within the pore, as has been postulated for other porous 2D nanostructures at the solution/solid interface,¹¹⁷ could affect the adsorption kinetics of pore-site fullerene, making top-site adsorption favourable (Discussed in chapter 4). Our molecular mechanics calculations (Section 3.5) suggest that pore-site fullerene adsorption is energetically preferred with respect to adsorption on the COF. Between the possible adsorption sites on the COF, adsorption over a boroxine ring is favoured with respect to adsorption over a phenyl ring. Gas-phase density DFT also indicate an energetic preference for fullerene adsorption over the boroxine compared to the benzene.

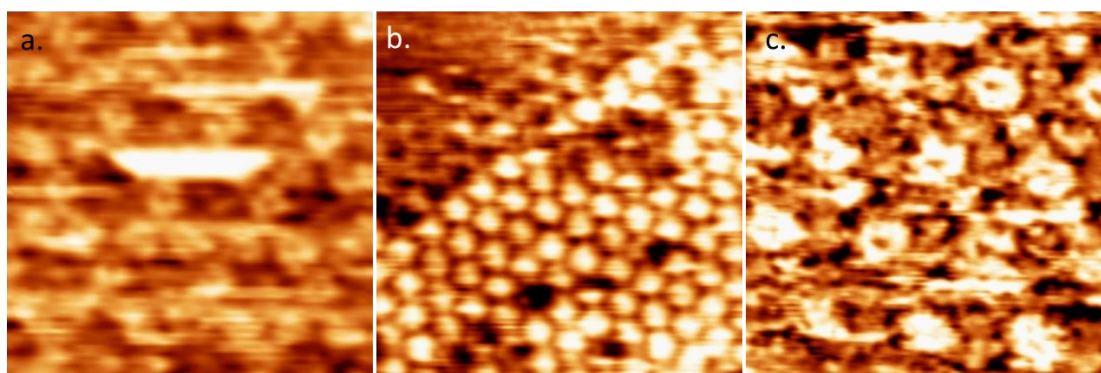


Figure 3.4 H/G structures at the air/solid interface. The images in (a) and (b) show top site adsorption and image in (c) shows pore site adsorption, respectively. (a) shows an isolated fullerene molecule and (b) is a stable domain of top site adsorption of C₆₀ molecules at air/solid interface. Imaging parameters: voltage $V=-800$ mV, tunneling current $I=100$ pA. Image width: (a) 5.6 nm (b) 17.2 nm (c) 5.4 nm.

We were able to obtain and image dried films of the COF-1/fullerene H/G system by allowing the solvent to evaporate in ambient, as shown in Figure 3.4. Figure 3.4a

demonstrates a difference between adsorption at the solution/solid interface and the air/solid interface: at the air/solid interface, and with sparse guest population, top-site C_{60} can be moved laterally along the rim of the COF by the STM tip. We could not similarly manipulate the top-site fullerenes at the solution/solid interface, suggesting that the solution may play a role in stabilizing the fullerenes in this site, or that the C_{60} can be easily removed to solution by the tip. We also found that the top-site fullerene guests in dried films could not be moved with the tip when the relative concentration of guest molecules was high, see *Figure 3.4b*, suggesting that isolated guest molecules are destabilized with respect to those contained in a regular lattice of guests.

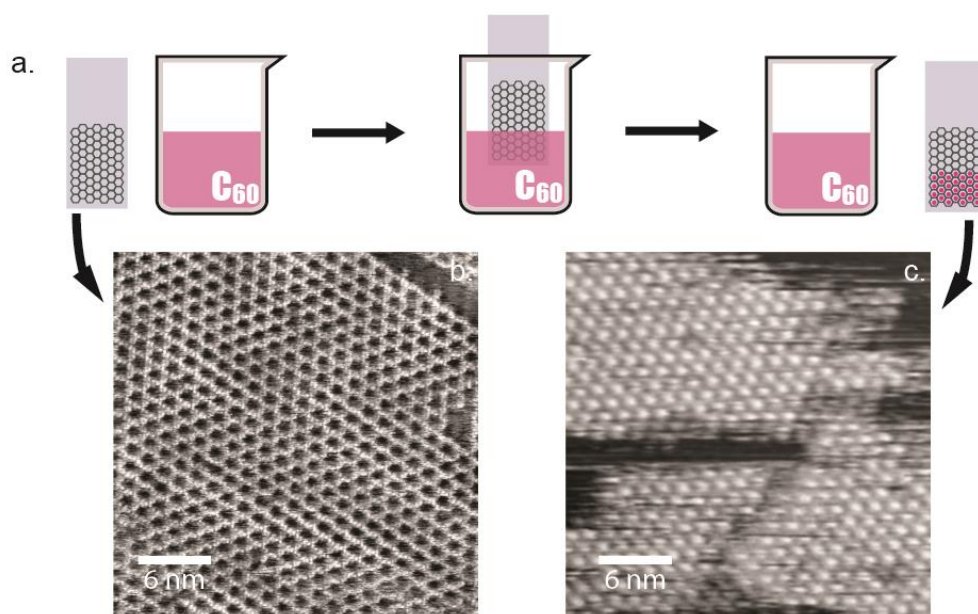


Figure 3.5 Schematic illustration of dipstick synthesis of COF-1/fullerene H/G structure. The image in (b) shows the as-synthesized COF-1 on HOPG. Following immersion into a solution of C_{60} in heptanoic acid (a) and subsequent drying, STM

images like that in (c) reveal COF-1 populated with C₆₀ guest molecules. Imaging parameters: voltage V=-800 mV, tunneling current I=100 pA.

The dried H/G monolayer could also be conveniently obtained through dipstick method: following the preparation of COF-1 on HOPG, the HOPG substrate was dipped vertically into a suspension of fullerene in heptanoic acid with a nominal concentration of 10⁻³ M. The substrate was held in the solution for less than five seconds, and was subsequently left to dry under ambient conditions for 12 hours (*Figure 3.5*). Images acquired after air drying (*Figure 3.5c*) revealed near complete occupancy of the COF-1 host by C₆₀ guest molecules. We conducted control experiments in which a HOPG substrate without COF-1 was dipped into a fullerene suspension of the same nominal concentration (10⁻³ M) and allowed to dry. In this case, STM imaging did not reveal any molecular structures at the surface. Instead, only typical HOPG features were present, suggesting that the stabilization of the fullerene molecules on the HOPG is dependent on the formation of a COF-1/fullerene H/G structure.

3.3. Conclusions and perspectives

We have shown that COF-1 can act as a robust host for C₆₀ fullerene guest molecules at the solution/solid interface and under ambient conditions, demonstrating the possibility for COF-based host/guest architectures at monolayer thickness. At both the solution/solid interface and in dried films, COF-1 presents a lattice with two distinct

fullerene adsorption sites: a pore site, where the C₆₀ molecule is adsorbed on the underlying HOPG, and a top site, where the fullerene is adsorbed on the boroxine ring. Dried COF-1/fullerene films can be produced either through drop deposition or by dipping the HOPG-supported COF-1 into the fullerene solution. The predictable trapping of fullerene molecules using COF-1 represents a proof-of-principle example of the utility of 2D boronic acid based COFs for applications in sensing or trapping molecules where the COF is exposed to a solution containing the target molecule. Since boronic acid derivatives can form a wide variety of template architectures with different functionalizations, this approach has an inherent flexibility that could be exploited to produce surface-mounted sensors amenable to integration into device architectures.

3.4. Experimental methods

Synthesis of BDBA COFs: BDBA COFs were formed following procedures described previously.⁴⁹⁻⁵⁰ 1 mg of 1,4-benzenediboronic acid (Tokyo Chemical Industry Co. Ltd) was added to 1.5 ml heptanoic acid (99%, Sigma- Aldrich), and then sonicated for approximately 30 min. This produced a whitish suspension 7.5 μl of this BDBA suspension was dropped onto freshly cleaved HOPG (Structure Probe International, grade SPI-2) and put into a reactor with a volume of ~16 ml. 130 μl deionized water was added to the bottom of the reactor, and a valve to ambient was left slightly open to maintain an open system. The entire reactor was placed in an

oven preheated to 125 °C and left for 60 min. After the thermal treatment, the reactor was taken out of oven and allowed to cool for at least 20 min before the samples were removed. Subsequently, the samples were characterized by scanning tunnelling microscopy at the solid/air interface.

H/G synthesis by drop-casting: Following the experiment of drop-wise test, 10 µl of a solution of fullerene (99.5%, Sigma- Aldrich) in heptanoic acid (99%, Sigma- Aldrich) with a concentration of 2×10^{-5} M, close to saturation,¹¹⁸ was applied onto a substrate with a previously-grown BDBA COF. Dried films were formed by leaving these same samples in ambient for 12-16 hours.

H/G synthesis by dipstick: Following the experiment of dipstick test, the HOPG substrate with preparation of BDBA COFs was dipped into a suspension of fullerene (10^{-3} M) in heptanoic acid. The HOPG was held in the solution for less than five seconds and was subsequently left to dry under ambient conditions for 12 hours.

STM measurements: STM was performed at room temperature under ambient conditions, using a Digital Instruments STM equipped with a Nanoscope IIIa controller. Tips were cut from Pt_{0.8}Ir_{0.2} wire (Nanoscience Instruments). Bias voltages are reported with respect to the STM tip. STM images were processed using the free WSxM software.¹¹⁹ The images were rendered using the standard grayscale color mapping, after which false colour (brown) was overlaid on the COF-1 in *Figure 3.2*.

3.5. Calculations

Adsorption geometries for fullerene adsorption were investigated using molecular mechanics calculations using MM+ as implemented in HyperChem.⁵ A cluster representing COF-1 was placed on top of larger hexagonal graphene cluster (*Figure 3.6*) all coordinates of which were frozen. The optimization was run until the energy change was <0.000001 kcal/mol over 100 cycles. The achieved gradient was <0.02 kcal/mol/Å (in most cases <0.01 kcal/mol/Å).

The COF-1 was found to be the most stable with its unit cell vector coaligned with the graphene zigzag direction. Alignment along the armchair direction was disfavoured by 0.2 kcal/mol. Although the structure for the COF-1 pore does not reflect the exact epitaxial relationship identified in our experiments, we expect that the geometry used in these calculations correctly captures the relative energetics between the different adsorption sites.

Fullerene adsorption was examined for the pore site, and for two possible top site adsorptions: over a boroxine ring and over a phenyl ring in the COF-1. In all cases, C₆₀ is most stable when adsorbed with a hexagonal ring facing down.

The most stable adsorption was found to be in the pore site, at $E_b = -32.1$ kcal/mol. This was followed by adsorption in a boroxine top site ($E_b = -11.2$ kcal/mol) and finally a benzene top site ($E_b = -10.2$ kcal/mol). The calculated geometries are shown in *Figure 3.6*.

Using gas-phase density functional theory (DFT), as implemented in the Gaussian09

software,¹³⁹ we considered the adsorption geometries of the fullerene molecules above the COF-1 pore. Since the graphene layer was not included in these calculations, several dihedral angles were frozen in the COF-1 pore in the vicinity of the fullerene. Calculations were performed at the B3LYP/6-31G level, which we do not expect to capture all relevant dispersive interactions. B3LYP Calculations of the fullerene/COF-1 geometries converged with respect to forces (both force and root-mean-square force) and revealed the same relative energetics indicated by the molecular mechanics calculations: adsorption above the boroxine was favoured as compared to adsorption above the benzene (calculated E_b values were -1.31 kcal/mol for adsorption above boroxine and -0.48 kcal/mol for adsorption above benzene).

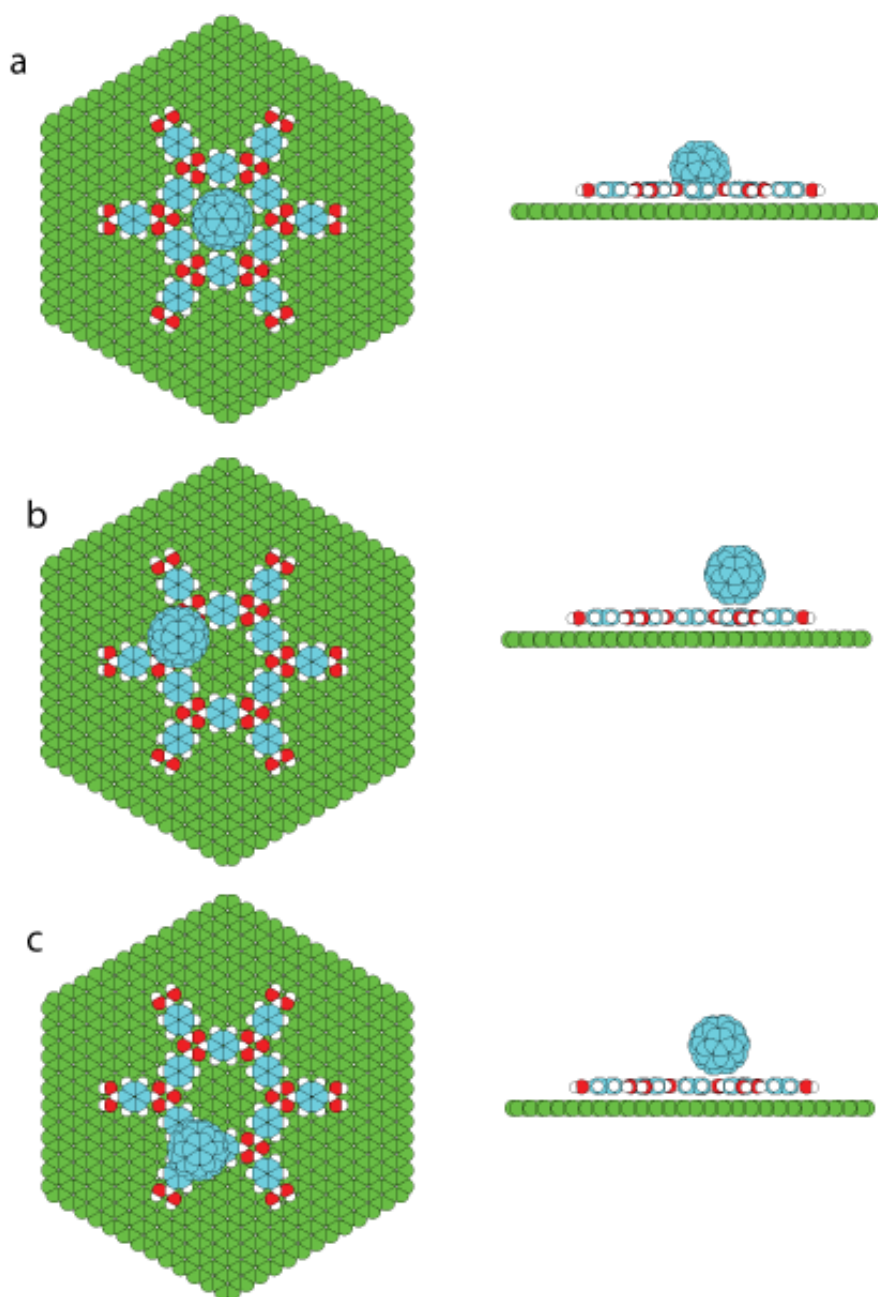


Figure 3.6 molecular mechanics calculated geometries for pore site adsorption (a), top site adsorption over a phenyl ring (b) and top site adsorption over a boroxine ring (c). Oxygen atoms are represented by red, carbon atoms (fullerene and COFs) are represented by blue and carbon atoms (graphite) are represented by green.

Chapter 4. Selective binding in different adsorption sites of a 2D covalent organic framework template

Daling Cui, Jennifer M. Macleod, Maryam Ebrahimi and Federico Rosei.
CrystEngComm, **2017**, *19*, 4927-4932.

Daling Cui's contributions: the creation of original idea, the collection and analysis of data, drafting manuscript.

4.1. Introduction

H/G chemistry in two-dimensional (2D) supramolecular networks has been extensively studied as a means to immobilize a variety of guest molecules, with potential applications in separation technology, molecular recognition, sensing, catalysis and nanoscale patterning.^{22, 120} In general, H/G networks rely on hierarchical interactions: the interaction binding the host together is stronger than the interaction binding the guest to the host. The host networks are typically sustained by hydrogen bonding,^{55, 74, 76, 83} vdW forces,^{54, 121} or metal-ligand interaction,¹¹⁶ whereas the adsorption of guest molecules mainly occurs *via* weaker interactions, typically London dispersion forces with the host as well as with the underlying substrate. However, moving away from self-assembled templates may offer some new opportunities for the stabilization of guest molecules. 2D COFs have recently been explored as host system,^{80, 122-123} opening the possibility of using stronger interactions to stabilize molecules into the pores. COF-1, a well ordered 2D porous material that

can be synthesized through the on-surface polycondensation of BDBA,⁵⁰ is a promising candidate for this application.

The mutually specific recognition between the host network and the guest molecules, *i.e.*, a form of molecular recognition, is at the core of host–guest chemistry.¹²⁴⁻¹²⁵

Design strategies for selectivity in guest bonding have often relied on tuning the host geometry, such as pore size⁶⁰⁻⁶¹, shape⁶² and chirality.⁶⁴ Much less is known about how to use the interaction between host and guest.¹²⁶ This is mainly due to limitations of hierarchical interaction strength imposed by self-assembled host templates. This aspect can be addressed by using a covalently-bonded template, such as COF-1, which enables a route to molecular recognition through a range of different interactions, including hydrogen bonding, halogen bonding or vdW interactions.

Here, we show that a template of COF-1 can host 1,2,4-trichlorobenzene (TCB) guest molecules that are stabilized through X...H hydrogen bonding. The adsorption is enabled through a combination of factors, including host pore size and shape, and specific stereochemical arrangement of binding sites. By introducing a solution of C₆₀ in TCB onto the COF-1 template, we observe that selective adsorption of C₆₀ on the top-sites of the COF-1 template is obtained simultaneously by trapping TCB within the pore-site. This work demonstrates a strategy to separate and recognize molecules through different interactions within a covalent porous 2D template.

4.2. Results and discussions

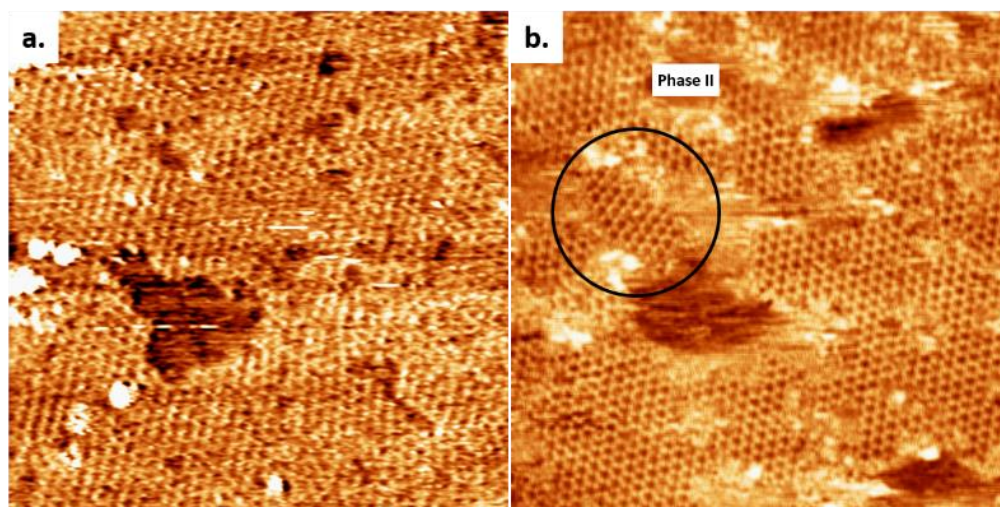


Figure 4.1 (a) STM image of COF-1 synthesized in TCB, collected at the air/solid interface. Image width: 60 nm. Scanning conditions: $V = -1000$ mV, $I = 100$ pA. (b) STM image of COF-1 synthesized in heptanoic acid, collected at the interface of heptanoic acid and HOPG. A small domain of Phase II is marked by black circle. Image width: 60 nm. Scanning conditions: $V = -800$ mV, $I = 100$ pA.

Using TCB as solvent, the synthesis of COF-1 on HOPG produces a high density of small domains across the surface, as shown in *Figure 4.1a*. The obtained surface-confined porous network is qualitatively identical to the one formed using heptanoic acid as solvent.⁸⁰ In both cases, the large COF sheets appear to comprise multiple domains that have grown together, leaving disordered regions evident at the domain boundaries. However, when using TCB, we also observed ordered domain boundaries, as described below.

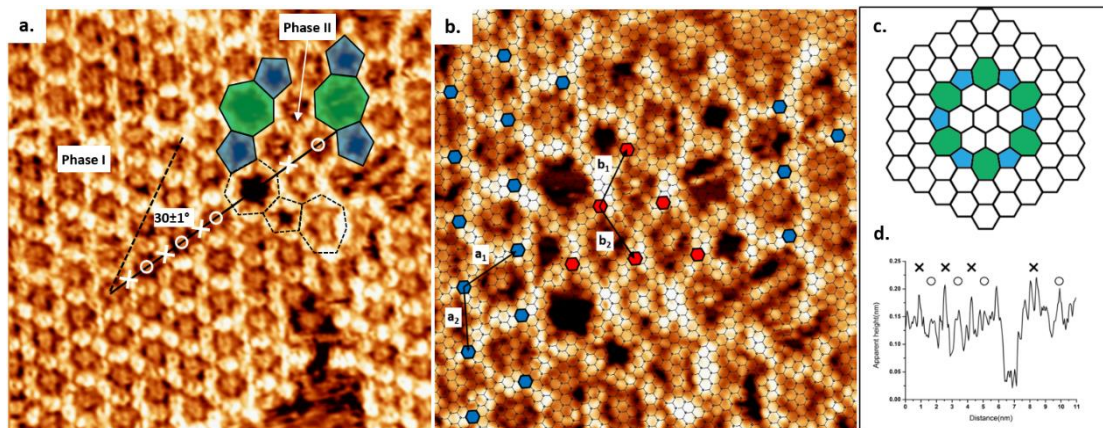


Figure 4.2 (a) COF-1 STM image showing the grain boundary consisting of pentagon and heptagon rings, connecting two domains rotated by $30\pm 1^\circ$ with respect to one another, as shown by the dashed and solid black lines. The image was collected at the interface of TCB and HOPG. Image width: 15 nm. Scanning conditions: $V = -1000$ mV, $I = 100$ pA. (b) The epitaxy of COF-1 and HOPG at grain boundary region. Phase I: $a_1 = a_2 = 1.476$ nm; Phase II: $b_1 = b_2 = 1.42$ nm. Image width: 9.6 nm. (c) Schematic structure of the rotational grain boundary identified in (b), i.e., a loop defect with C_6 symmetry. Five- and sevenfold rings are shaded by blue and green, respectively. (d) Line profile of the measured height along the black solid line in (a). The positions of benzene rings in COF-1 are marked as \times and the positions of adsorbed TCB molecules are marked as \circ .

As shown in *Figure 4.2a*, the COF-1 polycrystalline film synthesized in TCB comprises two different domain orientations tilted at an angle $\alpha = 30\pm 1^\circ$ to each other and separated by a grain boundary (GB). In our analysis of the epitaxial relationship of COF-1 and HOPG (*Figure 4.2b*), we attribute the dominant domain as Phase I, i.e.,

the COF-1 lattice aligned with HOPG with a 6×6 epitaxial unit cell, which corresponds to a lattice parameter of $a_1=1.476$ nm, as reported in previous work.⁸⁰ The lattice of Phase I is represented by small blue hexagons in *Figure 4.2b*. The smaller domain is denoted as Phase II. The orientation of this domain, along the HOPG armchair direction, is nearly commensurate for a 10×10 superstructure (corresponding to 3×3 unit cells). We previously calculated that the phase II epitaxial orientation of COF-1 should be energetically disfavoured,⁸⁰ consistent with our infrequent experimental observation of the phase. Phase II has also occasionally been observed for COF-1 synthesized from heptanoic acid (See *Figure 4.1b*)

The GB region in *Figure 4.2* consists of elementary topological defects, pentagons (shaded blue) and heptagons (shaded green). These defects represent some of the basic building blocks of the disordered COF-1 network that have been observed on oriented noble metal surfaces under UHV,^{43, 46} where the random distribution of these topological defects can be attributed to kinetic trapping during synthesis, since the water-driven self-correction mechanism is not available under UHV conditions. However, the ordered pentagonal/heptagonal defects that we observe in this work are directly analogous to defects formed in another single layer covalent system, *i.e.*, single layer graphene.¹²⁷⁻¹²⁹ According to the atomic model proposed by Cockayne *et al.*,¹³⁰ the chain of alternating pentagon and heptagon defects is consistent with a loop GB of graphene, as shown in *Figure 4.2c*. Compared with the linear GB, reported by Xu *et al.* in COFs formed by benzene-1,3,5-tricarbaldehyde (BTA) and

p-phenylenediamine (PDA),¹³¹ the loop defect boundary has the lowest energy per dislocation core, suggesting that this defect is likely to form under conditions where mobile dislocations exist. This is consistent with our COF-1 synthesis method, since defect correction within the COF lattice leads to improved structural order under humid synthesis conditions.⁵⁰ In our case this translates to the minimization of energy at domain boundaries through the inclusion of well-defined Stone-Wales type defects.¹²⁷

The presence of the loop boundary defect enables us to identify the adsorption of TCB in the COF-1 pore. *Figure 4.2d* shows the apparent height profile along the zigzag direction of Phase I COF-1 lattice (the black solid line in *Figure 4.2a*). The adsorption of TCB in hexagonal rings can be clearly distinguished by comparison with the apparent height of the heptagonal ring.

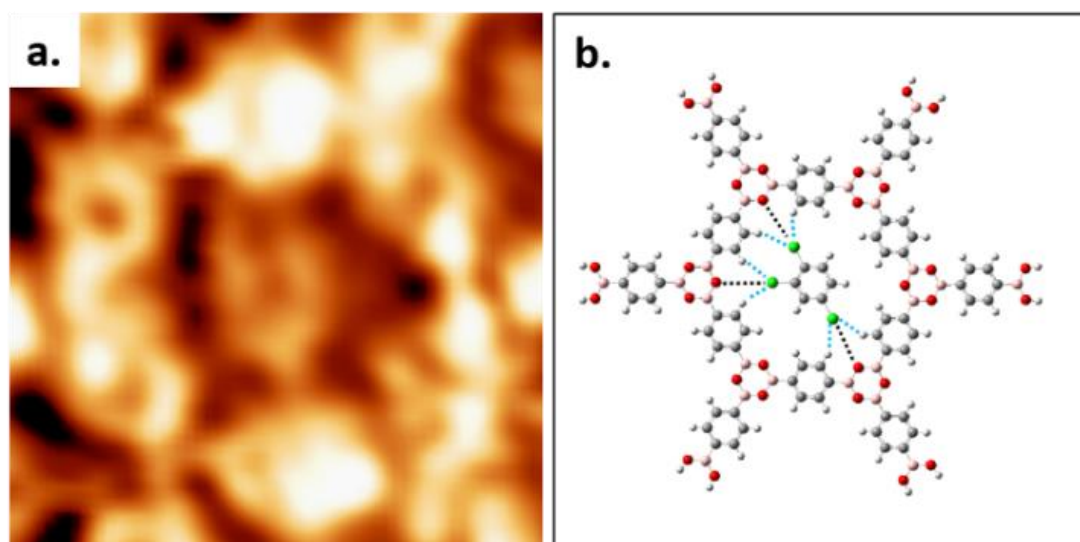


Figure 4.3 (a) The detailed STM image of one TCB molecule adsorbing into the hexagonal ring formed by COF-1. Image width: 2.1 nm. Scanning conditions: $V=$

-1000 mV, $I = 100$ pA. (b) DFT-calculated structure of one TCB in hexagonal pore (M06-2X/LANL2DZ). Dashed blue and black lines represent the interactions of Cl...H and Cl...O, respectively.

High resolution STM images allow us to elucidate the host-guest structure formed by the hexagonal pore of COF-1 and TCB molecule, as shown in *Figure 4.3a*. The six phenyl rings in the backbone of COF-1 can be easily distinguished, as are submolecular features associated with the adsorbed TCB molecule. These features may correspond to the three chlorine atoms or contrast of the benzene ring, and their presence suggests stable adsorption of the TCB molecule (*i.e.* that the molecule is not rotating).⁵⁹ Our gas-phase DFT calculations suggest that the TCB adsorption is stabilized through Cl...H hydrogen bonding interactions, as indicated in *Figure 4.3b*; consistent with previous work, we identify these interactions through Cl...H distances that are shorter than the sum of the Cl and H vdW radii, as shown in Table 4.1.¹³²⁻¹³³ The electron density associated with the chlorine atoms in the TCB molecule is anisotropically distributed, as shown in *Figure 4.6*.¹³⁴ The nucleophilic belt orthogonal to the covalent bond, with higher electron density and showing negative electrostatic potential, forms X...H hydrogen bonds with neighboring hydrogen atoms on the COF-1 backbone (dashed blue line).¹³⁵ Although the σ -hole of the chlorine atoms points toward the nucleophilic oxygen atom of the COF-1 (dotted black line in *Figure 4.3b*), the interaction between the chlorine and the oxygen is screened by the hydrogens on the phenyl rings, as shown in *Figure 4.6*. Our DFT calculation confirms

that the chlorine-oxygen distance is too large ($\sim 4.38 \text{ \AA}$) to allow significant interaction.

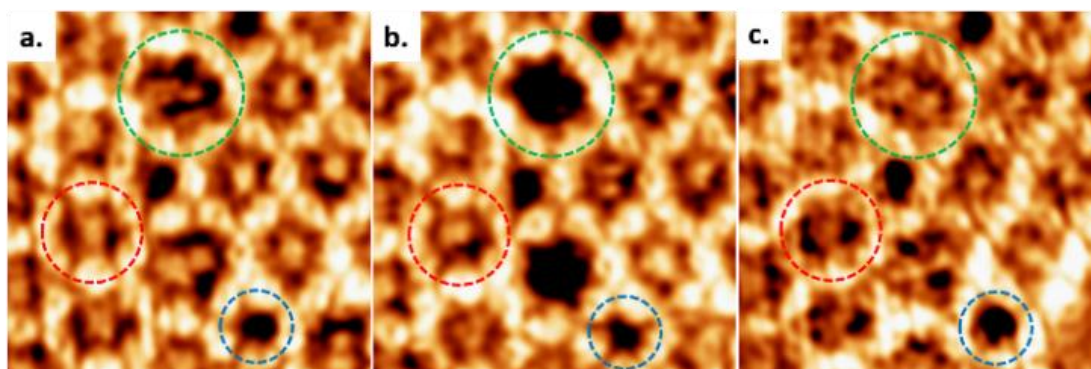


Figure 4.4 (a-c) The sequential collection of STM images showing the evolution of adsorption of TCB in the grain boundary defects. Different geometries are marked by different dashed color circle: heptagonal ring (green circle); hexagonal ring (red circle); pentagonal ring (blue circle). Image width: 5.8 nm. Scanning conditions: $V = -1000 \text{ mV}$, $I = 100 \text{ pA}$.

The presence of the pentagonal/heptagonal defects at the GB allows us to explore the topological and pore size dependence of the guest molecule adsorption. In previous work, fullerene guest molecules were shown to preferentially adsorb in the irregularly-shaped pores present at domain boundaries in a nanoporous hydrogen-bonded network of TMA.⁸¹ However, in contrast to the TMA network where the domain boundary dynamically evolves,¹³⁶ the loop defects in COF-1 are stable during STM scanning and present a well-defined molecular template, as shown in *Figure 4.4*. The diameters of pentagonal rings (blue dashed line) and heptagonal rings (green dashed line) are 1.381 nm and 1.959 nm respectively, as compared to the

hexagonal pore size (red dashed line) of 1.758 nm.⁴⁶ Pores of different sizes can adsorb different numbers of guest molecules, as shown in *Figure 4.4a-c*. There is no adsorption of TCB in pentagonal rings; basic considerations reveal that a TCB molecule cannot be included in this pore without creating interference between hydrogen atoms on the TCB and the pentagonal ring (multiple H...H contacts with distances smaller than twice the hydrogen vdW radius), as shown in *Figure 4.7*.

Two TCB molecules can adsorb simultaneously in the heptagonal pore, as shown in *Figure 4.4*. The adsorption of a different number of guest molecules within different pore sizes drives from the commensurability of host and guest molecules. Networks with sufficiently large cavities can host clusters of molecules.^{76, 82, 116} The adsorption of TCB in porous self-assembled networks has been reported previously for large-pore self-assembled templates,^{26, 61} including instances where TCB was trapped in close-packed domains within the pore.^{26, 137} In the present study, DFT calculations suggest that both inter-TCB Cl...Cl interactions and TCB-COF Cl...H interactions stabilize the adsorption of the TCB pair within the heptagonal pore (*Figure 4.8*).

The occupation states of the pentagonal and hexagonal pores appear unchanged with time under STM scanning: the pentagonal pores remained empty, whereas the hexagonal pores retain a single TCB molecule. Conversely, the adsorption of TCB molecules in heptagonal rings exhibits dynamical change. The adsorption-desorption-readsorption process of two TCB molecules can be clearly distinguished in STM images, as marked by green circles in *Figure 4.4a-c*. Although

both empty pores and double-occupied pores were observed, we did not detect the intermediate state, *i.e.*, single TCB adsorbed in a heptagonal ring. The most likely explanation for this is the relatively weak stabilization for an individual TCB molecule in a heptagonal pore. Unlike the matched symmetry between the TCB and the hexagonal pore, the reduced symmetry of the heptagonal pore is a poor match for the TCB molecule, reducing the number of possible Cl...H contacts for a single molecule, and rendering single-molecule adsorption unfavourable.

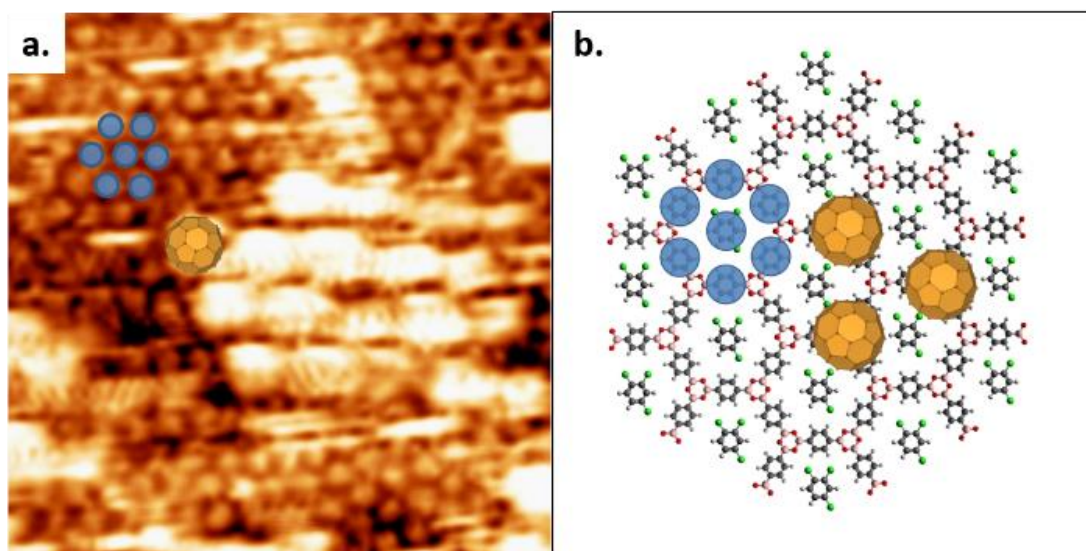


Figure 4.5 (a) The top-site selective formation in $C_{60}/COF-1$ system. Image width: 12 nm. Scanning conditions: $V = -800$ mV, $I = 100$ pA. (b) Schematic image of top-site selective formation in $C_{60}/COF-1$ system. The shaded blue circles over benzene rings represent the closed packed background in STM image. Top-site C_{60} molecules are placed over boroxine rings, corresponding to the large bright spots in (a).

Previous work showed that C_{60} introduced from solution containing heptanoic acid as solvent adsorbs on the COF-1 template in two different sites, the top-site and

pore-site.⁸⁰ The top-site geometry corresponds to the adsorption of fullerene molecule on the boroxine ring and pore-site corresponds to the adsorption of a fullerene molecule in the hexagonal pore. Our present experiments reveal that C₆₀ introduced from solution in TCB exhibits a different behaviour, as shown in *Figure 4.5a*. Our interpretation of the STM data is shown in *Figure 4.5b*, that is consistent with the results obtained in the absence of C₆₀. Therefore, we attribute the tightly-packed hexagonal pattern to TCB molecules adsorbed in the COF-1 pores (indicated as shaded blue circles in *Figure 4.5a* and *b*), and the high-contrast, larger-periodicity hexagonal domain to C₆₀ molecules adsorbed on top-sites. The top-site adsorption of C₆₀ is consistent with the calculated geometry, where the architecture is stabilized by vdW interactions.⁸⁰

The growing body of literature on H/G architectures based on COF-1 suggests that the solvent used for C₆₀ deposition plays an important role in the adsorption of the guest molecules. Plas' work shows that C₆₀ molecules grow layer-by-layer sequentially from COF-1 template dispersed in 1-phenyloctane, suggesting that the solvent does not compete with C₆₀ for adsorption in the pore site.¹²² Using heptanoic acid as solvent, we anecdotally observed a preference for top-site adsorption of fullerenes, suggesting that heptanoic acid may compete for adsorption in the pore-site. Combined with the present results, this suggests that the solvent can be used to select the initial adsorption site for fullerenes, that is TCB and 1-phenyloctane will select for top-site and pore-site adsorption, respectively; whereas heptanoic acid cannot predictably

select between the adsorption sites.

4.3. Conclusions and perspectives

A 2D porous COF-1 layer was synthesized on HOPG from solution in TCB. Two different epitaxial orientations of COF-1 were observed, with a well-defined loop boundary defect formed by a chain of pentagonal ring and heptagonal ring separating the two domain orientations. STM images collected at the TCB/solid interface reveal the adsorption of TCB within the hexagonal pores of the COF-1 template. Our DFT calculations show that this host/guest structure is stabilized by Cl...H hydrogen bonding. The presence of the loop boundary defect permitted the investigation of the effect of pore shape and size on TCB adsorption: no TCB was adsorbed in the pentagonal pores, but the larger heptagonal pores accommodated two TCB molecules, stabilized through a combination of Cl...H and Cl...Cl bonding. Including C₆₀ in the TCB solution allowed us to investigate the molecular recognition of template. When both C₆₀ and TCB are present at the solution/solid interface, TCB molecules are selectively trapped in the pores of the COF-1 template, whereas fullerenes adsorb on top of the COF-1 in sites identified as top sites. The selective adsorption of TCB and C₆₀ in COF-1 suggests that the different adsorption sites in the COF-1 lattice can be used to separate guest molecules by different interactions, opening opportunities for applications in molecular patterning and recognition.

4.4. Experimental methods

Synthesis of BDBA COFs: Monolayer COF-1 on HOPG was formed through a modification of procedures described previously, where heptanoic acid was used as solvent.⁴⁹⁻⁵⁰ In the present experiments, 1.8 mg of 1,4-benzenediboronic acid (Tokyo Chemical Industry Co. Ltd) was added to 1.2 ml 1,2,4-trichlorobezene (99%, Sigma-Aldrich), and then sonicated for approximately 30 min. This produced a whitish suspension. 15 μ l of this BDBA suspension was dropped onto freshly cleaved HOPG (Structure Probe International, grade SPI-2) and placed into a reactor with a volume of ~16 ml. 130 μ l of deionized water was added to the bottom of the reactor, and a valve to ambient was left slightly open to maintain an open system. The entire reactor was placed in an oven preheated to 125 °C and left for 60 min. After the thermal treatment, the reactor was taken out of the oven and allowed to cool down for at least 20 min before the samples were removed.

H/G synthesis: Following the confirmation of monolayer COF-1 on the HOPG surface using STM, 15 μ l of 1,2,4-TCB (99%, Sigma-Aldrich) was applied onto the substrate. Subsequently, the samples were characterized by STM at the solvent/solid interface. To investigate the adsorption of fullerenes, 15 μ l supernatant solution of C₆₀ (99.5%, Sigma- Aldrich) in 1,2,4-TCB was applied onto a pre-prepared COF-1 template.

STM measurements: STM was performed at room temperature at the liquid-solid interface, using a Digital Instruments STM equipped with a Nanoscope IIIa controller.

Tips were cut from Pt_{0.8}Ir_{0.2} wire (Nanoscience Instruments). Bias voltages are reported with respect to the STM tip. STM images were calibrated with COF-1 lattice parameter (1.476 nm) using the free WSxM software¹¹⁹.

4.5. Calculations

Gas-phase DFT calculations were carried out using Gaussian09.¹³⁸ In previous work, we compared the performance of a number of functionals and basis sets for calculations of self-assembled systems comprising X...H and X...X interactions,^{27, 133} and found that the combination of M06-2X¹³⁹/LANL2DZ provides an accurate description of energies for halogen-bonded systems. The M06 functionals are known to be more accurate for systems involving non-covalent interactions and hence were chosen for the description of halogen-bonded system. To simulate surface adsorption, all geometries were constrained to remain planar.

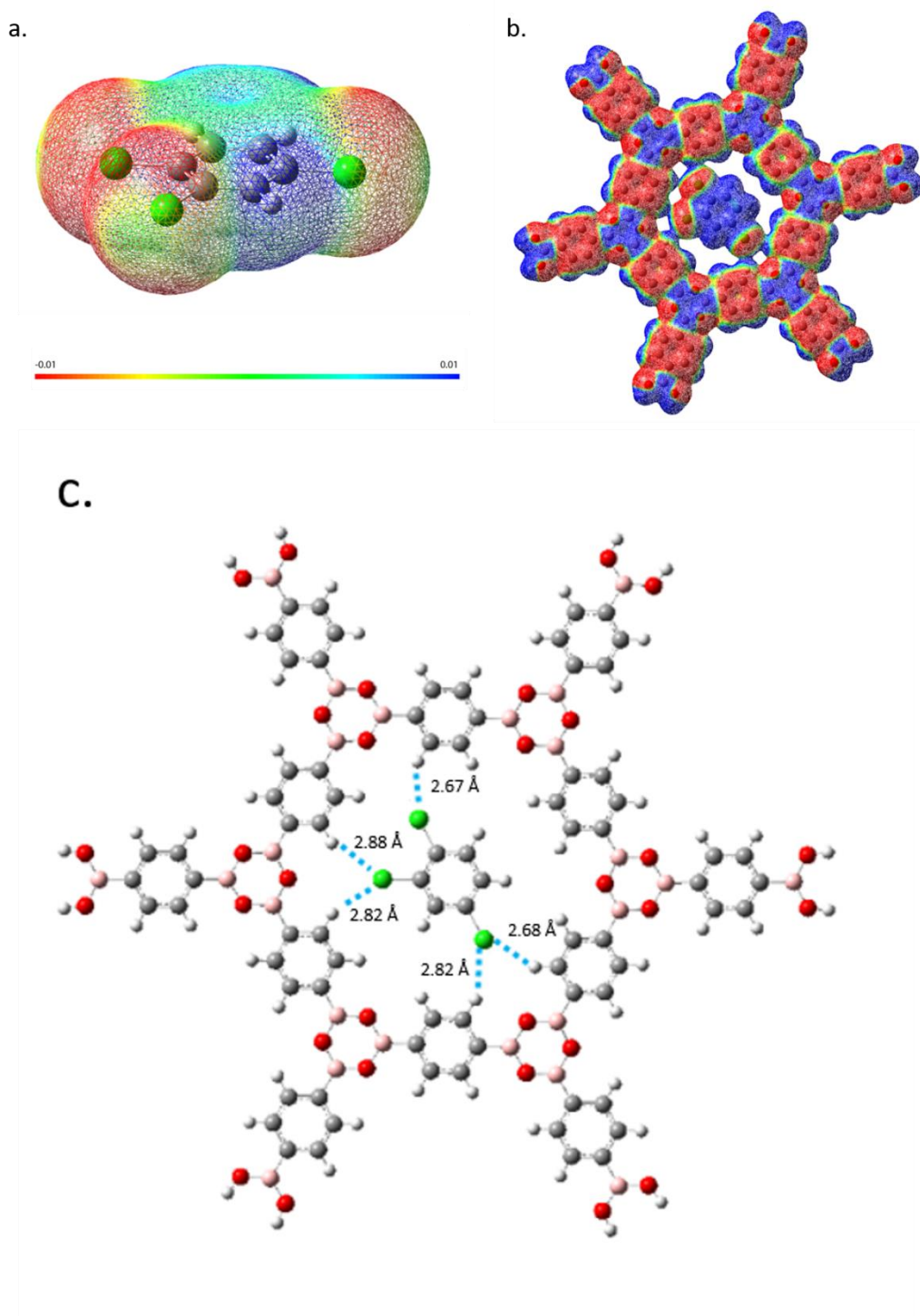


Figure 4.6 (a) Molecular electrostatic potential (ESP) map (M06-2X/LANL2DZ) for isolated TCB in the gas phase (3D view). (b) Molecular ESP map of optimized geometry (M06-2X/LANL2DZ) for TCB in COF-1 hexagonal pore. The ESP maps for a

and b are expressed in atomic units (a.u., Rydberg/ e) on $0.0004 e/\text{Bohr}^3$ and $0.004 e/\text{Bohr}^3$ isodensity surfaces, respectively. The color scale from blue (+ve) to red (-ve) spans the following ranges: ± 0.01 a.u. for both a and b . (c) Optimized geometry of one TCB in hexagonal pore (M06-2X/LANL2DZ), with marking the distances of Cl...H (dashed blue line) interatomic contacts. (Only showing the distances less than the sum of the vdW radii for Cl...H contacts)

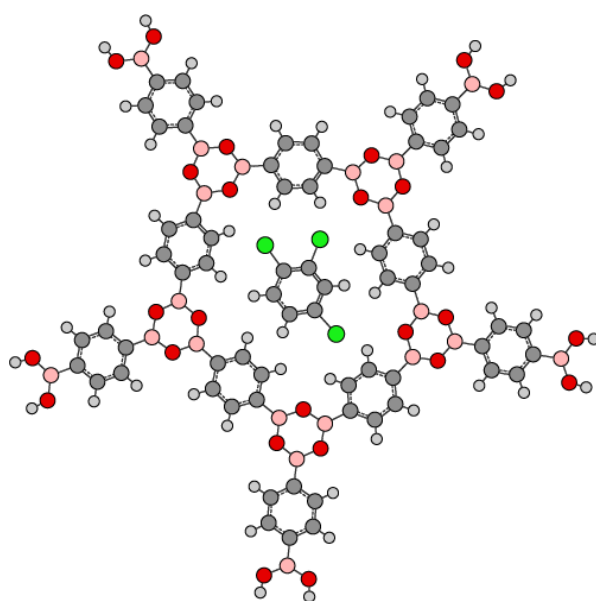


Figure 4.7 Indicative geometry for TCB in pentagonal pore. All H...H distances between hydrogens on the TCB molecule and hydrogens on the COF-1 pore are below 2 vdW radii for hydrogen ($2r_H=2.4 \text{ \AA}$),¹⁴⁰ suggesting that the TCB molecule cannot be accommodated in a planar adsorption geometry in the pentagonal pore.

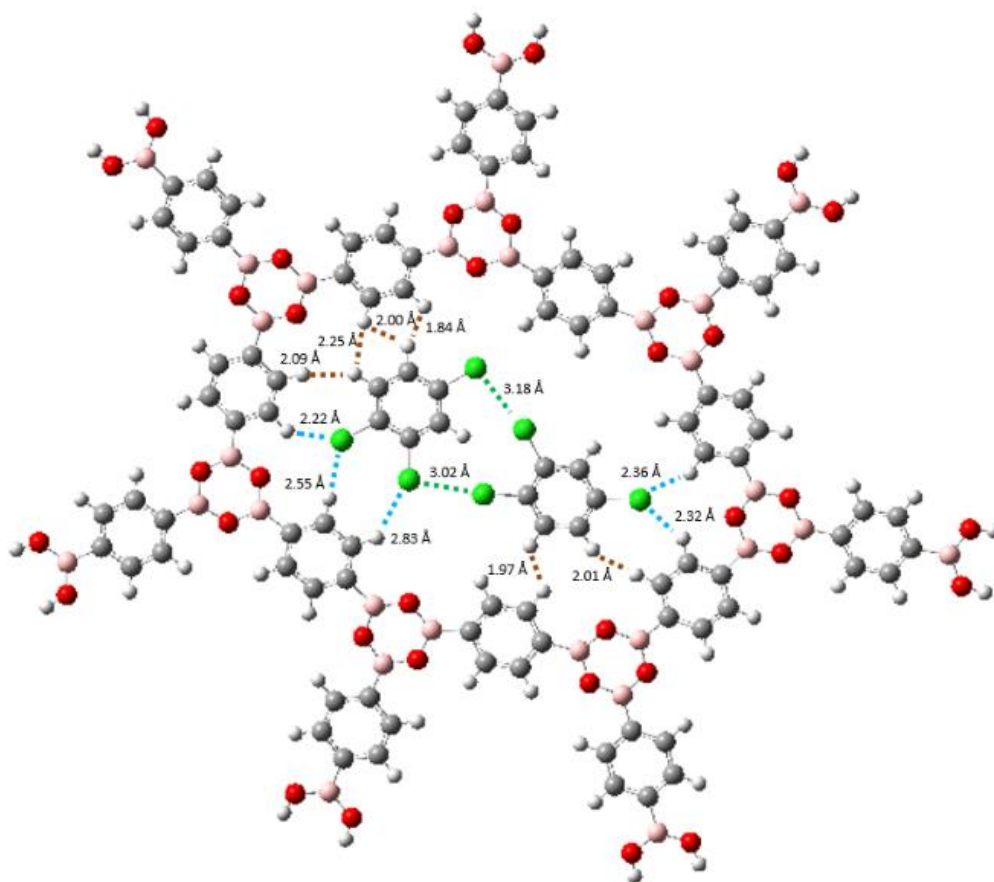


Figure 4.8 Optimized geometry for two TCB molecules in a heptagonal pore. This geometry allows for Cl...H (dashed blue line) interactions between the TCB and the COF-1 pore as well as Cl...Cl (dashed green line) interactions between the two TCB molecules. However, bond distances for Cl...H interactions are shorter than expected (i.e., shorter than the optimized distances found for a single TCB in a hexagonal pore, see Table 4.1), and unfavourably short H...H (dashed brown line) interactions exist between hydrogen atoms on the TCB molecules and the COF-1 pore (i.e., distances shorter than $2r_{\text{H}}=2.4 \text{ \AA}$). These closer interactions suggest that perhaps the epitaxial

heptagonal pore is expanded somewhat from the gas-phase dimensions reflected in this geometry. The inter-atom distances for Cl...Cl, Cl...H and H...H are marked accordingly. (Only showing those less than the sum of the vdW radii)

Table 4.1 Van der Waals radii¹⁴⁰ and calculated inter-atom distance*

	Van der Waals radii					Calculated inter-atom distance		
	r_H	r_{Cl}	$2r_H$	$r_H + r_{Cl}$	$2r_{Cl}$	d_{H-H}	d_{H-Cl}	d_{Cl-Cl}
TCB/hexagon	1.20 Å	1.75 Å	2.40 Å	2.95 Å	3.50 Å	N/A	2.67 Å	N/A
TCB/heptagon						1.84 Å	2.22 Å	3.02 Å

*The inter-atom distances in Table 4.1 are reported by selecting smallest value in calculation for each case. For detailed data list, please check corresponding calculated graphics.

Chapter 5. Control of fullerene crystallization from 2D to 3D through combined solvent and template effects

Daling Cui, Maryam Ebrahimi, Federico Rosei, Jennifer M. Macleod. *J. Am. Chem. Soc.* **2017**, *139*, 16732-16740.

Daling Cui's contributions: the creation of original idea, the collection and analysis of data, drafting manuscript.

5.1. Introduction

Understanding structure-property relationships of materials is a central objective of nanoscience. This understanding is particularly critical when a molecule or compound can aggregate in different crystalline phases, *i.e.* polymorphs, which exhibit altered physical or chemical properties.¹⁴¹⁻¹⁴³ Predicting the occurrence of polymorphs and producing materials with unusual structures are two important challenges in materials science and engineering. Polymorphism is routinely observed in both 3D and 2D crystals. Several parameters can control the formation of polymorphs in molecular crystals, such as the solvent employed,^{35, 144-145} temperature,^{26, 143} and the presence or absence of a substrate that may facilitate epitaxial growth.^{23, 146-147}

In 2D, the use of STM permits the direct visualization of molecular architectures with

submolecular resolution, providing detailed insights into polymorphism.^{16, 148} Surface-confined 2D self-assembly can be used as a means to the controlled, atomically-precise nanofabrication of 3D objects¹⁴⁹ and is regarded as a promising strategy to increase overall device density in the third dimension.^{5, 150-151} This approach is well-suited for the realization of tailored polymorphs with out-of-plane anisotropy by bottom-up methods, effectively bridging the gap between 2D and 3D investigations.¹⁵²⁻¹⁵⁴

The growth of template networks, able to form H/G structures,^{22, 120} has proven to be an important approach for controlling crystallization into the third dimension using molecular building blocks. H/G structures rely on hierarchical interactions, in which the template is stabilized by relatively robust and directional interactions (such as hydrogen bonding and metal coordination) and guest molecules are templated through weaker interactions.^{25, 56, 116} In a monolayer 2D film, the architecture is governed by both the adsorptive interactions between the substrate and the deposited molecules (H and G)^{75, 155} and the intermolecular H/G interactions.⁷³⁻⁷⁴ Beyond the first layer, the structure is stabilized by intermolecular interactions alone. The formation of a bilayer H-bonded kagomé structure⁷³ and self-aggregation of π -stacked heterocirculenes⁷⁴ have been observed as examples of growth into the third dimension, perpendicular to the surface, starting from a 2D H/G layer. The use of non-planar guests, *e.g.*, fullerenes and their derivatives, when stabilized by weak interaction with 2D templates, can promote configurations that deviate from standard close-packing due to

the structure defined by the template.^{23, 75-78} The codependent relation between trapped fullerenes and the growth of a second layer of a supramolecular framework represents a cooperative interaction of H and G species.⁷⁹ Although these examples demonstrate the possibility of arranging molecules from 2D to 3D, defining the 3D spatial organization of films containing small molecules still remains an important challenge,¹⁵⁶ since small compounds without functional groups tend to lack directional interactions.¹⁵⁷⁻¹⁵⁸

The solvent effect is also a well-known factor that may lead to different polymorphs, through co-adsorption effects (known as pseudopolymorphism)¹⁵⁹⁻¹⁶¹ and solvent-induced polymorphism^{35, 37-38, 144} driven by thermodynamics or kinetics.^{34, 162} For example, different polymorphs of TMA and BTB³⁷⁻³⁸ were observed subject to the solvent used. The solvent dependence of the formation of the molecular adlayers has been examined in terms of the properties of the solvents (polarity, solvophobicity, solubility *etc.*),³⁵ solvent-solvent interactions, molecular shape, and packing constraints.¹⁵⁹ Co-adsorption involving different solvent molecules allows for a fine-tuning of self-assembled architectures.¹⁶³ However, although many reports focus on either the solvent or the template, less is known about how the two effects work jointly in molecular crystal growth.

Here, we show that two distinct approaches to controlling crystallization, template and solvent, work together to define the observed out-of-plane fullerene packing in solution-processed fullerene films. Using a planar aromatic solvent molecule (TCB),

the monolayer porous COF-1 guide fullerene guest molecules to a template-defined close packing. Varying the solvent to an aliphatic (heptanoic acid), the fullerenes crystallize in a number of different less-dense polymorphs. Our STM images and DFT calculations collectively suggest the observed quasi-close-packed geometries are stabilized through co-adsorption of heptanoic acid.

This work demonstrates the possibility to create new polymorphs and tune molecular packing through the synergistic effect of template and solvent co-adsorption simultaneously. The combination of these two effects can effectively control molecular packing beyond the first layer, even for highly-symmetric building blocks like fullerene. The ability to arrange fullerenes into distinct packing could provide a useful approach towards improving device performance in thin-film based architectures,¹⁶⁴ such as field effect transistors⁸⁶ or photovoltaics.⁸⁷

5.2. Results and discussions

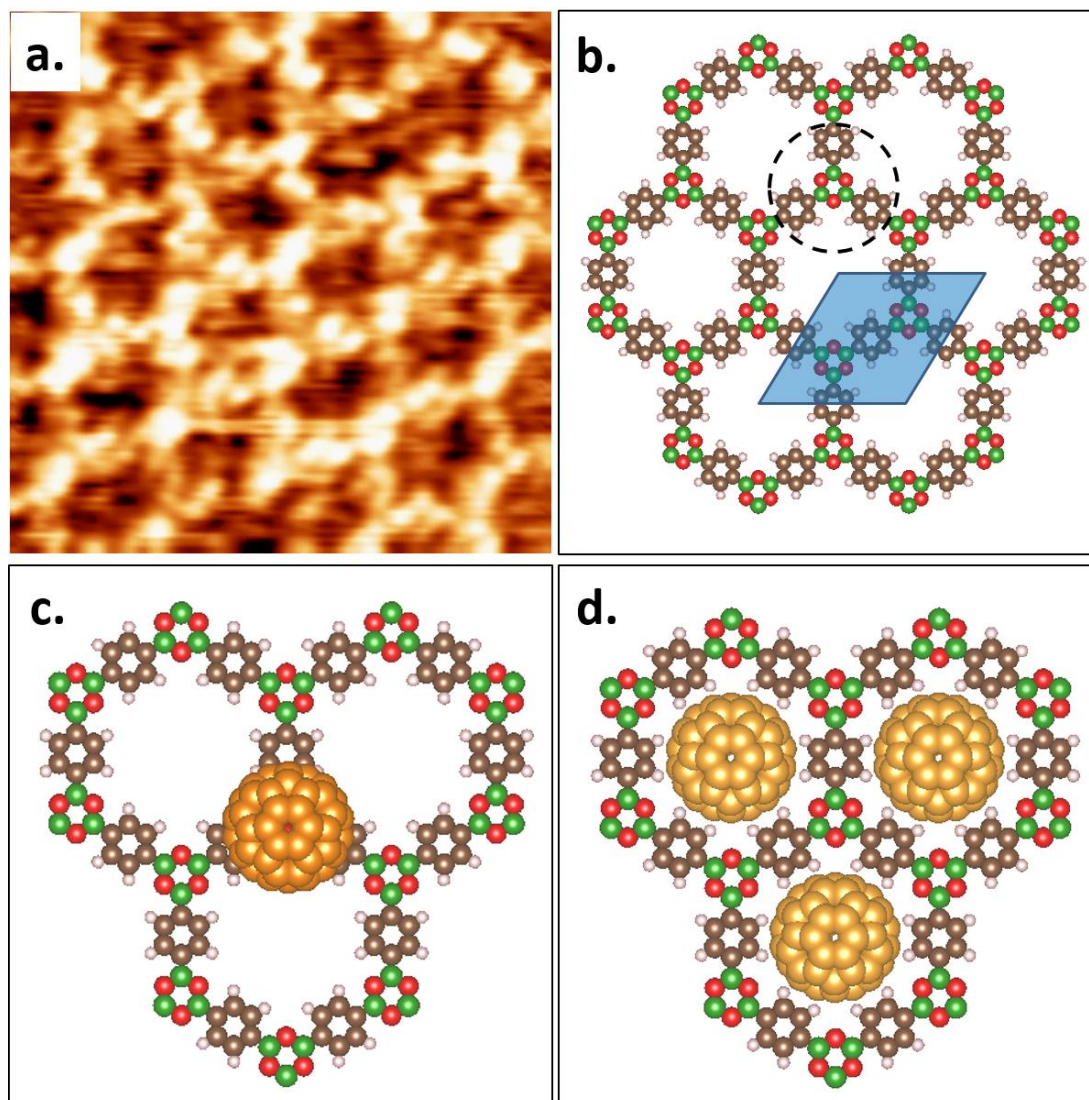


Figure 5.1 (a) Sub-molecularly resolved COF-1 template STM image collected at air/solid interface. Tunnelling conditions: $V=-800$ mV, $I=100$ pA. Image dimensions: 7.1×7.1 nm². (b) Schematic image of honeycomb COF-1 with unit cell shaded blue and a boroxine ring together with three neighbor benzenes specified with dashed black circle. DFT optimized top-site (c) and pore-site (d) positioning of a guest C₆₀ molecule

within the COF-1 host. The substrate graphene bilayer has been omitted for better visibility. Detailed simulation results are given in calculation section.

COFs are a recently discovered class of porous crystalline materials with high architectural and chemical robustness and customized topologies.²⁹ A high-quality extended hexagonal porous COF-1 template can be obtained through cyclocondensation of three BDBA monomers by using excess water as the chemical-equilibrium-manipulating agent (*Figure 5.1a* and *b*).⁴⁹⁻⁵⁰ In previous work, we demonstrated that the monolayer COF-1 mesh preferentially grows in a 6×6 epitaxial unit cell on HOPG, corresponding to a lattice parameter of 1.476 nm, and showed that C₆₀ adsorbs in the COF-1 template in two different sites, the top-site (T) and the pore-site (P).⁸⁰ T-site and P-site geometries correspond to the adsorption of the C₆₀ guest molecule on the boroxine ring and in the hexagonal pore, respectively. Corresponding DFT simulation results are presented in *Figure 5.1c, d* and *Figure 5.14*. We have previously reported an off-centred adsorption for P-site C₆₀ at the heptanoic acid/HOPG interface.⁸⁰ Our present DFT calculations suggest that C₆₀ adsorbs most stably at the centre of the pore (*Figure 5.15*). The off-centred adsorption observed experimentally could support the hypothesis of solvent coadsorption (see section 5.2.2), since moving the C₆₀ off centre allows solvent access to the HOPG substrate beneath the pore.

5.2.1. C₆₀ self-assembly at heptanoic acid/HOPG interface

5.2.1.1. Multiple-layer structures with P-site as bottom layer

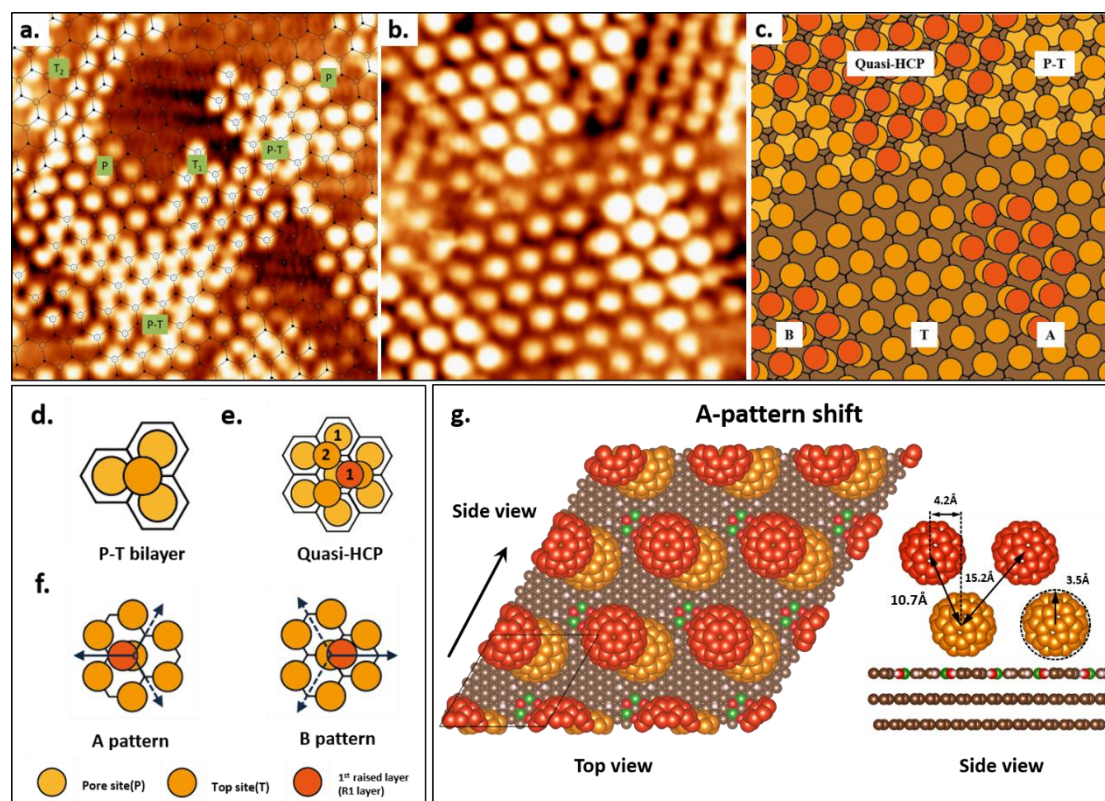


Figure 5.2 (a) STM image with P-T bilayer structure collected at the heptanoic acid/HOPG interface. Tunnelling conditions: $V=-776$ mV, $I=42.25$ pA. Image dimensions: 19×19 nm². (b) STM image collected at the heptanoic acid/HOPG interface showing quasi-HCP triple layer structure and R1_T layer shifts in A and B patterns. Tunnelling conditions: $V=-800$ mV, $I=33$ pA. Image dimensions: 15.4×15.4 nm². (c) The schematic image corresponding to (b). Different architectures are marked by indicators. (d) Model of the P-T bilayer. (e) Model of the quasi-HCP triple layer structure. The two fullerene molecules marked with “1” are adsorbed in the

quasi-same position. (f) Models of the shift of a single $R1_T$ layer molecule with respect to the T layer in A and B patterns. (g) The DFT calculated structure of A-pattern shift, as shown in top view and side view. The relative positions of T-site and R1 C_{60} are specified in side view. For a better visualization, the radius of C_{60} carbon atoms is enhanced.

Multi-layer C_{60} thin films were prepared by drop-deposition of fullerene guest molecules in heptanoic acid onto pre-prepared COF-1-covered HOPG and imaged at room temperature with STM. In previous work, the adsorbed C_{60} molecules were observed to order into domains comprising a single adsorption site.⁸⁰ Presently, we show that combination of T and P adsorption sites can also occur in the same region through the formation of a bilayer. For instance, we have observed a bilayer structure consisting of P-site C_{60} in combination with a T-site C_{60} , which we denote as a P-T bilayer (Figure 5.2a), which is consistent with the small domains reported by Plas *et al.*¹²² In Figure 5.2a, a hexagonal mesh representing the COF-1 lattice is superimposed on the STM image. Bright spots are interpreted as C_{60} molecules.

Two T-site C_{60} molecular lattices, located over boroxine rings, can be identified and represented by open circles (T_1) and spots (T_2). These lattices coexist with P-site C_{60} , defining the P-T bilayer structure (Figure 5.2d). The cohesive energy of P-T bilayer is -2.36 eV, higher than the sum (-2.12 eV) of the P-site and T-site energies (Table 5.1, DFT-D3). When both the P-site and the T-site are occupied, additional stability is gained from the interaction between the adjacent fullerene molecules. However, the

existence of P-T structure relies on the adsorption of P-site C_{60} , which can be influenced by the solvent in use.⁵⁶

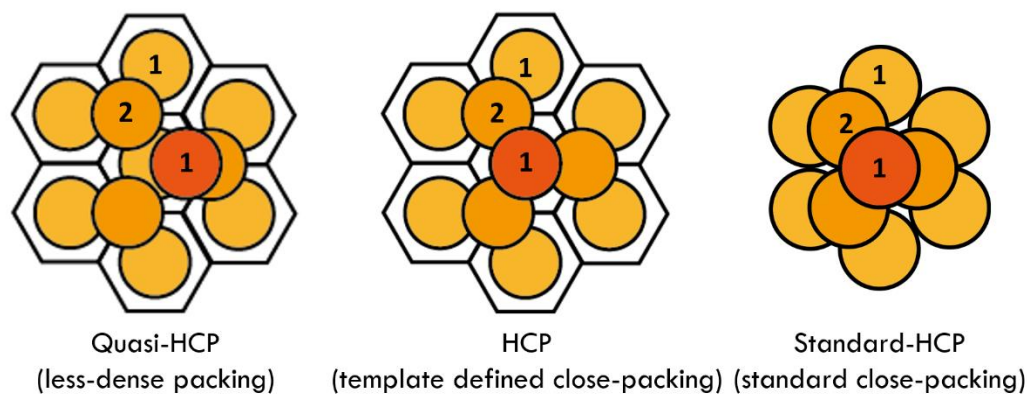


Figure 5.3 A comparison of quasi-HCP (left), HCP (middle) and standard-HCP (right). Similar arguments can also be assigned for the face-centred cubic (FCC) packing. The quasi-structure is associated with the shift behavior of R1 fullerenes (marked 1 in the orange circle) with respect to the given T-layer fullerene (marked 2). Note that, in the quasi-HCP and HCP here, the intralayer C_{60} molecules are spaced with a distance of 1.476 nm. This is different from standard-HCP, where all the molecules are spaced in a distance of ~ 1 nm.¹⁶⁵ The standard-FCC close packing C_{60} can be formed on bare HOPG, see Figure 5.10.

The COF-1 template can host a variety of multilayer structures. A third layer, named as the first raised layer ($R1_{P-T}$), can adsorb above the P-T bilayer to form a triple-layer structure (STM image in Figure 5.2b and schematic in Figure 5.2e). As shown in the schematic view, this triple layer presents a quasi-hexagonal close-packed (quasi-HCP) structure. We define this as a “quasi”-HCP structure because of the shift between the

first and third layers (see *Figure 5.3*), which differs from the HCP in which the first and third layer molecules are positioned in registry with one another.

5.2.1.2. Bilayer structures with T-site as bottom layer

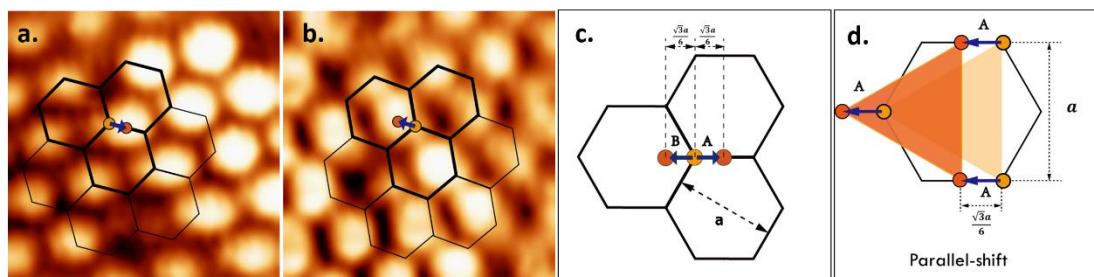


Figure 5.4 STM images of a single R1 fullerene shift collected at heptanoic acid/solid interface, where the COF-1 lattice is represented by the black honeycomb, and the yellow and orange circles indicate T layer and R1 layer fullerene molecules respectively. (a) A-pattern shift. (b) B-pattern shift. (c) Geometry of the shifts, where the epitaxial COF-1 lattice constant is $a=1.476$ nm according to our previous work. (d) The collective assembly of R1 fullerenes, parallel-shift. Tunnelling conditions: $V=-800$ mV, $I=33$ pA. Image dimensions: 6.5×6.5 nm².

A monolayer of T-layer, with no corresponding molecules in the P-site, can also form the foundation for further adsorption. In this case, the R1_T layer can shift in two distinct geometries with respect to the T-layer. We denote them as A-pattern shift and B-pattern shift, each of which exists in three-fold symmetry with respect to a given T-site fullerene, as shown in *Figure 5.2f*. Our calculations support this observation and show that A- and B- shift are stable structures with the binding energy of the R1_T fullerene calculated as $E_A=-0.21$ eV and $E_B=-0.25$ eV respectively (*Figure 5.16* and

Table 5.1). The DFT optimized structure of the A-pattern shift is presented in *Figure 5.2g*. When full domains of R1_T fullerenes linearly shift in the same direction (A- or B- pattern), we denote this collective assembly as a parallel-shift (see *Figure 5.4d*). The R1_{P-T} layer also has the same geometry (*Figure 5.2b* and *c*). Through a combination of distances measured from STM images and geometrical considerations, we find that the shift distance of the R1 layer relative to the given T-layer fullerene is 0.43 nm, which is the half-length of the hexagonal edge, as shown in *Figure 5.4*. This is consistent with our calculation result (0.42 nm). However, the observation of shift structures runs counter to Kitaigorodskii's close-packing principles,¹⁶⁶ since the R1 layer adsorption site is not the three-fold centre described by the T-layer C₆₀, which is the enthalpically favoured template-defined close-packed structure, with a binding energy of -0.73 eV (A-close packing, see *Figure 5.16* and Table 5.1). We attribute the observed shift trapped R1 C₆₀ motif to the effect of co-adsorption of solvent molecules associated with the growth process, explained hereafter.

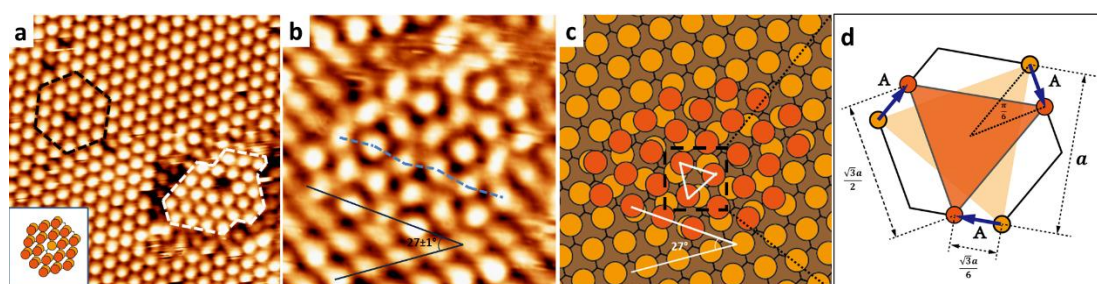


Figure 5.5 (a) STM image collected at the heptanoic acid/HOPG interface. The black dashed line encloses a region of the crystal with one missing C₆₀ molecule. The inset image shows the plan view schematic of the black dashed box region, according to the parallel shift model. The white dashed line marks a rotated-shift region. Tunnelling

conditions: $V=-800$ mV, $I=100$ pA. Image dimensions: 24.4×24.4 nm². **(b)** Detailed STM image collected at heptanoic acid/HOPG interface showing a moiré pattern caused by rotation of the R1 layer relative to the underlying T layer. Tunnelling conditions: $V=-800$ mV, $I=100$ pA. Image dimensions: 11.8×11.8 nm². **(c)** The schematic image corresponding to (b). Orange circles represent the R1 layer molecules and yellow circles represent the T layer molecules. **(d)** The schematic image of geometrical considerations of the region (spin centre) enclosed by the dashed box in image (c), showing the geometry of the rotation of the R1 layer relative to the T layer.

Figure 5.5a shows a film where the R1 layer exhibits predominantly a parallel shift. However, another collective adsorption geometry is also possible: the R1 layer can be rotated relative to the T-layer, forming a domain with a flower-like appearance (moiré pattern, Figure 5.5b), referred to as a rotated-shift alignment (see Figure 5.5d). The R1 lattice and T-layer lattice are rotated by $27\pm 1^\circ$ with respect to one another and the schematic is given in Figure 5.5c. The rotation can be interpreted according to the three-fold symmetry of the-shift behavior of an R1 fullerene (Figure 5.2f). Surrounding the rotation centre, three R1 fullerenes move clockwise by a distance of half-length of a hexagonal edge, leading to a 30° rotation of the R1 lattice with respect to the T layer (Figure 5.5d). The effect of stacking the rotated-shift R1 layer and T-site layer gives rise to a flower-like appearance in STM images, which can be attributed to the influence of the moiré pattern superlattice on the electronic properties probed by STM.¹⁶⁷

In the scheme shown in *Figure 5.5d*, the R1 layer is rotated by an angle of 30° and has a different lattice constant ($\sqrt{3}a/2 = 1.278$ nm) from the T layer ($a=1.476$ nm). However in the STM image of *Figure 5.5b*, the R1 lattice is rotated by $27\pm 1^\circ$ with respect to the T-layer lattice. This likely occurs because, in a large domain size, a slight relaxation in the R1 lattice will be preferred energetically, with a rotated angle of 27° between R1 and T layers and R1 lattice constant matched to that of the T layer. Nevertheless, the rotated-shift can still introduce strain in localized regions, unlike the fully relaxed parallel-shift. R1 fullerenes exhibit a preference for adsorbing at binding sites described by the T layer, *i.e.*, the parallel shift sites. The fullerenes in the rotated-shift R1 layer are also constrained by the rotated R1 lattice. The rotated shift lattice does not perfectly match the parallel shift lattice. The local trade-off between the preference for binding sites on the T layer and the constraint of the rotated R1 lattice results in a positioning offset of the C_{60} molecules from one another along the R1 high-symmetry directions, creating a zigzag appearance (see blue dashed line in *Figure 5.5b*). Compared with the parallel-shift, the strain introduced by rotated-alignment seems to make this architecture energetically less favorable, consistent with *Figure 5.5a* where parallel-shift is dominant. Typically, the area of a rotated-shift domain is less than one unit cell of the superlattice of the moiré pattern, as shown in *Figure 5.6*.

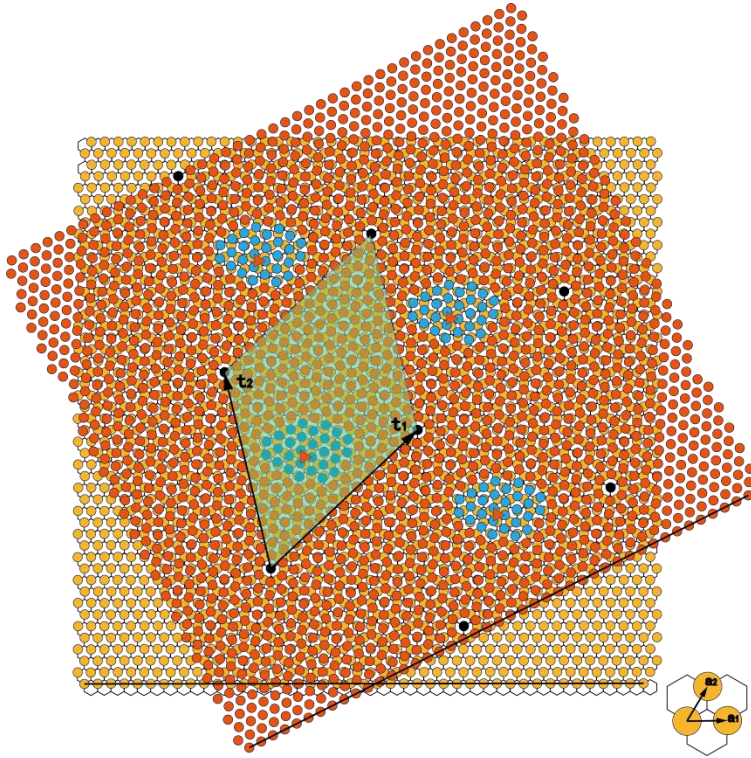


Figure 5.6 Moiré pattern of R1 layer rotated by $\theta = 26.746^\circ$ (indicated by lines at the bottom) with respect to the underlying T layer. The vectors of the Moiré pattern t_1, t_2 are shown by arrows and labeled accordingly. The lattice vectors a_1, a_2 of the underlying T monolayer are sketched at the lower right, where a magnification by a factor 3 is applied for better visibility. Specifically, the region of Figure 5.5b is marked by colour of blue in a unit cell, where the centre of spin defined in Figure 5.5c is marked with orange triangle. The calculated model is available in experimental section.

5.2.1.3. Tri-layer structures with T-site as bottom layer

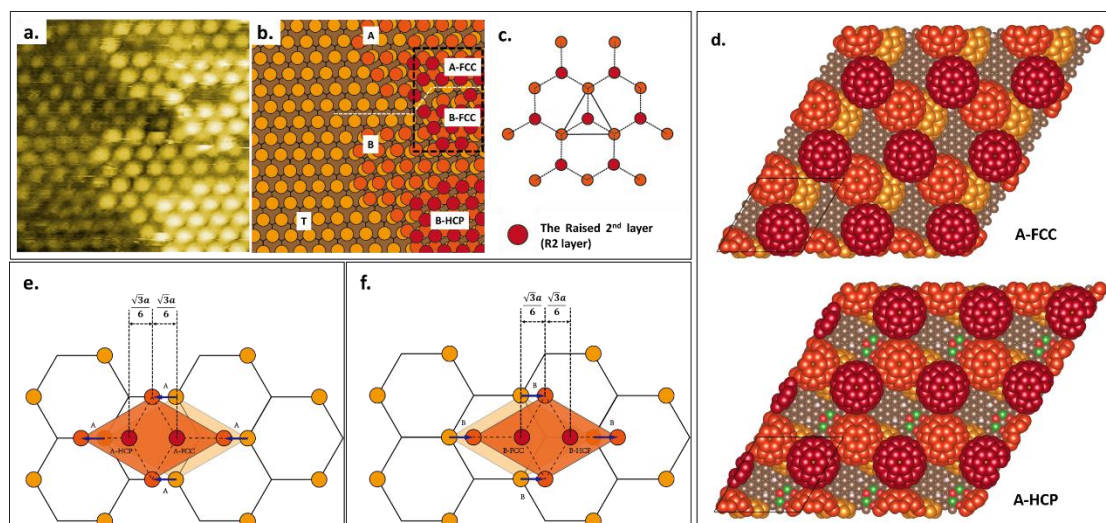


Figure 5.7 (a) STM image collected at heptanoic acid/HOPG interface showing multiple crystallization geometries for three layer structures. Tunnelling conditions: $V=-800$ mV, $I=200$ pA. Image dimensions: 17.3×17.3 nm². (b) The schematic of (a). (c) The schematic showing position of the R2 layer relative to the R1 layer. (d) The DFT optimized geometries of A-FCC and A-HCP. Schematic showing the positions of C₆₀ in the T layer (bottom), R1 layer (middle) and R2 layer (top) relative to each other for an R1 layer with A-pattern shift (e) and B-pattern shift (f).

For the case where the R1 shift is parallel, we observed another layer superimposed on top of the R1 layer, denoted as the raised second layer R2, which together with the R1 and T layers forms a triple-layer structure, as shown in *Figure 5.7a*. In this architecture, the R2 fullerenes adsorb in the three-fold hollow site formed by R1 fullerenes, creating the close packed structure (*Figure 5.7c*).

C₆₀ molecules of R1 and R2 do not occupy the exact positions defined in a

template-defined close-packed model due to the shift in the R1 layer. Using the COF-1 host template and T-layer as a reference, the parallel-shift of R1 will give two possible positions for molecules in the R2 layer. In *Figure 5.7e*, a parallel-shift in A pattern positions an R2 layer C₆₀ nearly above a T-layer C₆₀, defining a structure that we denote as A-HCP, and another occupied position nearly above an empty site in the T-layer, defining the A-FCC structure. A similar nomenclature can be assigned for the B pattern shift, shown in *Figure 5.7f*. R2 molecules in A-FCC and B-FCC occupy the same position with respect to the reference (T-site/COF-1) layer, although the structures themselves are non-identical due to the geometry of the R1 layer. In *Figure 5.7b*, The A pattern shift and B pattern shift are separated by a white dashed line, and the black dashed box shows the alignment of A-FCC and B-FCC. Our calculations suggest that each fullerene in R2 has an adsorption energy of ~-0.6 eV (Table 5.1) and the corresponding optimized geometries are given in *Figure 5.7d* and *Figure 5.17*.

5.2.2. Identification of the solvent co-adsorption effect

The structural analysis above suggests that R1 C₆₀ molecules, which adsorb in the less-dense shift motifs instead of template-defined close-packing, lead to the formation of this diverse array of polymorphic structures. Using heptanoic acid as solvent, we never observed the R1 template-defined close-packed structure (the three-fold hollow site described by T layer), despite the thermodynamic advantage it offers.

There are two primary effects that help to favour the shifting in R1 layer C_{60} , rather than to close-packing: electrostatics¹⁶⁸ or a solvent effect.³⁵ To explore the electrostatic effects, we performed Bader charge analysis of the DFT simulated structures. These calculations show that the charge transferred between the T-site and the shift R1 C_{60} is negligible and that the charge distribution of the R1 shift C_{60} is essentially the same as that of a free C_{60} (See Table 5.2). This is consistent with our calculated energies for the binding between the shift R1 C_{60} and the corresponding T-site fullerene, which are essentially identical whether the fullerene dimer is calculated in the presence or absence of the COF-1/graphene bilayer substrate (~ 0.2 eV, see Table 5.1). These results indicate that the shift R1 C_{60} molecules are stabilized through vdW interactions with the underlying T-site fullerene, ruling out the anisotropic electrostatic effects potentially caused by the presence of the substrate.^{75,}

169-170

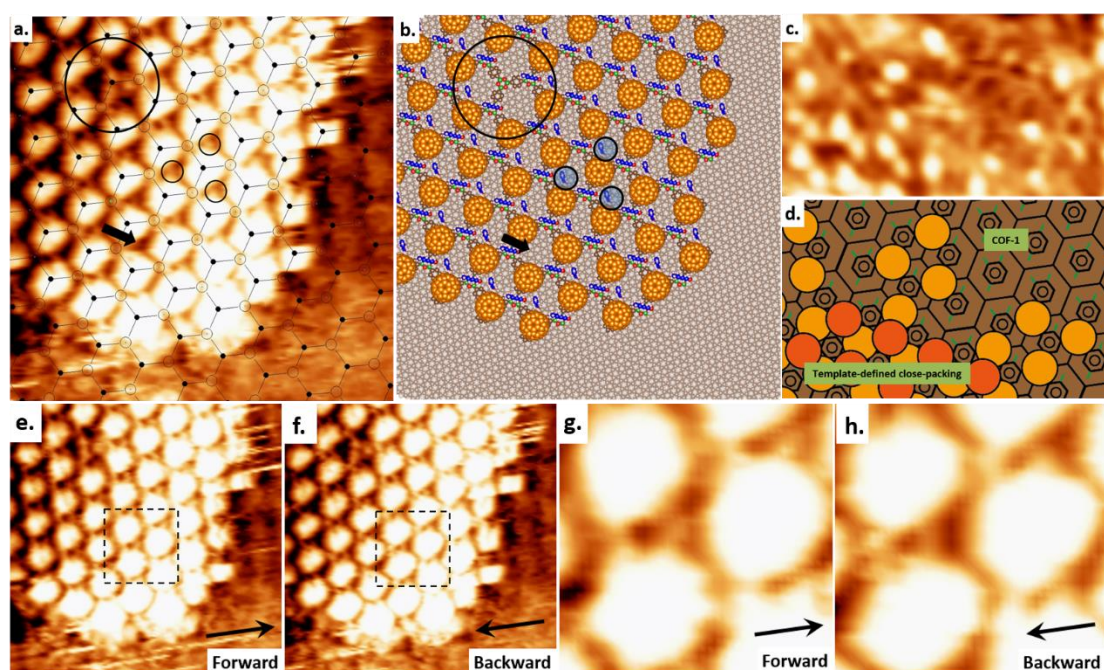


Figure 5.8 (a) STM image showing the co-adsorption of heptanoic acid and T-layer C_{60} collected at the heptanoic acid/HOPG interface. Tunnelling conditions: $V=-1000$ mV, $I=50$ pA. Image dimensions: 12×12 nm². The hexagonal lattice represents the COF-1 template. A single missing C_{60} is marked by a large black open circle. The features at the bottom of missing C_{60} site are assigned as COF-1 template. Three small bright spots assigned as solvent molecules are marked by small black open circles; similar adsorption occurs throughout the lattice, but has not been indicated to allow clearer visualization of the contrast modulation associated with these features. One site without this small bright feature is marked by a black arrow. **(b)** Optimized structure of T-layer C_{60} with co-adsorption of heptanoic acid at both P-site and T-site (See section 5.5). The T-site heptanoic acid molecules appear at each of the three boroxine rings in the COF-1 template. Only one P-site adsorbed heptanoic acid appears per pore, consistent with the slightly off-centre adsorption of the T-site C_{60} molecule. For a better illustration of the model matching with the experimental data, scheme (b) has been modified from the actual DFT data by taking off the features missing from the STM image (a). **(c)** STM image collected at the supernatant (TCB)/HOPG interface. Image dimensions: 9.6×5.4 nm². Tunnelling conditions: $V=-1000$ mV, $I=50$ pA. Here, R1 C_{60} adsorbs in a template-defined close-packed geometry. **(d)** Schematic of (c) with TCB molecules in the pores of the COF-1 template. The STM images (e and f) showing the co-adsorption of heptanoic acid in T-layer C_{60} obtained in a same collection. **(e)** is the forward-scan image and **(f)** is the backward-scan image. Tunnelling conditions:

$V=-1000$ mV, $I=50$ pA. Image dimensions: 11.72×11.72 nm². (**g**, **h**) are magnified images corresponding to the regions marked by dashed black squares in (e) and (f) respectively. Image dimensions: 2.8×2.8 nm². The black arrows in the images indicate the direction of scan. (f) is also shown in (a).

In *Figure 5.8a*, some smaller bright spots are visible within the T layer. The size of these features (~ 0.39 nm) is consistent with previous observations of upright heptanoic acid (~ 0.35 nm),¹⁷¹ suggesting the possibility of co-adsorption of solvent molecules in the interstitial spaces. The position of a small bright feature within one pore is also influenced by the scanning direction of the STM. In the forward scan, the small bright spot locates in the center described by three T-site C₆₀ molecules (*Figure 5.8g*). But in the backward scan, the small bright spot locates asymmetrically into one of the three equivalent corners (*Figure 5.8h*). The positional site of this small bright spot is associated with the direction of scan. This observation supports our hypothesis that these small bright features are up-oriented heptanoic acid molecules and the flexibility of the heptanoic acid molecule offers the explanation for the different placement of bright spot feature associated with STM scan direction.

Hence, we propose that the formation of shifted R1 C₆₀ can be attributed to the co-adsorption of heptanoic acid in the void spaces between C₆₀ molecules in the T layer (Table 5.4 and *Figure 5.8b*).³⁵ Heptanoic acid molecules are known to orient with their carboxyl groups pointed towards the surface and their alkyl chains pointing out of the surface (Table 5.3 and *Figure 5.18*); the chains are likely to be

disordered.¹⁷¹ Heptanoic acid molecules can also orient with their carboxyl groups upward, forming a dimer with another solvent molecule.¹⁷² Since the length of heptanoic acid (~1.0 nm for monomer and 2.1 nm for dimer) is comparable with (bigger than) the diameter of C₆₀, the protruding alkyl chains would prevent the R1 C₆₀ from adsorbing in a template-defined close-packed motif (*Figure 5.19*). In STM images, the arrangement of coadsorbed alkylated solvent molecules typically cannot be clearly resolved in 2D,^{159-160, 173} much less in our case of co-adsorption in 3D space. Thus, no conclusion can be drawn about the precise adsorption arrangement or conformation of the solvent molecules in the gaps between C₆₀ molecules. However, even in the absence of a detailed understanding of the adsorption geometry, DFT calculations in which heptanoic acid molecules have been added to the unit cells of shift-structure architectures suggest that the presence of the incorporated solvent molecules stabilizes the shift structures (Table 5.4).

5.2.2.1. Control experiment: C₆₀ self-assembly at TCB/HOPG interface

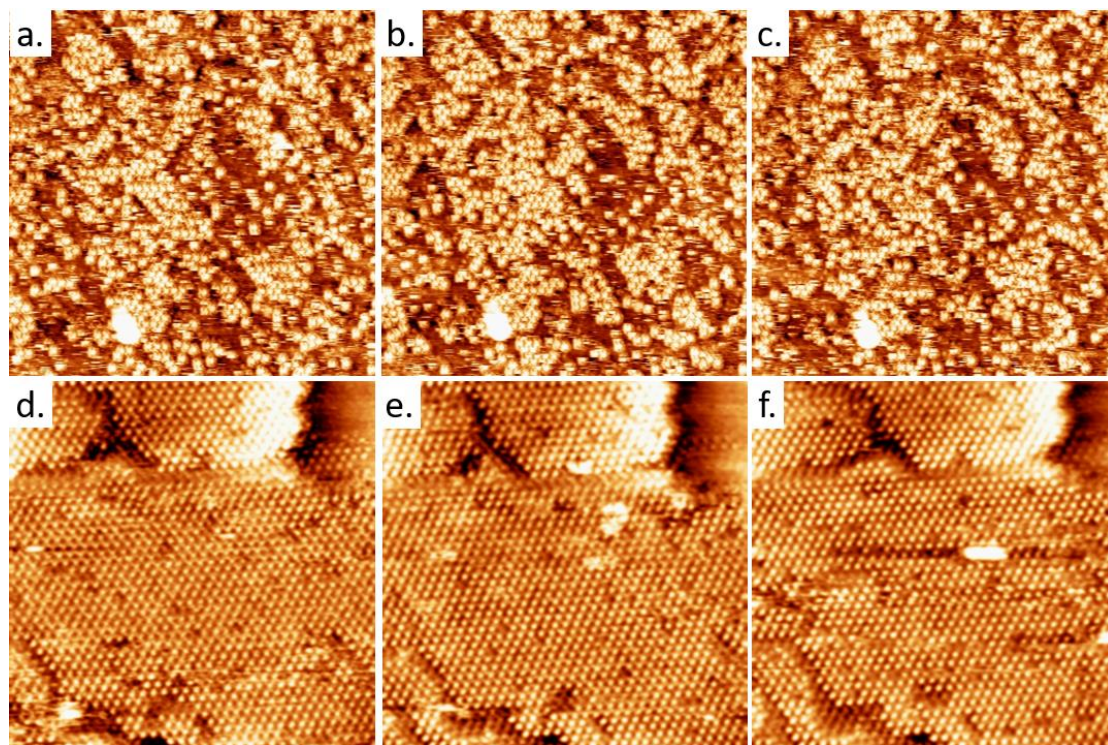


Figure 5.9 (a-c) Successive STM images of same region collected from the TCB supernatant/HOPG interface. Image dimensions: $80 \times 80 \text{ nm}^2$. Tunnelling conditions: $V = -1200 \text{ mV}$, $I = 50 \text{ pA}$. (d-f) Successive STM images of same region collected from the heptanoic acid supernatant/HOPG interface. Image dimensions: $60 \times 60 \text{ nm}^2$. Tunnelling conditions: $V = -800 \text{ mV}$, $I = 100 \text{ pA}$. The domain morphology of the C₆₀ films in TCB varies with time, in contrast to the films formed from heptanoic acid. In the latter (d-f), individual vacancies vary from image to image, but the overall domain structure and occupancy remains relatively constant.

To test the solvent coadsorption hypothesis, we performed the same experiment using

a different solvent. Instead of heptanoic acid, we applied the supernatant of C_{60} in TCB, a planar aromatic solvent without alkyl chains, to a pre-fabricated COF-1 monolayer. Based on our previous work, we expect the TCB to adsorb flat in the COF-1 pores.⁵⁶ Using TCB as solvent, we obtained the enthalpically-favored template-defined close-packed motif of R1 C_{60} , as shown in *Figure 5.8c*. The Moiré pattern formed by rotated-shift was not observed, indicating the absence of the R1 shift structure. Moreover, the C_{60} film in TCB is less stable under STM scanning than C_{60} films in heptanoic acid, as shown in *Figure 5.9*. Based on the energetics of the fullerenes alone, this observation is counterintuitive, since the template-defined close-packed R1 C_{60} is more stable than shift R1 C_{60} (*Figure 5.16*). However, taking into account the coadsorption of solvent molecules, this observation is consistent with the increased stability of the fullerene layer due to interactions with standing heptanoic acid molecules (Table 5.4 and *Figure 5.19*). The planar, pore-confined TCB cannot interact with raised layers and therefore offers no stabilization.

5.2.2.2. Solvent co-adsorption leading to polymorphism

We suggest that the co-adsorption of solvent molecules is responsible for the observed polymorphism: co-adsorbed heptanoic acid sterically inhibits the formation of the close-packed fullerene structure, which is instead allowed by the smaller planar TCB solvent molecules. Without the COF-1 template, C_{60} molecules crystallize into a standard-FCC C_{60} close packed crystal on HOPG, rather than forming

pseudopolymorphic phases incorporating heptanoic acid (See *Figure 5.10*).^{165, 174-175}

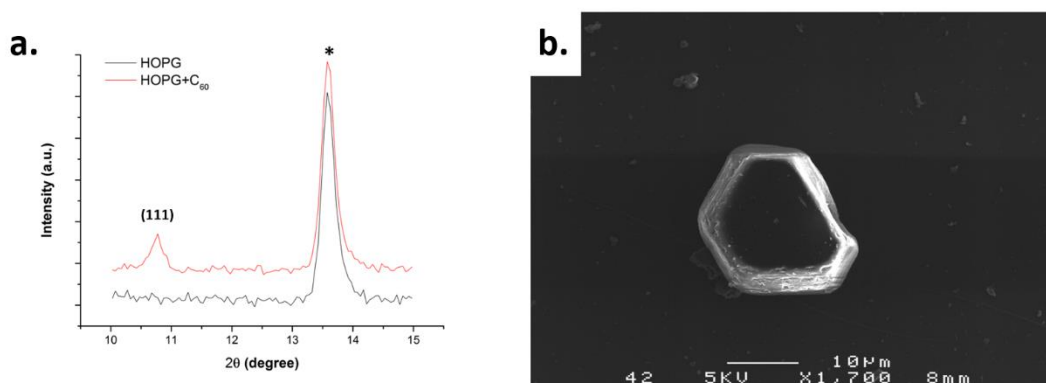


Figure 5.10 (a) XRD spectra of bare HOPG (black) and C_{60} crystal on HOPG (red).

The peak at $2\theta = 10.8^\circ$ ($d \sim 0.82$ nm) corresponds to the (111) face of standard-FCC fullerene ($a = 1.42$ nm). This is also consistent with (002) of standard-HCP fullerene with $a = 1.00$ nm and $c = 1.64$ nm, but in this case we should also observe the weaker (001) reflection at 10.2° . The asterisk indicates the peak from HOPG.¹⁷⁴ (b) Scanning electron microscopy image of an asymmetric C_{60} hexagonal-shaped disk on bare HOPG, prepared by drop-deposition method with a solution (1.942×10^{-3} M) of C_{60} in heptanoic acid.

In *Figure 5.10*, x-ray diffraction (XRD) data and scanning electron microscopy (SEM) image for the solution processed bulk C_{60} crystals are shown. These results are consistent with Hyeon Suk's work,¹⁷⁴ where standard close packed bulk C_{60} crystals were prepared through vapor-solid process. This suggests that heptanoic acid solvent molecules don't influence the standard close packing structures: the motif structure of C_{60} crystals in solution-deposition is just like what they exhibit when in vapor-deposition.

However, there may be important differences between bulk and thin film C_{60} . A necessary comparison between C_{60} film on bare HOPG and our present work (with COF-1 template) is desired.

C_{60} weakly interact with HOPG substrate through vdW interactions.^{165, 176} There have been numerous experimental studies about the growth of C_{60} on HOPG in UHV.¹⁷⁷⁻¹⁸¹ Although different experimental conditions can affect the morphologies of C_{60} film,¹⁸² the motif structure of C_{60} film has been confirmed to consist of a standard close-packed arrangement of C_{60} molecules on HOPG by both STM^{175, 179, 183} and low-energy electron diffraction.^{181, 184} The standard close-packing films in these references suggest HOPG substrate plays a relatively minimal role in the arrangement of C_{60} molecules, unlike COF-1 covered HOPG where the lattice constant of C_{60} packing can be modified by template network.

To investigate the effect on C_{60} packing motif when solvent is present on HOPG surface, we performed STM characterization at the supernatant solution (C_{60} in heptanoic acid and TCB)/bare HOPG interface.⁸⁰ In contrast to UHV condition, we did not observe the self-assembly of C_{60} on HOPG. This can be explained by the affinity between C_{60} and solvent molecules and that C_{60} molecules experience fast adsorption and desorption between solution species and adsorption on the HOPG surface, so that STM cannot observe any stable self-assembled feature of C_{60} . This also suggests that solvent (heptanoic acid and TCB) and C_{60} alone cannot form pseudopolymorph at the solution/HOPG surface. This suggests that the co-adsorption

of solvent molecules in the C₆₀ film is driven by the template. Solvent co-adsorption can occur because the template-induced packing creates solvent-sized void spaces between C₆₀ molecules. This is different from previous investigations, where polymorphism was driven by solvent co-adsorption through stronger solute-solvent interactions, such as hydrogen bonds, or through solvent-surface interactions.^{35, 133, 145,}

159, 161

To summarize, C₆₀ molecules have been previously observed to pack in a standard close packing structure on HOPG surface. This occurs in both film and bulk C₆₀ under vacuum deposition conditions, for bulk C₆₀ when solution-processed (heptanoic acid). However, at the solution/HOPG interface, we were unable to observe self-assembly of C₆₀, and no reports of this. Conversely, in the presence of COF-1 at the TCB/HOPG interface, a template-defined close packed structure was obtained and at the heptanoic acid/HOPG interface, a less dense packing structure was obtained, which we assigned as a template-driven solvent co-adsorption effect. These discussions are schematically shown in *Figure 5.11*.

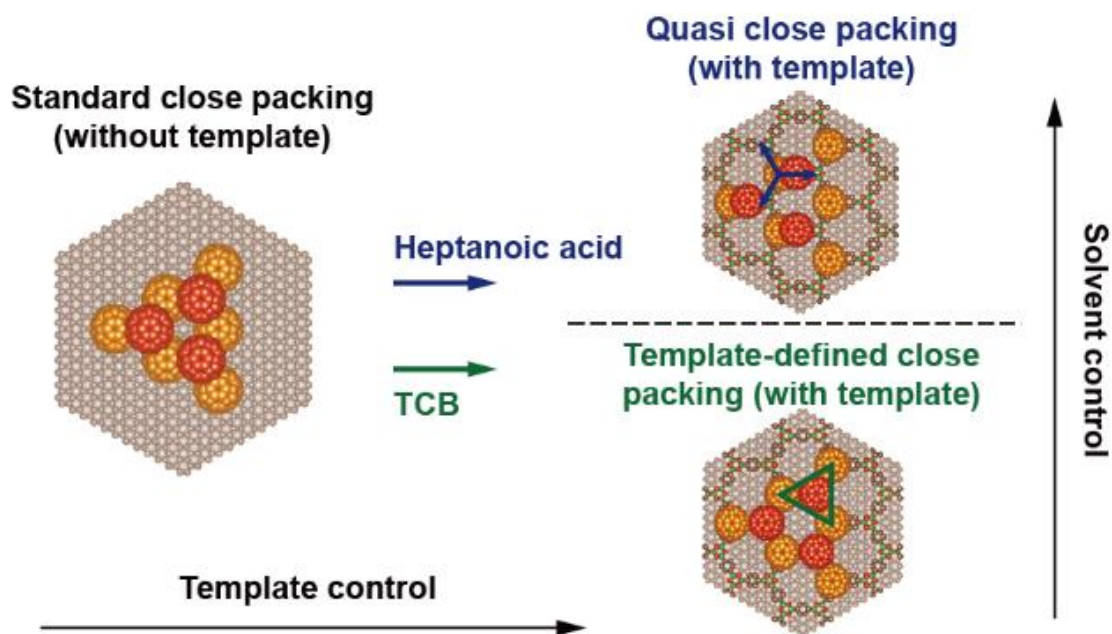


Figure 5.11 Schematically illustration of the control of fullerene crystallization from 2D to 3D through combined solvent and template effects.

5.2.3. Additional solvent effects on film packing and morphology

Thermodynamics. Besides the co-adsorption effect, the properties of solvents, such as polarity and solvophobic effect, can also influence the self-assembled structures through an environmental change for the C_{60} molecules. Although the dielectric constants of heptanoic acid (3.04) and TCB (2.24) are different, we do not expect this to affect fullerene assembly, since solvent polarity mainly influences molecular self-assembly stabilized through hydrogen bonding or dipole–dipole interaction by changing the microenvironment of adsorbates.^{35, 37-38, 159} Solvophobic effects may also play a role in this case since we have polar solvent and non-polar solute. A non-polar solute has a stronger propensity to form a close-packed structure in more polar

solvents, to reduce the interface between them.³⁵ However, here the close-packed structure is obtained in a less polar solvent, which does not follow this trend, and precludes solvophobicity as a contributing effect.

Kinetic effects on the packing motif. Kinetic effects are also known to lead to polymorphism.^{16, 162} It is reasonable to assume that the R1 shift structure is kinetically favored with respect to the template-defined close-packed structure. According to Ostwald's law of stages,¹⁸⁵ if several states exist, the state initially adopted will not be the most stable, but will instead be the state nearest to the original state in free energy. A rapid adsorption rate (*i.e.*, the number of molecules adsorbing from the liquid onto the surface per unit of area and time) of C₆₀ may lead to the shift adsorption R1 C₆₀, because the system is trapped in a higher-energy state.¹⁶² However, the TCB supernatant, which contains a higher concentration of C₆₀ than heptanoic acid,¹⁸⁶ should produce a faster adsorption rate than a heptanoic acid solution, and could therefore be expected to give rise to shifted adsorption, which runs counter to our experimental observation of the R1 template-defined close packed structure. Therefore, the adsorption-rate related kinetic trapping of the polymorph can also be ruled out.

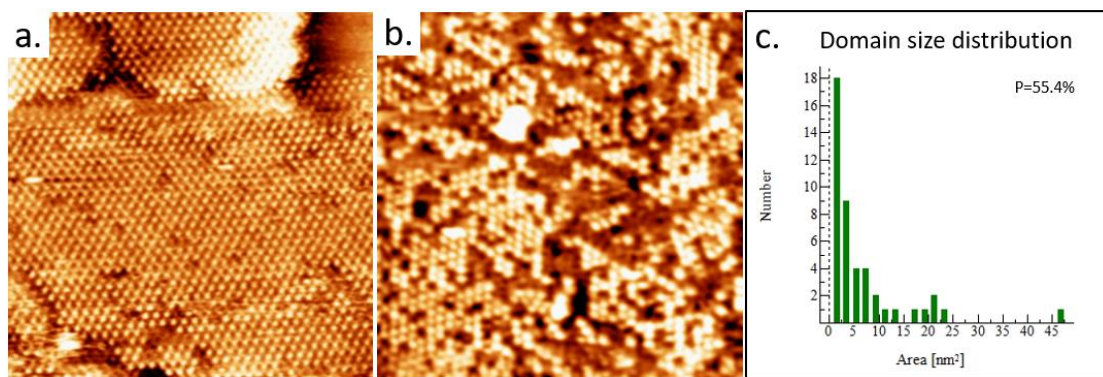


Figure 5.12 STM images collected from supernatant solutions of C₆₀. (a) STM image at the heptanoic acid supernatant/HOPG interface. Tunnelling conditions: $V=-1200$ mV, $I=50$ pA. Image dimensions: 60×60 nm². (b) STM image at the TCB supernatant/HOPG interface. Tunnelling conditions: $I=100$ pA, $V=-800$ mV. Image dimensions: 60×60 nm². (c) Domain size distribution of (b). The coverage (P) of C₆₀ in STM image is 55.4%.

Kinetic effects on the morphologies of C₆₀ films. Although kinetic effects do not account for the observed polymorphism, they have a discernible effect on the morphology of the film. From the heptanoic acid supernatant, C₆₀ molecules have a tendency to form large domains on the COF-1 template, with domain boundaries occurring as a consequence of the domain structure of the COF-1 monolayer (Figure 5.12a and Figure 5.9).¹²² However, C₆₀ molecules adsorbed from the TCB supernatant are confined in small clusters (see Figure 5.12b and Figure 5.9). A simple size distribution analysis of C₆₀ domains in Figure 5.12b indicates an exponential decay relationship between the number of domains and their sizes, as shown in Figure 5.12c, suggesting that the growth from TCB supernatant is consistent with a percolation

growth model.¹⁸⁷ Anecdotally, STM images with low coverage of C₆₀ on COF-1 were much more frequently obtained in TCB than that in heptanoic acid. This may suggest a lower growth rate, R_G, in the TCB system. We can treat the attachment of one C₆₀ to a pre-existing nucleate as a monomolecular process. Following first-order chemical kinetics, R_G is proportional to $[\exp(\Delta\mu/k_B T) - 1]$,¹⁸⁸ where $\Delta\mu = \mu_{\text{solution}} - \mu_{\text{crystal}}$ is the difference in chemical potential of the crystallizing species, k_B is the Boltzmann constant, and T is the absolute temperature. Since we used supernatant C₆₀ in both heptanoic acid and TCB, the solution is equilibrated with the precipitation of C₆₀, and $\mu_{\text{heptanoic acid-solution}}$ can be assumed to be roughly equal to $\mu_{\text{TCB-solution}}$ during the growth process. Under this assumption, the higher rate of growth, R_G(heptanoic acid), can be ascribed to the lower $\mu_{\text{heptanoic acid-crystal}}$. This is consistent with our expectation and observation stated above, *i.e.*, the co-adsorption of heptanoic acid stabilizes C₆₀ crystallization.

This morphological observation is similar to the competitive adsorption of two different analytes from binary mixture solutions,¹⁸⁹ and the same argument can be applied here. The different sizes of the domains suggest significant differences in the nucleation rate and growth rate of each morphology. The analytical model can be defined as a ratio $r = R_G/R_N$ with the growth rate, R_G, and nucleation rate, R_N. A large ratio r gives rise to the formation of well-ordered domains extending over large areas, as observed for heptanoic acid. On the contrary, a small ratio r means that domains nucleate quickly yet grow slowly, yielding numerous small domains; this is consistent

with the morphology of COF-templated C₆₀ in TCB. As we described above, the higher solubility of C₆₀ in TCB suggests the relation: $R_N(\text{TCB}) > R_N(\text{heptanoic acid})$. In addition, the co-adsorption with different solvent molecules gives the relation: $R_G(\text{heptanoic acid}) > R_G(\text{TCB})$. Together these indicate that $r(\text{heptanoic acid}) > r(\text{TCB})$, which is consistent with our morphological observations.

5.3. Conclusions and perspectives

Monolayer COF-1 films can induce the self-assembly of fullerene into multiple layer structures at the solution/solid interface. The template-defined packing, which deviates from standard close packing, depends on the solvent for the fullerene molecules: a template-defined close-packing motif is achieved using TCB as solvent, whereas lower-density quasi-close-packed polymorphs are observed when using heptanoic acid as solvent. The solvent-dependent polymorphism and morphologies can be described in terms of a template-driven solvent co-adsorption effect. The results presented here highlight the important role of the solvent, not just in influencing 2D self-assembly, but also in defining 3D architectures. Through a judicious combination of solvent and template, (pseudo)polymorphic films can be formed with packing geometries that have not been observed under other conditions. This suggests a pathway towards using the combination of 2D template and solvent effects to control molecular self-assembly precisely into the third dimension, even in the absence of directional solute-solute or solute-solvent interactions.

5.4. Experimental methods

Synthesis of BDBA COFs: Monolayer COF-1 on HOPG was formed following procedures described previously.⁴⁹⁻⁵⁰ 1.0 mg and 1.4 mg of 1,4-benzenediboronic acid (BDBA, Tokyo Chemical Industry Co. Ltd) was added to 1.5 ml heptanoic acid (99%, Sigma- Aldrich)⁸⁰ and 1.2 ml 1,2,4-trichlorobezene (TCB, 99%, Sigma- Aldrich),⁵⁶ respectively. This step was followed by sonication for ~30 min which produced whitish suspensions. 10 μ l of BDBA suspension was dropped onto freshly cleaved HOPG (Structure Probe International, grade SPI-1 or SPI-2) and placed into a reactor with a volume of ~16 ml. 130 μ l of deionized water was added to the bottom of the reactor, and a valve to atmosphere was left slightly open to maintain an open system. The entire reactor was placed in an oven preheated to 125 °C and left for 60 min. After thermal treatment, the reactor was taken out of the oven and allowed to cool down for at least 20 min before the samples were removed.

H/G synthesis: Following the confirmation of monolayer COF-1 on the HOPG surface, 10 μ l of a known concentration solution of fullerene (99.5%, Sigma-Aldrich) in heptanoic acid or TCB was applied onto the substrates prepared with precursors in heptanoic acid or TCB. Subsequently, the samples were characterized by STM at the solution/solid interface.

STM measurements: STM was performed at room temperature at the liquid/solid interface, using a Digital Instruments STM equipped with a Nanoscope IIIa controller. Tips were cut from a Pt_{0.8}Ir_{0.2} wire (Nanoscience Instruments). Bias voltages are

reported with respect to the STM tip. STM images were calibrated with COF-1 lattice parameter (1.476 nm) using the free WSxM software.¹¹⁹ Images were smoothed using Gwyddion software.¹⁹⁰

Characterization of C₆₀ crystal on bare HOPG: The morphology and crystal structure were characterized with a scanning electron microscopy (JEOL JSM-6300F) and an X-ray diffractometer (Panalytical X'Pert Pro MRD, using Cu K_α radiation).

Model for the Moiré pattern: The continuum model of the commensurate Moiré pattern from a twisted hexagonal bilayer is summarized as follows:¹⁹¹

The lattice of guest molecules in the bottom monolayer has an underlying Bravais lattice with basis vectors which we choose as \mathbf{a}_1 and \mathbf{a}_2 .

The Bravais lattice is expressed as:

$$\mathbf{r}(m, n) = m\mathbf{a}_1 + n\mathbf{a}_2.$$

The rotated angle of R1 layer relative to T layer which gives a commensurate structure is defined by equation:

$$\cos \theta(m, p) = \frac{3m^2 + 3mp + p^2/2}{3m^2 + 3mp + p^2}, \quad (5.1)$$

where $p = n - m$, p and m are coprime positive integers, $0 < \theta < \pi/3$.

The primitive vectors of the superlattice for a commensurate structure of angle $\theta(m, p)$ are as follows [gcd(p,s) is the greatest common divisor of p and s]:

(i) If gcd(p,1)=1,

$$\begin{bmatrix} \mathbf{t}_1 \\ \mathbf{t}_2 \end{bmatrix} = \begin{bmatrix} m & m+p \\ -(m+p) & 2m+p \end{bmatrix} \begin{bmatrix} \mathbf{a}_1 \\ \mathbf{a}_2 \end{bmatrix}. \quad (5.2)$$

(ii) If gcd(p,3)=3,

$$\begin{bmatrix} \mathbf{t}_1 \\ \mathbf{t}_2 \end{bmatrix} = \begin{bmatrix} m + p/3 & p/3 \\ -p/3 & m + 2p/3 \end{bmatrix} \begin{bmatrix} \mathbf{a}_1 \\ \mathbf{a}_2 \end{bmatrix}. \quad (5.3)$$

We observed a rotated angle of $\sim 27^\circ$. With equation (1), we know $m/n = 0.4126$ for $\theta = 27^\circ$.

Here, we give an approximate example, where $m=5$ and $n=12$ ($\text{gcd}(p,1)=1$), giving $m/n = 0.4167$, $\theta = 26.746^\circ$.

The vectors of the superlattice associated with the moiré pattern are expressed as:

$$\begin{cases} \mathbf{t}_1 = 5\mathbf{a}_1 + 12\mathbf{a}_2 \\ \mathbf{t}_2 = -12\mathbf{a}_1 + 17\mathbf{a}_2 \end{cases}$$

The resulting moiré pattern is shown in *Figure 5.6*.

5.5. Calculations

Density functional theory (DFT) calculations based on slab model were performed with the Vienna Ab-initio Simulation Package (VASP)¹⁹²⁻¹⁹³ installed at the SciNet¹⁹⁴ supercomputer clusters of Compute Canada. DFT calculations were made using the Perdew-Burke-Ernzerhof approximation (PBE)¹⁹⁵ of the exchange-correlation potential, the projector augmented wave (PAW)¹⁹⁶⁻¹⁹⁷ method, and a plane-wave basis set. Final calculations were performed using zero-damping DFT-D2¹⁹⁸ and DFT-D3¹⁹⁹ methods of Grimme, a correction which takes into account vdW for potential energies and dispersion effects *via* a semi-empirical approach, yielding more accurate geometries of the adsorption structures compared to those obtained from uncorrected DFT calculations. Unless stated otherwise, all the calculations were first performed at the gamma point with an energy cut off of 450 eV, followed by a higher accuracy

level using 5-irreducible k -points ($3 \times 3 \times 1$ k -points) with the cut off energy of 750 eV, until the net force on each atom was less than 0.02 eV/\AA and the energy change between the two steps was smaller than 0.00001 eV . Except the bottom layer of graphene, all the atoms, including top layer of graphene, COF-1, and C_{60} molecular layers were relaxed during the simulation.

5.5.1. COF-1/graphene bilayer

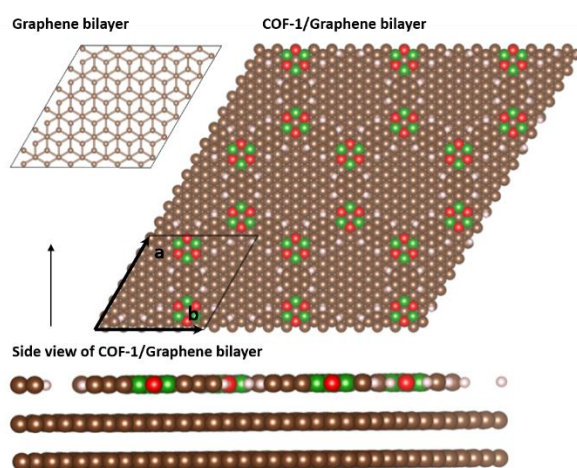


Figure 5.13 The optimized geometry of COF-1 on graphene bilayer.

The lattice parameter of a 6×6 graphene layer was first optimized to be 14.8 \AA (for the range of 12.76 \AA to 16.76 \AA in the step of 0.1 \AA). Then, an AB bilayer of graphene (144 atoms) was optimized in a unit cell with the dimension of $a=14.8 \text{ \AA}$, $b=14.8 \text{ \AA}$, $c=40.0 \text{ \AA}$, and the angle between \mathbf{a} and \mathbf{b} vectors equal to 60° . The graphene bilayer distance was calculated to be 3.25 \AA using DFT-D2 and 3.50 \AA using DFT-D3.

The optimum lattice parameter of COF-1 was found to be 15.2 \AA (for the range of 14.5 \AA to 15.3 \AA in steps of 0.1 \AA). To model COF-1 network on periodic graphene,

the lattice of the COF-1 was adjusted to be commensurate with graphene bilayer. Therefore, COF-1 was compressed from 15.2 Å to 14.8 Å (*i.e.*, by 2.6%). COF-1 was optimized for its most stable geometry and location with respect to the underlying graphene bilayer. The bottom layer of graphene was kept frozen, but the graphene top layer and COF-1 atoms were relaxed, here and for all subsequent calculations in which C₆₀ molecules were added. The graphene bilayer distance became 3.23 Å using DFT-D2 (3.49 Å using DFT-D3), close to the optimized distance described above. The optimized distance between COF-1 and the graphene top layer was found to be 3.30 Å (3.49 Å using DFT-D3).

5.5.2. C₆₀ molecules adsorbed on COF-1/graphene bilayer

The adsorption of one C₆₀ with a 6-ring facing down at three different adsorption sites top-boroxine-site (*Figure 5.14a*), top-phenyl-site (*Figure 5.14b*), and pore-site (*Figure 5.14c*), gave the following stable structures. In agreement with our previous molecular mechanics calculations,⁸⁰ the top-boroxine site was confirmed to be more stable than top-phenyl site (see Table 5.1). In the following discussion, unless stated otherwise, top-site refers to the top-boroxine structure. Top-site C₆₀ adsorption with a 5-ring facing down gave an energy within 0.004 eV difference to that of the 6-ring top-site. The P-T bilayer was also calculated (*Figure 5.14d*).

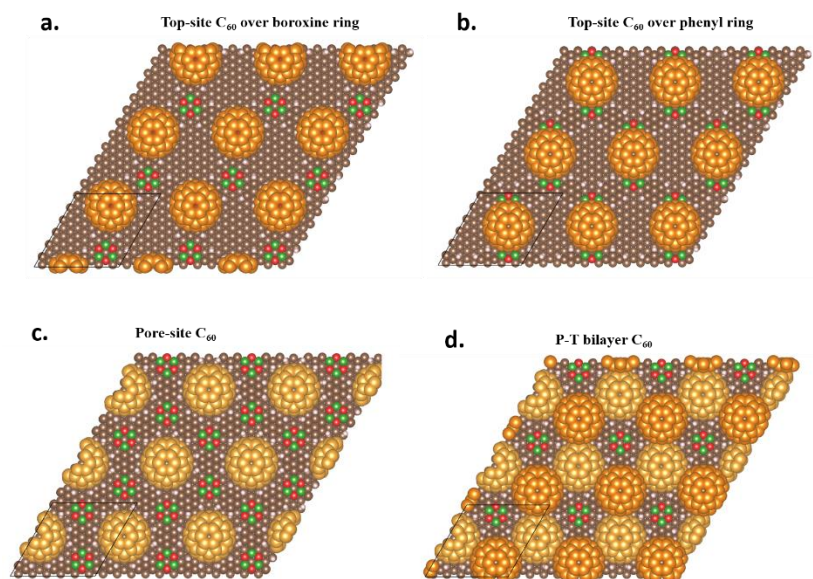


Figure 5.14 The DFT-calculated geometry for C_{60} on COF-1/graphene bilayer. (a) C_{60} over boroxine ring (T-layer), (b) C_{60} over phenyl ring, (c) Pore-site C_{60} (P-layer), (d) P-T bilayer C_{60} .

Starting from the optimized centred pore-site (Figure 5.14c), the off-centred pore-site C_{60} was simulated, at single point calculations using DFT-D3 at the gamma point with an energy cut off of 450 eV, by shifting centred C_{60} along zigzag and armchair directions of COF-1. These calculations showed that the centred pore-site adsorption is more stable than the simulated off-centred pore-site adsorption geometries (Figure 5.15).

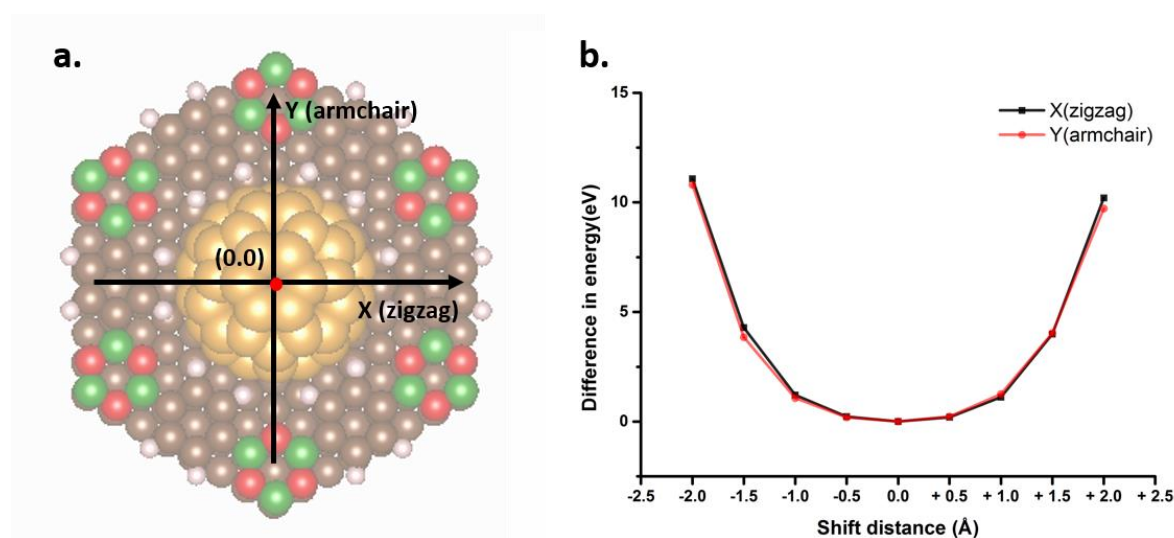


Figure 5.15 (a) Cartesian coordinate system for off-centred adsorption simulation, where origin is defined as the position of optimized pore-site. X and Y axes represent zigzag and armchair directions of COF-1 template. (b) The plot of energy change of different off-centred positions (along X and Y axes) with respect to optimized centred pore-site position (P-site Table 5.1, which gave -1.59 eV adsorption energy here under the accuracy described above). The distance of each step is 0.5 Å.

For the two-layer C₆₀, four structures were calculated: (1) two shift-structures (A-pattern shift and B-pattern shift), which were observed at heptanoic acid/HOPG interface, representing two directional shifts with respect to the given top-site C₆₀ (Figure 5.14a), and (2) two template-defined close-packed structures which have high symmetry (A-close packing and B-close packing), observed at TCB supernatant/HOPG interface. The shift structures are energetically much less stable than close packed structures. The adsorption energies of the R1 C₆₀ over the top-site structure for these structures are listed in Table 5.1. The final optimized geometries

are presented in *Figure 5.16*.

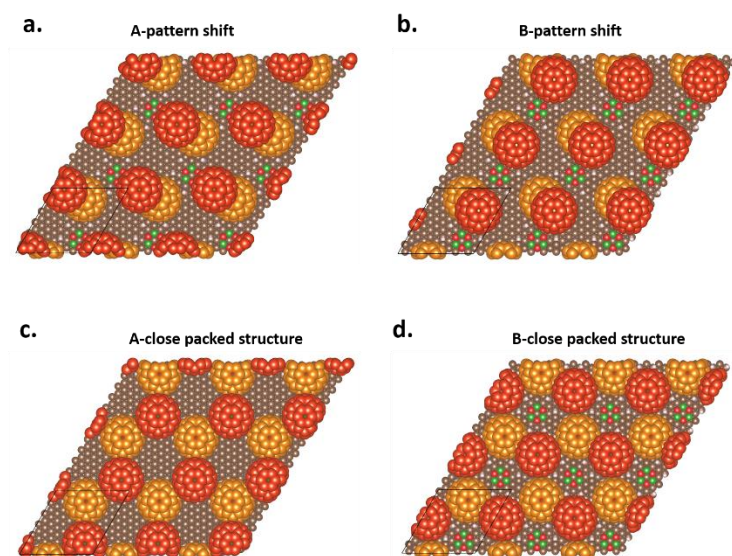


Figure 5.16 The DFT calculated geometry of R1 layer C₆₀ on T layer/COF-1/graphene bilayer. (a) A-pattern shift. (b) B-pattern shift. (c) A- close packing. (d) B- close packing.

C₆₀ growth of the R2 layer was simulated by adding a third C₆₀ molecule over the bilayer structure (*Figure 5.16a* and *b*). The adsorption energies of the R2 C₆₀ are listed in Table 5.1. The final optimized geometries of different architectures are shown in *Figure 5.17*.

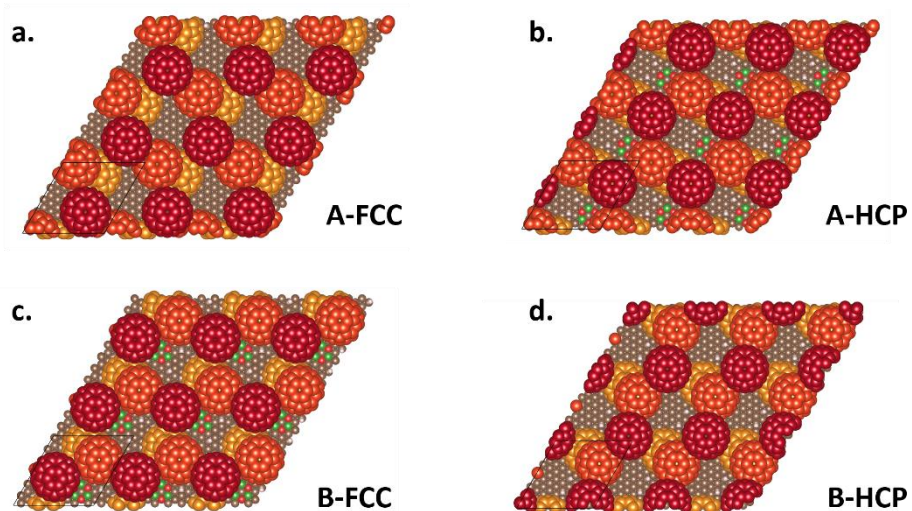


Figure 5.17 The DFT calculated geometry of R1 and R2 layer C_{60} on T layer/COF-1/graphene bilayer. (a) A-FCC architecture. (b) A-HCP architecture. (c) B-FCC architecture. (d) B-HCP architecture.

Table 5.1 The adsorption and total cohesive energy of 2D-to-3D growth of C₆₀ (1st, 2nd, and 3rd layer of C₆₀ formed of one, two, and three C₆₀ molecular layers, respectively) on COF-1/graphene bilayer

	Single layer			Bilayer						Triple layer			
	Porc-site (P-site)	Top-phenyl ring	Top-boroxine ring (T-site)	P-T bilayer	A-pattern shift	B-pattern shift	A-close packed	B-close packed	Shift-pattern without COF-1/graphene bilayer	A-FCC	A-HCP	B-FCC	B-HCP
R2 C ₆₀ [#]										-0.61 eV (-0.58 eV)	-0.59 eV (-0.57 eV)	-0.79 eV (-0.59 eV)	-0.60 eV (-0.63 eV)
R1 C ₆₀ [#]					-0.21 eV (-0.23 eV)	-0.25 eV (-0.25 eV)	-0.73 eV (-0.72 eV)	-0.54 eV (-0.57 eV)	-0.20 eV (-0.22 eV) [-0.01]**	-0.85 eV (-0.77 eV)	-0.85 eV (-0.77 eV)	-0.89 eV (-0.79 eV)	-0.89 eV (-0.79 eV)
1 st C ₆₀	-1.60 eV (-1.58 eV) [#]	-0.42 eV (-0.43 eV)	-0.64 eV (-0.54 eV)		-0.64 eV (-0.54 eV)		-0.85 eV (-0.77 eV)	-1.44 eV (-1.34 eV)	-1.68 eV (-1.38 eV)	-1.49 eV (-1.42 eV)			
Total cohesive energy	-1.60 eV (-1.58 eV)	-0.42 eV (-0.43 eV)	-0.64 eV (-0.54 eV)	-2.36 eV (-2.36 eV)	-0.85 eV (-0.77 eV)	-0.89 eV (-0.79 eV)	-1.37 eV (-1.28 eV)	-1.18 eV (-1.11 eV)		-1.46 eV (-1.35 eV)	-1.44 eV (-1.34 eV)	-1.68 eV (-1.38 eV)	-1.49 eV (-1.42 eV)

[#]The adsorption energy of R1 C₆₀ is reported with respect to top-boroxine ring structure.

^{##}The adsorption energy of R2 C₆₀ is reported with respect to A- and B-pattern shift structures.

*DFT-D3 (values in parentheses)

**DFT (without dispersion correction)

5.5.3. Bader charge calculation

In order to elucidate the electrostatic interactions, we calculated Bader charge²⁰⁰⁻²⁰³ on these structures, starting from the top-site architecture, to see how the charge distribution may have led the subsequent growth of C₆₀.

In order to see the change of charge on each atom after the C₆₀ adsorption on the boroxine ring, the charge distribution of a free C₆₀ was deducted from assembled C₆₀ top-site/COF-1/graphene-bilayer (*Figure 5.14a*). Similarly, we calculated the charge change for the shift-structures and found that for the A-shift, the top-site C₆₀ is positively charged by 0.052 e and the R1 C₆₀ has gained 0.004 e. For the B-shift, the top-site C₆₀ is positively charged by 0.047 e and the R1 C₆₀ has gained 0.005 e.

Details are available in Table 5.2.

Table 5.2 The Bader charge for top-site and shift structures

Valence electrons (+ lost, - gained)	Free C ₆₀ , COF-1 and graphene bilayer	COF-1/graphene bilayer	Top-site	A-shift	B-shift
R1 layer C ₆₀	240.000			240.005 (-0.005)	240.004 (-0.004)
T-layer C ₆₀	240.000		239.948 (+0.052)	239.953 (+0.047)	239.948 (+0.052)
COF-1	138.000	138.102	138.146 (-0.044)	138.140 (-0.038)	138.155 (-0.053)
Graphene bilayer	576.000	575.898	575.906 (-0.008)	575.902 (-0.004)	575.893 (+0.005)

5.5.4. Solvent molecule (heptanoic acid) adsorption on COF-1/graphene bilayer

A single heptanoic acid molecule was optimized in the gas phase, and was subsequently located at the pore, top-boroxine, and top-phenyl positions of

COF-1/graphene bilayer model. For each adsorption site, the heptanoic acid molecule was simulated for two orientations as ‘up’ and ‘down’, corresponding to the direction of carboxyl group with respect to the surface. The COF-1/graphene bilayer atoms (*Figure 5.13*) were kept frozen, while the heptanoic acid atoms were relaxed for all the simulations. The calculations were performed using the DFT-D3 method at the gamma point with a cutoff energy of 450 eV. All other convergence parameters and functions were set identical to the previous simulations. The values reported in Table 5.3 show that in its ‘down’ orientation (carboxyl group directing towards the surface), the heptanoic acid molecule gives a higher adsorption energy for the three adsorption sites. Thus, the ‘down’ orientation was chosen for the subsequent simulations.

We note that while we based these geometries on our experimental results, the exact adsorption site for the solvent molecules cannot be determined from STM images. Hence these geometries should be taken as representative, rather than exact.

Table 5.3 Adsorption energy of one heptanoic acid at three adsorption sites

	Pore-site (P-site)	Top-phenyl ring	Top-boroxine ring (T-site)
carboxyl-down	-0.49 eV	-0.23 eV	-0.35 eV
carboxyl-up	-0.15 eV	-0.11 eV	-0.10 eV

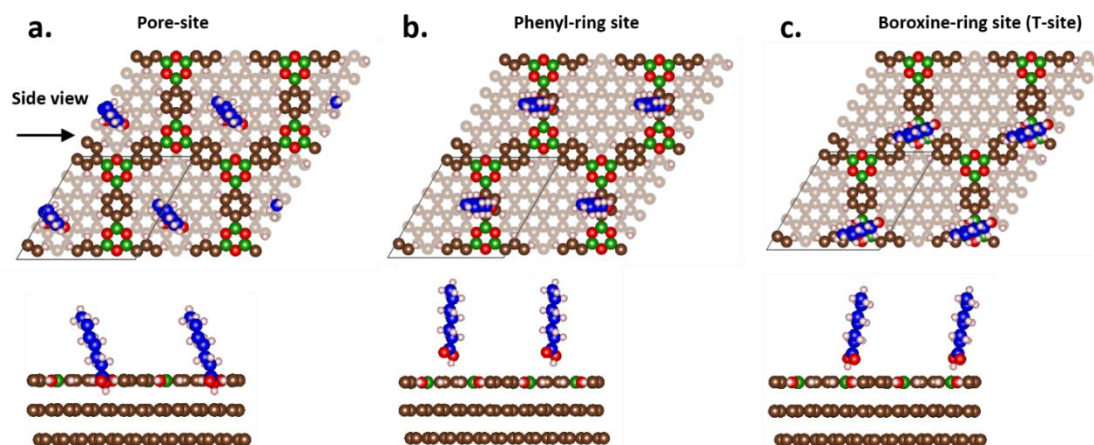


Figure 5.18 Optimized structures of adsorption of solvent molecules on COF-1/graphene bilayer. Heptanoic acid adsorbed at the pore-site (a), top phenyl-ring site (b) and top boroxine-ring site (c).

5.5.5. The co-adsorption of heptanoic acid in shift structures and template defined close packing structures

The total cohesive energies of T-layer C_{60} alone, the shift structures and template defined close packed structures with heptanoic acid molecules co-adsorbed at both P-site and T-site are reported in Table 5.4. The co-adsorbed optimized geometry of T-layer C_{60} is shown in *Figure 5.8b* and the optimized geometries of the shift structures and template defined close packing are shown in *Figure 5.19*. When co-adsorbed with heptanoic acid, the absolute cohesive energies of shift-pattern structures (A- and B-shift structures) are higher than their close-packed counterparts (A- and B-close packed structures), which is opposite to the trend in the absence of heptanoic acid (Table 5.1). These calculated results support the interpretation that pseudopolymorphism accounts for the experimental observations. In Table 5.4, we

find that the co-adsorption of solvent molecules contributes more stabilization in shift structures (-1.93 eV and -1.85 eV) than their close packed counterparts (-1.38 eV and -1.31 eV). Co-adsorption of solvent also perturbs the R1 C₆₀ packing geometries. For example, compared to the cases without solvent, R1 C₆₀ molecules move closer to surface by ~0.9 Å for shift structures, but away by ~3.0 Å for template-defined close packed structures, as shown in *Figure 5.19*. This is consistent with the hypothesis that it is the protruding alkyl chains that inhibit the formation of template-defined close packing.

Table 5.4 Total cohesive energies of T-layer C₆₀, shift structures and template-defined structures with co-adsorption of heptanoic acid molecules

dE (eV)	Top layer	A-shift	A-close packing	B-shift	B-close packing
Total cohesive energy*	-2.16 eV	-2.69 eV	-2.62 eV	-2.63 eV	-2.40 eV
Contribution of solvent co-adsorption in cohesive energy [#]	-1.69 eV	-1.93 eV	-1.38 eV	-1.85 eV	-1.31 eV

*dE(total)_{system+solvent}=E_{system+solvent}-(E_{COF-1/graphene bilayer}+E_{C60}+E_{solvent}); System=COF-1/graphene bilayer+ C₆₀

[#]dE(co-adsorption)=E_{system+solvent}-(E_{system}+E_{solvent})

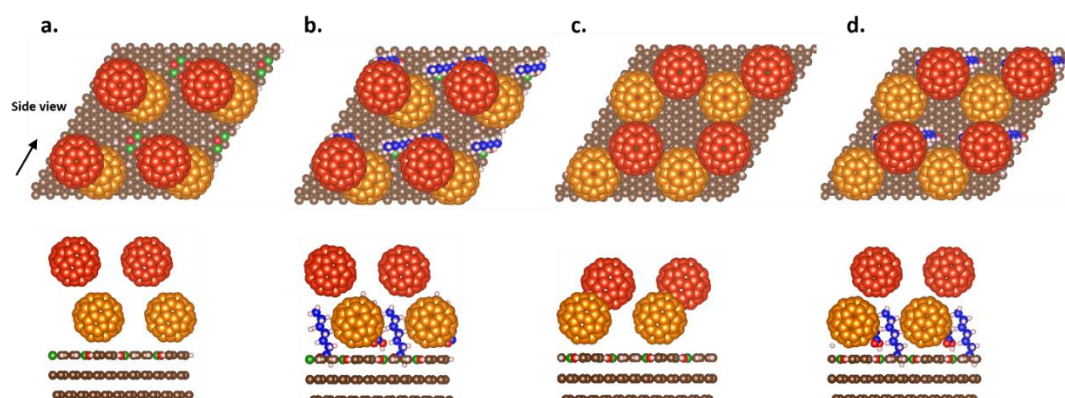


Figure 5.19 Comparing A-pattern shift (a, b) and A-close packing (c, d) optimized structures in the absence and presence of heptanoic acid molecules (P- and T- sites).

The structures shown in (a) and (c) are the same structure as *Figure 5.16a* and *Figure*

5.16c, respectively. The height of R1 C₆₀ in (b) is about 0.9 Å lower than (a), and that of (d) is about 3.0 Å higher than (c).

Chapter 6. Conclusions and perspectives

6.1. Conclusions

COF-1 has been used as a robust host for C_{60} fullerene guest molecules at the solution/solid interface and under ambient conditions. The COF-1 layer was routinely synthesized on HOPG and the H/G structures can be produced through the introduction of C_{60} solution in different solvent and concentrations.

STM investigations have demonstrated the possibility for COF-based H/G architectures at monolayer thickness, as discussed in Chapter 3. At both the heptanoic acid/HOPG interface and in dried films, COF-1 presents a lattice with two distinct fullerene adsorption sites: a pore site, where the C_{60} molecule is adsorbed on the underlying HOPG, and a top site, where the fullerene is adsorbed on the boroxine ring. Dried COF-1/fullerene films can be produced either through drop deposition or by dipping the HOPG-supported COF-1 into the fullerene solution.

The method of synthesizing porous COF-1 layer on HOPG from solution in TCB was also developed. Using TCB-based synthesis, two different epitaxial orientations of COF-1 were observed, with a well-defined loop boundary defect formed by a chain of pentagonal ring and heptagonal ring separating the two domain orientations. STM images collected at the TCB/solid interface reveal the adsorption of TCB within the hexagonal pores of the COF-1 template. DFT calculations suggest that this host/guest

structure is stabilized by Cl...H hydrogen bonding. The presence of the loop boundary defect permitted the investigation of the effect of pore shape and size on TCB adsorption: no TCB was adsorbed in the pentagonal pores, but the larger heptagonal pores accommodated two TCB molecules, stabilized through a combination of Cl...H and Cl...Cl bonding. Including C₆₀ in the TCB solution allowed us to investigate the molecular recognition of template. When both C₆₀ and TCB are present at the solution/solid interface, TCB molecules are selectively trapped in the pores of the COF-1 template, whereas fullerenes adsorb on top of the COF-1 in sites identified as top sites.

The monolayer COF-1 network was also found to be able to induce the self-assembly of fullerene into multiple layer structures at the solution/solid interface. The template-defined packing, which deviates from standard close packing, depends on the solvent for the fullerene molecules: a template-defined close-packing motif is achieved using TCB as solvent, whereas lower-density quasi-close-packed polymorphs are observed when using heptanoic acid as solvent. The solvent-dependent polymorphism and morphologies can be described in terms of a template-driven solvent co-adsorption effect. The results presented here highlight the important role of the solvent, not just in influencing 2D self-assembly, but also in defining 3D architectures. Through a judicious combination of solvent and template, (pseudo)polymorphic films can be formed with packing geometries that have not been observed under other conditions. This suggests a pathway towards using the

combination of 2D template and solvent effects to control molecular self-assembly precisely into the third dimension, even in the absence of directional solute-solute or solute-solvent interactions.

In this thesis, the predictable trapping of fullerene molecules using COF-1 was shown as a proof-of-principle example of the utility of 2D boronic acid based COFs for applications in sensing or trapping molecules where the COF is exposed to a solution containing the target molecule. The selective adsorption of TCB and C₆₀ in COF-1 suggests that the different adsorption sites in the COF-1 lattice can be used to separate guest molecules by different interactions, opening opportunities for applications in molecular patterning and recognition. The combination of two independent tuning parameters, COF-1 template and solvent, suggests an improved control over phase behaviors in molecular crystallization, which could give rise to previously unobserved phases in a range of related advanced materials.²⁰⁴

6.2. Perspectives

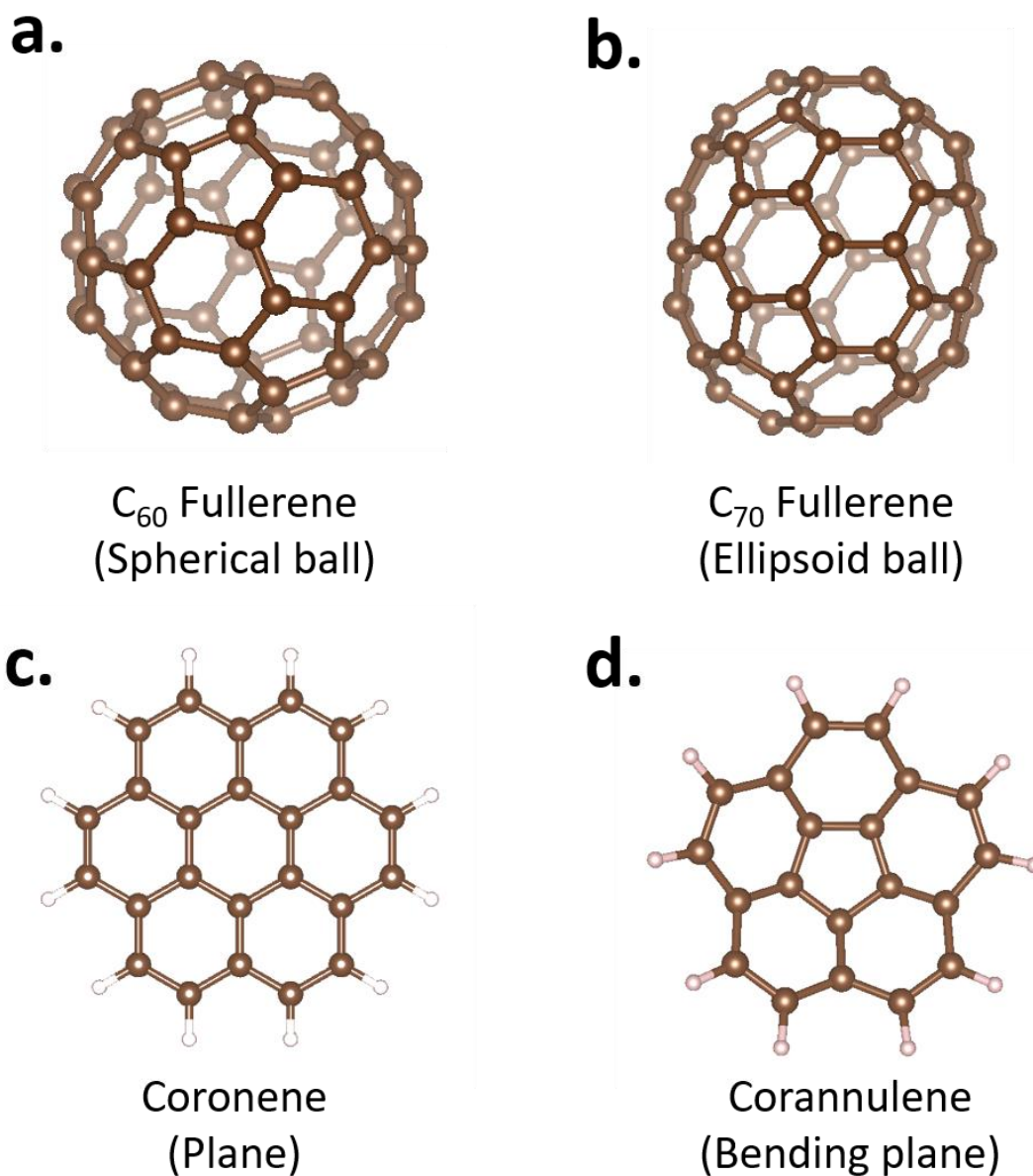


Figure 6.1 Scheme of (a) C_{60} , (b) C_{70} , (c) Coronene, and (d) Corannulene molecules.

Besides the guest molecule C_{60} , it is also possible to introduce other guest molecules.

C_{70} is another important fullerene, consisting of 25 hexagonal and 12 pentagonal rings arranged with icosahedral D_{5h} symmetry, as shown in *Figure 6.1b*. In contrast to the

spherical and isotropic C₆₀ molecule, C₇₀ can be treated as an ellipsoid with an elongated aspect ratio that gives rise to its anisotropy, *i.e.*, elliptical shape and anisotropic polarizability. The electric dipole polarizability of C₇₀ exceeds that of C₆₀ by 25%,²⁰⁵ enhancing electrostatic interactions between C₇₀ molecules as well as with other small organic molecules, such as COF-1 template. Thus, anisotropic effects may play an important role in the H/G structure when C₇₀ used as guest molecules.⁷⁷ This investigation may contribute to our fundamental knowledge of the effects of molecular anisotropy in the epitaxial growth of molecular crystals, bridging the properties of individual constituent and final architecture of assembly, which provides the basis for rationally designing 3D objects through bottom-up nanotechnology.

Besides fullerene derivatives with a ball-like geometry, planar circulenes, defined as a central n-sided polygon macrocyclic arene surrounded and fused by benzenoids, are another group of guest molecules for potential study. With COF-1 as template, we can also introduce coronene and corannulene (CORA) onto the pre-prepared COF-1. CORO and CORA are similar to each other, although they differ in presenting planar and curved geometries, respectively, as shown *Figure 6.1c* and *d*. These molecules have already attracted an intensive interest in the non-covalent H/G system in molecular manipulation and growth into third dimension.^{59, 206-207}

Besides architectures comprising single types of guest molecules, it is also possible to investigate binary guest systems by simultaneously introducing two types of guests to COF-1. Combining coronene and fullerene and corannulene and fullerene in COF-1

can provide a fundamental understanding about the interactions between host and guest or interaction between two types of guest molecules. The curved corannulene molecules can interact with fullerene through a concave-convex interaction,²⁰⁸ differing from planar coronene and fullerene, as shown in *Figure 6.2*. This approach not only provides insight into the H/G system but also offers important information about designing heteronanostructures that precisely position multiple components out of plane.

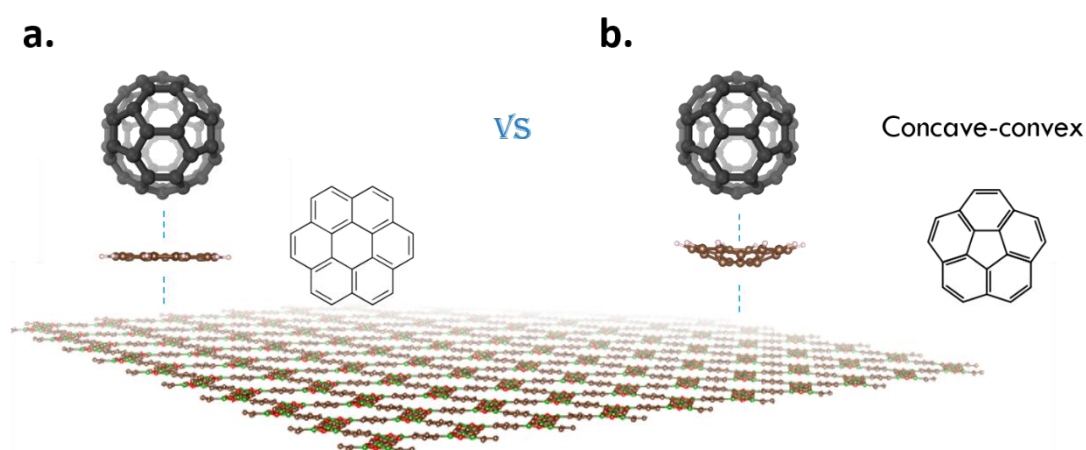


Figure 6.2 Schematically illustration of binary guest molecule systems in COF-1. **(a)** The system includes fullerene and coronene guest molecules. **(b)** The system includes fullerene and corannulene. The planar and curved circulene guest molecules will interact with COF-1 template and fullerene differently.

Appendix A Abbreviations

BA	boronic acid
BTA	benzene-1,3,5-tricarbaldehyde
BDBA	1,4-benzenediboronic acid
BTB	1,3,5-benzenetribenzoic acid
C ₁₈ ISA	5-octadecyloxyisophthalic acid
CORO	coronene
CORA	corannulene
COFs	covalent organic frameworks
DBA	dehydrobenzo annulene
DFT	density functional theory
ESP	molecular electrostatic potential
FCC	face-centred cubic
GB	grain boundary
HCP	hexagonal closed packing
HOPG	highly ordered pyrolytic graphite
H/G	host/guest
ISA	isophthalic acid
LDOS	the local density of states
NN4A	tetra-acidic azobenzene

OLEDs	organic light-emitting diodes
PAW	projector augmented wave
PBE	Perdew-Burke-Ernzerhof approximation
PDA	p-phenylenediamine
SEM	scanning electron microscopy
STM	scanning tunneling microscopy
TCNB	1,2,4,5-tetracyanobenzene
TMA	trimesic acid
TPTC	terphenyl-3,3",5,5"-tetracarboxylic
TCB	1,2,4-trichlorobenzene
vdW	van de Waals
XRD	X-ray diffraction
2D	two-dimensional
VASP	Vienna Ab-initio simulation package
Pt	Platinum
Ir	Iridium
W	Tungsten
\hbar	reduced planck constant
Ψ, χ, ϕ	wavefunction
U	potential function
E_F	Fermi level

e	elementary charge
V	bias voltage
ϕ	work function
ρ	density of states
μ	chemical potential
k_B	Boltzmann constant
T	temperature

Appendix B RÉSUMÉ

L'Introduction

Les COFs (Covalent Organic Frameworks en Anglais) ont fait l'objet d'une attention considérable depuis leur toute première synthèse en 2005.³⁹ Ils se présentent sous la forme de solides cristallins poreux robustes, face aux contraintes mécaniques et thermiques, et peuvent être fonctionnalisés dans une perspective d'application pour le futur.⁹²⁻⁹³ En utilisant des molécules précurseurs avec les différents groupes fonctionnels, les COFs à base d'acide boronique (BA) peuvent être adaptés pour des applications spécifiques, par exemple le stockage d'hydrogène⁹⁴⁻⁹⁵ et d'autres gaz,⁹⁶⁻⁹⁷ ou l'exploitation de la photoconductivité.⁹⁸⁻⁹⁹ Un certain nombre d'études expérimentales¹⁰⁰⁻¹⁰¹ et théoriques¹⁰²⁻¹⁰³ se sont concentrées sur les hétérojonctions massives formées par des COFs avec des donneurs de charge et des accepteurs ordonnés en ciblant des applications dans les photovoltaïques.

A l'instar de l'empilement de graphène dans le graphite, le COF a une structure en couches, avec des interactions non-covalentes (dispersives et électrostatiques) en stabilisant les plans de base définis par les COFs bidimensionnel (2D)¹⁰⁴ en cristaux tridimensionnel (3D). Il y a donc un intérêt important à isoler des feuilles 2D de COF, afin de retrouver, par l'analogie avec des propriétés exceptionnelles, des matériaux du graphène.¹⁰⁵⁻¹⁰⁶ Des plaquettes de COF avec l'épaisseur des couches plusieurs peuvent être produites en délaminant les COFs 3D par la sonication¹⁰⁷⁻¹⁰⁸ ou par

l'exfoliation mécanique.¹⁰⁹ La synthèse directe de la monocouche de COF 2D sur un substrat permet de définir l'orientation des COFs, ce qui est nécessaire pour la plupart des applications,¹¹⁰⁻¹¹¹. Il est également possible, par ce biais d'utiliser les réactions vapeur-solide adaptées pour produire des COF 2D.¹¹²

La synthèse de COF confinée en surface a déjà été réalisée par auto-condensation de BDBA sous UHV. Dans ces conditions, l'élimination rapide des molécules d'eau issues de la réaction, empêche la réversibilité et conduit à l'obtention d'un réseau de poly (BDBA) relativement désordonné,^{45, 113} une monocouche de COF-1.³⁹ Lorsqu'ils sont synthétisés en surface à la pression ambiante et à une humidité élevée, la correction des défauts dans le réseau COF conduit à un ordre structurel supérieur.⁴⁸⁻⁴⁹ Comme cela a été démontré dans les COFs 3D,¹¹⁴ la gamme des dérivés BA disponibles permet de réguler les propriétés structurelles des COFs synthétisés en surface.⁵⁰

D'autre part, un travail important a été effectué sur les architectures H/G (hôte/invité) confinées en surface en monocouche, qui reposent sur des interactions hiérarchiques: l'interaction liant les molécules hôte ensemble est plus forte que cela liant la molécule invitée à la molécule hôte. Si les réseaux formés par les molécules hôte sont généralement maintenus par des liaisons d'hydrogène,^{55, 74, 76, 83}, des forces van der Waals (vdW),^{54, 121} ou des interactions du ligand-métal,¹¹⁶ l'adsorption des molécules invitées se fait principalement par des interactions plus faibles, typiquement des forces de dispersion de Londres avec l'hôte ainsi qu'avec le substrat sous-jacent. La

formation et la caractérisation de ces réseaux H/G ont été effectuées à la fois dans des conditions UHV^{59, 76, 115-116} et à l'interface de solution/solide.^{54-55, 81}

La chimie H/G dans les réseaux supramoléculaires 2D a été largement étudiée comme un moyen d'immobiliser un grand panel de molécules invitées, avec des applications potentielles dans la technologie de séparation, la reconnaissance moléculaire ainsi que la détection, la catalyse et la structuration à l'échelle nanométrique.^{22, 120} La reconnaissance mutuellement spécifique entre le réseau hôte et les molécules invitées, c'est-à-dire une forme de reconnaissance moléculaire, est au cœur de la chimie hôte-invité.¹²⁴⁻¹²⁵ Dans le but de sélectionner les liaisons mises en jeu, les stratégies de conception se reposent sur le choix de la molécule d'hôte en vue de sa géométrie : telle que la taille des pores,⁶⁰⁻⁶¹ la forme⁶² et la chiralité.⁶⁴ Toutefois, l'utilisation spécifique de l'interaction d'entre hôte/invité est beaucoup moins exploitée.¹²⁶ Ceci est principalement dû aux limitations de la force d'interaction hiérarchique imposée par les modèles d'hôtes auto-assemblés. De plus, la croissance des réseaux supports, capables de former des structures H/G,^{22, 120} s'est révélée être une approche favorable pour contrôler la cristallisation dans la troisième dimension en utilisant des moléculaires précurseurs. Par exemple, la formation d'une structure bicouche Kagomé bicouche par les liaisons d'hydrogène⁷³ et l'auto-agrégation d'hétérocyclènes π -empilés⁷⁴ ont été observés. Ces exemples démontrent la possibilité de croissance dans la troisième dimension, perpendiculaire à la surface, à partir d'une couche 2D H/G. L'utilisation de molécules invitées non planaires, par exemple des fullerènes et

leurs dérivés, lorsqu'elles sont stabilisées par une interaction faible avec des modèles 2D, peut favoriser des configurations qui s'écartent de l'encapsulation standard en raison de la structure définie par le support.^{23, 75-78} La relation intriquée entre les fullerènes piégés et la croissance d'une deuxième couche d'un cadre supramoléculaire représente une interaction coopérative des espèces H et G.⁷⁹

On trouve de nouvelles opportunités pour la stabilisation des molécules invitées outre que les réseaux auto-assemblés. Par rapport à ces derniers présentant des liaisons non-covalentes, la robustesse des COFs est un réel avantage pour la préparation de systèmes avec des molécules hôtes covalentes, ouvrant ainsi la porte à une gamme de nouveaux matériaux hôtes-invités fonctionnels.

Dans cette thèse, des images de microscopie à effet tunnel (STM en anglais) montrent que le COF-1 en monocouche au soutien de surface, peut agir comme une architecture d'hôte pour les molécules de fullerène C₆₀, piégeant de manière prévisible les molécules dans certaines conditions. Les molécules C₆₀ s'adsorbent sur COF-1 dans deux sites différents, le site du sommet (T) et le site du pore (P). Les fullerènes s'occupent le réseau COF-1 à l'interface acide heptanoïque/HOPG et dans les couches séchées du réseau COF-1/fullerène qui peuvent être synthétisées soit par dépôt goutte à goutte de solution de fullerène, soit par une synthèse de type bandelette dans laquelle le COF-1 fabriqué surface est brièvement trempé dans la solution de fullerène.

Le COF-1 peut être synthétisée à partir de différents solvants. Lorsque le

1,2,4-trichlorobenzène (TCB) est utilisé, les images STM révèlent l'adsorption de TCB dans le pore hexagonal de la matrice COF-1 à l'interface TCB/HOPG. Une limite de boucle bien définie formée par une chaîne de pores pentagonaux et heptagonaux nous a permis d'étudier l'effet de la forme et de la taille des pores sur l'adsorption du TCB. Les résultats obtenus suggèrent que les effets géométriques et de taille sont importants pour la liaison du TCB. Lorsque C_{60} et TCB sont tous deux présents à l'interface TCB/HOPG, les molécules TCB sont sélectivement piégées dans le site poreux P, tandis que les fullerènes sont adsorbés sur le site T de COF-1. Alors que la première structure est stabilisée par des liaisons d'hydrogène Cl ... H, cette dernière est contrôlée par les interactions de vdW. Ces résultats suggèrent que les COFs 2D poreuses en surface peuvent lier sélectivement différentes molécules sur des sites spécifiques via différents types d'interactions et que les COFs peuvent être utilisées comme un moyen puissant pour la reconnaissance et la structuration des molécules invitées.

De plus, un COF-1 2D peut soutenir des molécules invitées C_{60} traitées par une solution pour former différents arrangements dont la structure et la topologie dépendent du solvant via un processus de croissance 2D à 3D. Lorsque le TCB est utilisé comme solvant, les molécules C_{60} forment une structure dense définie par le support. Lorsque l'acide heptanoïque est utilisé comme solvant, on observe une gamme d'architectures de faible densité qui s'écartent de la structure dense définie par le support. Cette différence est attribuée à la co-adsorption des molécules de solvant

de l'acide heptanoïque, qui n'est obtenue qu'en présence de la matrice. Ce travail démontre la possibilité de contrôler précisément l'auto-assemblage moléculaire pour former des structures 3D grâce à la combinaison sinéquanone des effets du support et du solvant.

Résultats et discussions

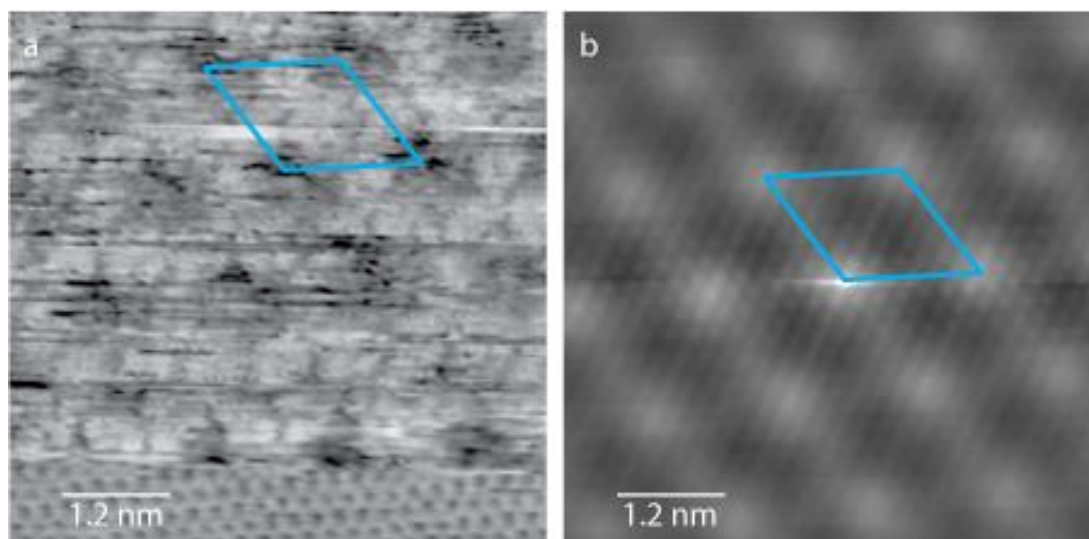


Figure 1 (a) Image révélant simultanément la résolution moléculaire de la structure COF-1 (en haut) et la résolution atomique du HOPG sous-jacent (en bas). Conditions d'image: la tension de balayage $V = -800$ mV, le courant de tunnel $I = 100$ pA (en haut); $V = -19$ mV, $I = 1000$ pA (en bas). (b) Correction autocorrélée de l'image STM montrée en (a). Le petit réseau (HOPG) et le grand réseau (COF-1) sont commensurables. Le COF-1 s'aligne avec le HOPG le long des deux directions du réseau, chaque vecteur unitaire ayant une longueur identique de six constantes de réseau HOPG.

Le support COF-1 est préparé sur HOPG selon des méthodes approuvées dans la littérature.⁴⁹⁻⁵⁰ Les anneaux de boroxine (B_3O_3) sont formés par la cyclocondensation de trois monomères de BDBA. On obtient une structure étendue de COF-1, qui consiste en des cavités hexagonales. Les mesures STM révélant simultanément le réseau atomique du HOPG et la maille du COF-1 indiquent que le COF-1 s'est aligné avec le HOPG avec une cellule épitaxiale 6×6 , comme le montre la *Figure 1*. Cela

correspond à un paramètre de réseau de 1.476 nm, et suggère une légère compression par rapport à la périodicité mesurée par la diffraction des rayons X , dont la valeur est de 1.54 nm pour le solide COF-1 en volume.³⁹ Dans toutes les expériences, la présence de COF-1 sur la surface HOPG est confirmée par l'imagerie STM, qui montre la présence du réseau en nid d'abeilles pouvant s'étendre sur des domaines de taille de dizaines de nanomètres.

Après d'avoir confirmé la présence de COF-1 sur la surface, une solution de fullerène C₆₀ dans de l'acide heptanoïque est déposée par la goutte sur le COF. Après le dépôt de la solution de fullerène, le COF-1 est encore visible sur les images STM, et une adsorption stable des fullerènes est observée.

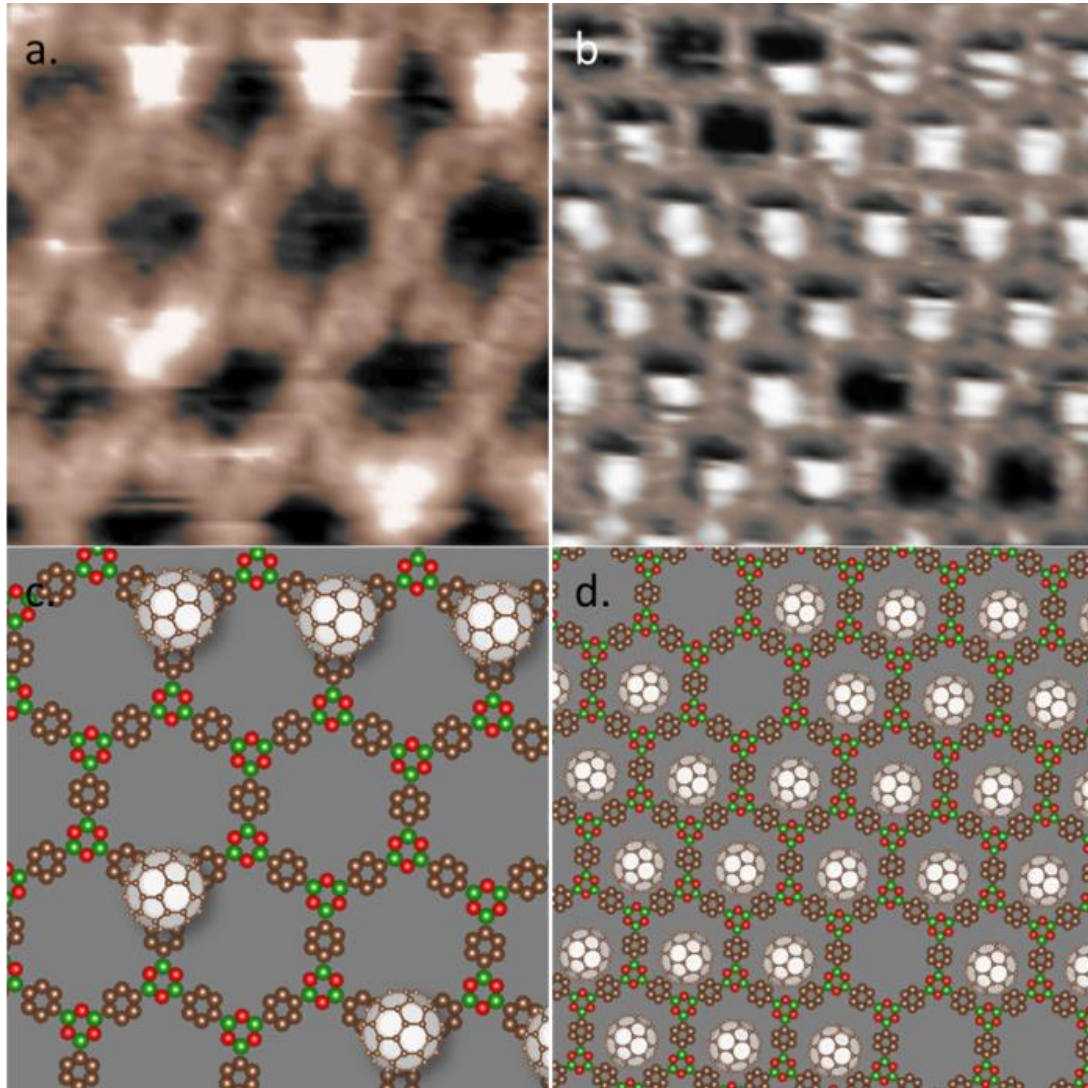


Figure 2 Structures H/G à l'interface solution/solide. Les images en (a) et (b) montrent les géométries d'adsorption de fullerène observés. On désigne respectivement les sites en haut (T) et les sites de pore. (P) Les structures dans (c) et (d) montrent des modèles proposés pour ces sites d'adsorption. Conditions de balayage: la tension de balayage $V = -800$ mV, le courant de tunnel $I = 100$ pA. Largeurs d'image (a) 5.3×5.3 nm² et (b) 7.7×7.7 nm².

En utilisant une solution diluée de fullerène (2×10^{-5} M), on obtient une densité de

fullerène relativement faible, ce qui permet de discerner clairement la position des molécules d'invité fullerène, comme le montrent les *Figures 2a* et *b*. Deux sites d'adsorption de fullerène différents peuvent être identifiés. Sur la *Figure 2a*, le COF-1 est visible sous la forme d'un réseau hexagonal à faible contraste, alors que les protrusions brillantes indiquent les positions des molécules de fullerène. Dans cette image, les molécules de fullerène ne se trouvent pas dans les pores de la structure hôte, comme observé pour d'autres systèmes de manière générale.^{55, 60, 115} Chaque molécule de fullerène est adsorbée au sommet d'un cycle boroxine du COF. Nous désignons ce site, représenté schématiquement sur la *Figure 2c*, comme un site en haut (T). Une géométrie d'adsorption similaire sur le réseau hôte a été observée pour l'adsorption de C_{60} sur des macrocycles oligothiophéniques, où un complexe donneur-accepteur stable 1: 1 est formé entre le C_{60} et le macrocycle oligothiophène riche en électrons.⁵⁴ Les forces électrostatiques sont également importantes dans COF-1, comme le montre la structure cristalline 3D COF-1 en volume. Ce dernier présente un empilement ABAB (décalé) des plans de base 2D, un anneau de benzène se place alors au-dessus d'un anneau de boroxine.³⁹

Les molécules invitées fullerène peuvent également s'adsorber dans les pores de la maille BDBA. Nous désignons ce site d'adsorption comme le site de pore (P) et ce dernier est légèrement décentré dans le pore de BDBA (*Figure 2d*). Sur la *Figure 2b*, les hôtes fullerènes s'apparaissent localisés à l'intérieur des pores COF-1. Puisque cette image a été acquise par balayage du bas vers le haut, nous interprétons

l'apparence asymétrique des molécules invités comme le résultat d'une adsorption décentrée (plutôt que, par exemple, d'une interaction attractive entre la pointe et l'échantillon, qui devrait conduire à un contraste lumineux en haut des pores.). Le site d'adsorption semble s'occuper la même position dans le pore pour tous les fullerène observés sur la *Figure 2b*. Nous avons précédemment observé un positionnement similaire des fullerènes dans des réseaux hôtes d'oligothiophène liés à l'hydrogène, où nous avons attribué cette structure à l'ordre électrostatique résultant d'un transfert partiel de charge vers le fullerène.⁸³

Bien que nous n'ayons pas réalisé d'étude systématique, nous avons observé de façon anecdotique une préférence pour l'adsorption des fullerènes sur le site (l'adsorption sur le site T est observée environ de dix fois plus fréquemment que l'adsorption en site P). L'adsorption de l'acide heptanoïque dans le pore, comme cela a été observé pour d'autres nanostructures 2D poreuses à l'interface de solution/solide, pourrait affecter de la cinétique d'adsorption du fullerène du site des pores, rendant l'adsorption sur le site T favorable.¹¹⁷

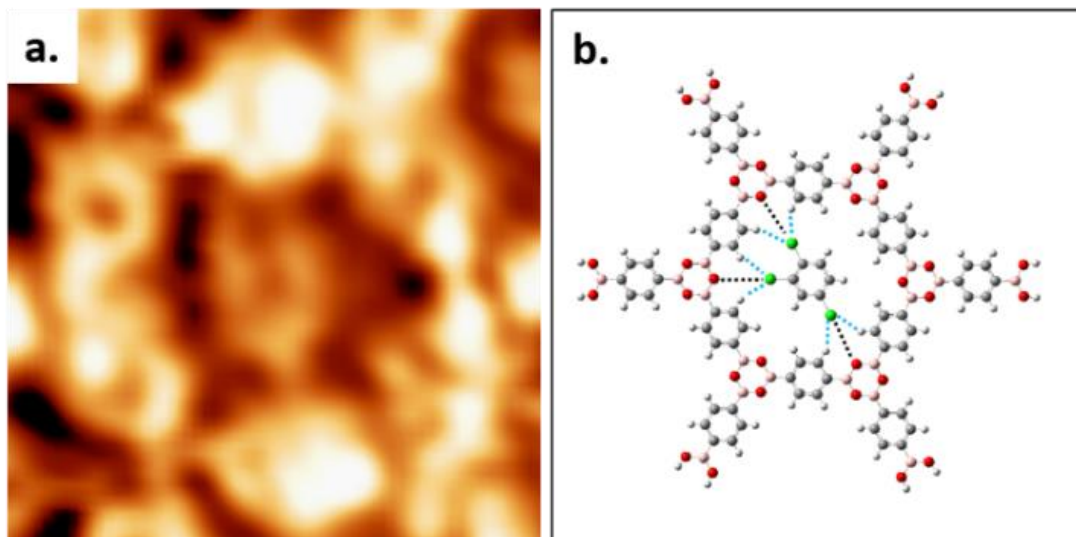


Figure 3 (a) Image STM détaillée d'une molécule de TCB adsorbée dans le cycle hexagonal formé par COF-1. Largeur de l'image: 2.1 nm. Conditions de balayage: $V = -1000$ mV, $I = 100$ pA. (b) Structure calculée par DFT d'un TCB dans les pores hexagonaux (M06-2X/LANL2DZ). Les lignes bleues et noires pointillées représentent les interactions Cl...H et Cl...O, respectivement.

Lorsque le COF-1 est synthétisé à partir du solvant TCB, des images STM haute résolution réalisées en interface TCB/HOPG nous permettent d'élucider la structure hôte-invité formée par le pore hexagonal des molécules COF-1 et TCB, comme le montre la *Figure 3a*. Les six cycles phényle dans le squelette de COF-1 peuvent être facilement distingués, tout comme les caractéristiques submoléculaires associées à la molécule de TCB adsorbée. Ces caractéristiques peuvent correspondre aux trois atomes de chlore ou au contraste du noyau benzénique, et leur présence suggère une adsorption stable de la molécule de TCB (c'est-à-dire que la molécule ne tourne pas).⁵⁹ Nos calculations DFT en phase gazeuse suggèrent que l'adsorption de TCB est

stabilisée par des liaisons d'hydrogène Cl...H, comme indiqué sur la *Figure 3b*; La densité électronique associée aux atomes de chlore dans la molécule TCB est répartie de manière anisotrope.¹³⁴ La bande nucléophile orthogonale à la liaison covalente, avec une densité électronique plus élevée et présentant un potentiel électrostatique négatif, forme des liaisons d'hydrogène X...H avec des atomes d'hydrogène voisins sur le squelette COF-1 (ligne bleue en pointillés).¹³⁵ Bien que le trou σ des atomes de chlore pointe vers l'atome d'oxygène nucléophile de la COF-1 (ligne noire pointillée sur la *Figure 3b*), l'interaction d'entre le chlore et l'oxygène est filtrée par les hydrogènes sur les cycles phényle. Le calcul DFT confirme que la distance de chlore-oxygène est trop grande ($\sim 4.38 \text{ \AA}$) pour permettre une interaction significative.

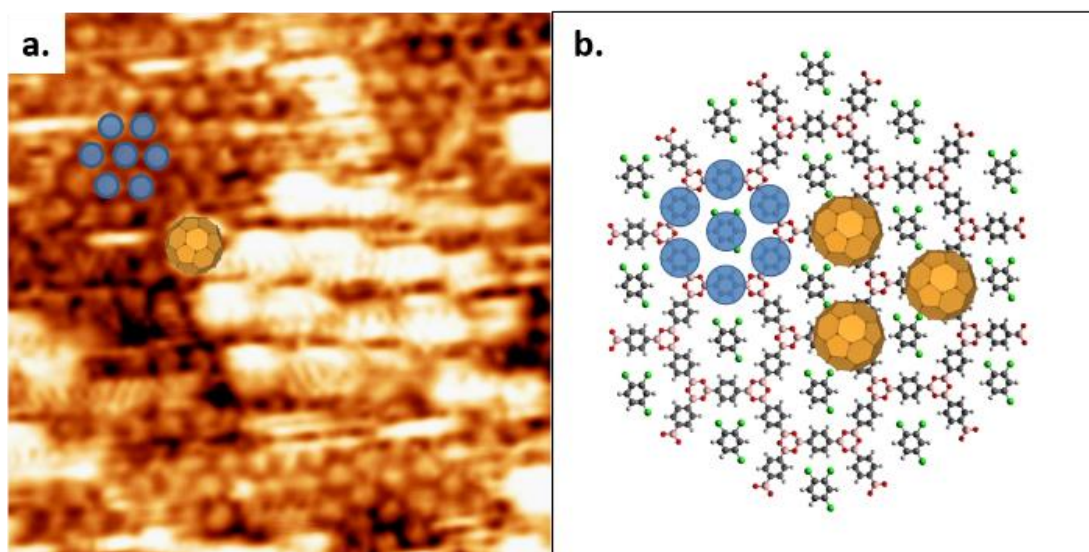


Figure 4 (a) La formation sélective du site supérieur dans le système $C_{60}/COF-1$. Largeur de l'image: 12 nm Conditions de balayage: $V = -800 \text{ mV}$, $I = 100 \text{ pA}$. (b) Image schématique de la formation sélective du site principal dans le système $C_{60}/COF-1$. Les cercles bleus ombrés sur les anneaux de benzène représentent la

structure compacte en arrière plan de l'image STM. Les molécules C₆₀ du site en haut sont placées sur les boroxines, correspondant aux structures plus larges et plus brillantes en (a).

La *Figure 2* montre que les molécules C₆₀ introduites à partir d'une solution contenant de l'acide heptanoïque en tant que solvant s'adsorbent sur la matrice COF-1 dans deux sites différents, le site en haut et le site de pore.⁸⁰ La géométrie T-site correspond à l'adsorption de la molécule de fullerène sur le cycle boroxine et le site de pore correspond à l'adsorption d'une molécule de fullerène dans le pore hexagonal. Cependant, les molécules de C₆₀ introduites à partir de la solution dans TCB présentent un comportement différent, comme le montre la *Figure 4a*. Une interprétation des données STM est représentée sur la *Figure 4b*. Nous attribuons le motif hexagonal serré aux molécules TCB adsorbées dans les pores COF-1 (indiqués par des cercles bleus hachurés sur les *Figures 4a* et *b*) et le domaine hexagonal à contraste élevé, d'une périodicité plus importante, aux molécules C₆₀ adsorbées sur les sites en haut. L'adsorption sur site T de C₆₀ est en accord avec la géométrie calculée, où l'architecture est stabilisée par les interactions vdW.⁸⁰

La littérature de plus en plus diversifiée sur les architectures H/G basées sur COF-1 suggère que le solvant utilisé pour le dépôt de C₆₀ joue un rôle important dans l'adsorption des molécules invitées. Le travail de Plas montre que les molécules C₆₀ se déposent couche par couche à partir de la matrice COF-1 dispersée dans le 1-phényloctane. Ce résultat suggère que le solvant n'entre pas en compétition avec les

molécules C_{60} pour l'adsorption dans le site de pore.¹²² En utilisant l'acide heptanoïque comme solvant, nous avons observé de façon anecdotique une préférence pour l'adsorption des fullerènes sur le site en haut, suggérant que l'acide heptanoïque peut entrer en compétition pour l'adsorption dans le site de pore. Combiné avec nos résultats, ceci suggère que le solvant peut être utilisé pour sélectionner le site d'adsorption initial pour les fullerènes. Ainsi le TCB et le 1-phényloctane choisiront respectivement pour l'adsorption du site en haut et du site de pore; tandis que l'acide heptanoïque ne peut pas choisir de manière prévisible entre ces deux sites d'adsorption.

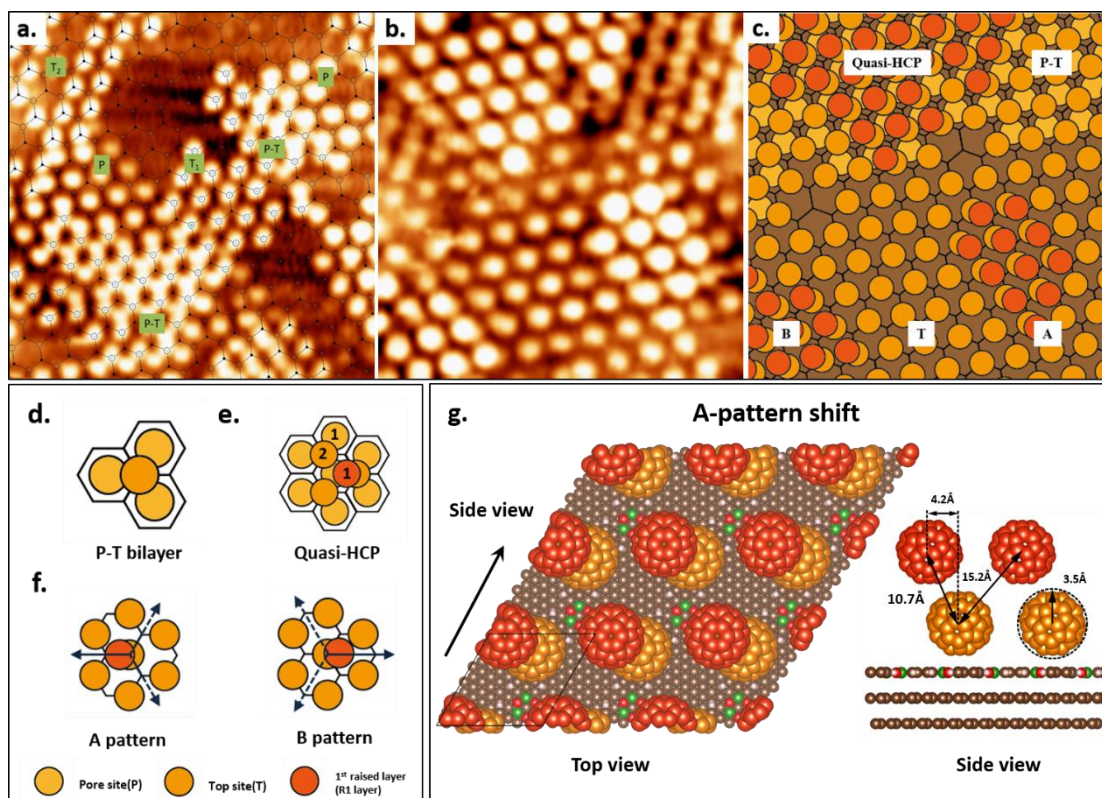


Figure 5 (a) Image STM avec structure bicouche P-T obtenue à l'interface acide heptanoïque/HOPG. Conditions de balayage: $V=-776$ mV, $I=42.25$ pA. Dimensions de

l'image: $19 \times 19 \text{ nm}^2$. (b) Image STM mesurée à l'interface acide heptanoïque/HOPG montrant la structure de la tricouche quasi-HCP et les décalages de la couche $R1_T$ dans les modèles A et B. Conditions de balayage: $V = -800 \text{ mV}$, $I = 33 \text{ pA}$. Dimensions de l'image: $15.4 \times 15.4 \text{ nm}^2$. (c) Représentation schématique correspondant à (b). Les différentes architectures sont marquées par des indicateurs. (d) Modèle de la bicouche P-T. (e) Modèle de la structure à tricouche quasi-HCP. Les deux molécules de fullerène marquées par "I" sont adsorbées dans la position quasi-identique. (f) Modèles du déplacement d'une seule molécule de couche $R1_T$ par rapport à la couche T dans les modèles A et B. (g) La structure calculée DFT du décalage A-pattern, comme montré dans la vue de dessus et la vue de côté. Les positions relatives du site T et de $R1_{C_{60}}$ sont spécifiées en vue de côté. Pour une meilleure visualisation, le rayon des atomes de carbone C_{60} est augmenté.

Des couches minces C_{60} des multicouches ont également été préparées par dépôt de la goutte à goutte de molécules de fullerène invités dans de l'acide heptanoïque sur du HOPG recouvert de COF-1 préparé au préalable. L'obtention des sites d'adsorption T et P simultanée peut se produire dans la même région par la formation d'une bicouche. Par exemple, nous observons une structure bicouche constituée de P-site C_{60} en combinaison avec un site T C_{60} , que nous nommons la bicouche P-T (*Figure 5a*), ce qui est en accord avec les petits domaines observés par Plas *et al.*¹²² Sur la *Figure 5a*, un maillage hexagonal représentant le treillis COF-1 est superposé à l'image STM. Les points brillants sont interprétés comme des molécules C_{60} . Deux réseaux

moléculaires C_{60} de site T, situés sur des anneaux de boroxine, peuvent être identifiés et représentés par des cercles (T_1) et des points (T_2). Ces réseaux coexistent avec les molécules C_{60} en site P, définissant la structure de la bicouche P-T (*Figure 5d*). L'énergie de cohésion de la bicouche P-T est de -2.36 eV, plus élevée que la somme (-2.12 eV) des énergies du site P et du site T (Tableau 1, DFT-D3). Lorsque à la fois le site P et le site T sont occupés, une stabilité supplémentaire est obtenue à partir de l'interaction entre les molécules de fullerène adjacentes. Cependant, l'existence de la structure P-T repose sur l'adsorption des C_{60} en site P, qui peut être influencé par le solvant utilisé.⁵⁶

Le substrat COF-1 peut héberger une variété de structures des multicouches. Une troisième couche, nommée en tant que la première couche surélevée (R_{1P-T}), peut être adsorbée au-dessus de la bicouche P-T pour former une structure à tricouches (image STM sur la *Figure 5b* et schéma sur la *Figure 5e*). Comme le montre la vue schématique, cette tricouche présente une structure quasi-hexagonale (quasi-HCP). Nous définissons cela comme une structure “quasi” -HCP en raison du décalage entre les première et troisième couches (voir la *Figure 5e*), qui diffère de la HCP dans laquelle les molécules des première et troisième couches sont positionnées en regard les unes avec les autres.

Une monocouche de couche T, sans molécules dans les sites P, peut également être la base d'une adsorption supplémentaire. Dans ce cas, la couche R_{1T} peut se décaler vers deux géométries distinctes par rapport à la couche T. Nous les nommons comme un

décalage de motif A et un décalage de motif B, dont chacun existe en symétrie triple par rapport à un fullerène de site T ordonné, comme le montre la *Figure 5f*. Nos calculations confirment cette observation et montrent que les déplacements A et B sont des structures stables avec l'énergie de liaison du fullerène $R1_T$ calculée comme $E_A = -0.21$ eV et $E_B = -0.25$ eV respectivement (Tableau 1). La structure optimisée par DFT du décalage vers le réseau A est présentée à la *Figure 5g*. Lorsque l'ensemble des domaines de fullerènes $R1_T$ se déplacent linéairement dans la même direction (diagramme A ou B), nous désignons cet assemblage collectif par un décalage parallèle. La couche $R1_{P-T}$ a également la même géométrie (*Figure 5b et c*). Par une combinaison de distances mesurées à partir d'images STM et de considérations géométriques, nous trouvons que la distance de décalage de la couche R1 par rapport au fullerène de la couche T donné est de 0.43 nm, ce qui correspond à la demi-longueur de l'hexagonal. Ceci est en accord avec notre résultat de calcul (0.42 nm). Cependant, l'observation de ces structures décalées va à l'encontre des principes de Kitaigorodskii,¹⁶⁶ puisque le site d'adsorption de la couche R1 n'est pas le centre de symétrie d'ordre trois de la couche T C_{60} . Cette dernière est la structure compacte définie par le substrat, et est celle qui est favorisée enthalpiquement, avec une énergie de liaison de -0.73 eV (Tableau 1).

L'analyse structurale ci-dessus suggère que les molécules $R1 C_{60}$, qui s'adsorbent dans les motifs décalés moins denses au lieu de la structure compacte définie par le substrat, conduisent à la formation de cette diversité de structures polymorphes. En utilisant

l'acide heptanoïque en tant que solvant, nous n'avons jamais observé la structure compacte définie par la matrice R1 (le site creux de symétrie trois présent dans la couche T), malgré à l'avantage thermodynamique qu'elle offre.

Tableau 1 L'adsorption et l'énergie cohésive totale de la croissance 2D à 3D de C₆₀ (1^{ère}, 2^{ème} et 3^{ème} couches de C₆₀ formées de 1, 2 et 3 couches moléculaires C₆₀, respectivement) sur COF-1/graphène bicouche

	Single layer			Bilayer					Triple layer				
	Porc-site (P-site)	Top-phenyl ring	Top-boroxine ring (T-site)	P-T bilayer	A-pattern shift	B-pattern shift	A-close packed	B-close packed	Shift-pattern without COF-1/graphène bilayer	A-FCC	A-HCP	B-FCC	B-HCP
R2 C ₆₀ [#]									-0.20 eV (-0.22 eV) [-0.01]**	-0.61 eV (-0.58 eV)	-0.59 eV (-0.57 eV)	-0.79 eV (-0.59 eV)	-0.60 eV (-0.63 eV)
R1 C ₆₀ [#]					-0.21 eV (-0.23 eV)	-0.25 eV (-0.25 eV)	-0.73 eV (-0.72 eV)	-0.54 eV (-0.57 eV)		-0.85 eV (-0.77 eV)	-0.85 eV (-0.77 eV)	-0.89 eV (-0.79 eV)	-0.89 eV (-0.79 eV)
1 st C ₆₀	-1.60 eV (-1.58 eV) [#]	-0.42 eV (-0.43 eV)	-0.64 eV (-0.54 eV)		-0.64 eV (-0.54 eV)	-0.64 eV (-0.54 eV)	-0.64 eV (-0.54 eV)	-0.64 eV (-0.54 eV)					
Total cohesive energy	-1.60 eV (-1.58 eV)	-0.42 eV (-0.43 eV)	-0.64 eV (-0.54 eV)	-2.36 eV	-0.85 eV (-0.77 eV)	-0.89 eV (-0.79 eV)	-1.37 eV (-1.28 eV)	-1.18 eV (-1.11 eV)		-1.46 eV (-1.35 eV)	-1.44 eV (-1.34 eV)	-1.68 eV (-1.38 eV)	-1.49 eV (-1.42 eV)

[#]The adsorption energy of R1 C₆₀ is reported with respect to top-boroxine ring structure.

^{##}The adsorption energy of R2 C₆₀ is reported with respect to A- and B-pattern shift structures.

*DFT-D3 (values in parentheses)

**DFT (without dispersion correction)

Tableau 2 La charge de Bader pour les structures de site et de décalage

Valence electrons (+ lost, - gained)	Free C ₆₀ , COF-1 and graphene bilayer	COF-1/graphene bilayer	Top-site	A-shift	B-shift
R1 layer C ₆₀	240.000			240.005 (-0.005)	240.004 (-0.004)
T-layer C ₆₀	240.000		239.948 (+0.052)	239.953 (+0.047)	239.948 (+0.052)
COF-1	138.000	138.102	138.146 (-0.044)	138.140 (-0.038)	138.155 (-0.053)
Graphene bilayer	576.000	575.898	575.906 (-0.008)	575.902 (-0.004)	575.893 (+0.005)

Tableau 3 Énergies totales de cohésion de la couche T C₆₀, des structures de décalage et des structures définies par le gabarit avec co-adsorption des molécules d'acide heptanoïque

dE (eV)	Top layer	A-shift	A-close packing	B-shift	B-close packing
Total cohesive energy*	-2.16 eV	-2.69 eV	-2.62 eV	-2.63 eV	-2.40 eV
Contribution of solvent co-adsorption in cohesive energy#	-1.69 eV	-1.93 eV	-1.38 eV	-1.85 eV	-1.31 eV

*dE(total)_{system+solvent}=E_{system+solvent}-(E_{COF-1/graphene bilayer}+E_{C60}+E_{solvent}); System=COF-1/graphene bilayer+ C₆₀

#dE(co-adsorption)=E_{system+solvent}-(E_{system}+E_{solvent})

Il y a deux effets principaux qui favorisent le déplacement de la couche R1, plutôt que la structuration sous forme compacte: l'effet électrostatique¹⁶⁸ ou l'effet de solvant.³⁵ Pour explorer les effets électrostatiques, nous avons effectué une analyse de charge de Bader des structures simulées par DFT. Ces calculs montrent que la charge transférée entre le site T et le décalage R1 C₆₀ est négligeable et que la distribution de charge du décalage R1 C₆₀ est essentiellement la même que celle d'un C₆₀ libre (voir le Tableau 2). Ceci est en accord avec les énergies calculées pour la liaison entre le déplacement R1 C₆₀ et le fullerène du site T correspondant, qui sont essentiellement identiques si le dimère de fullerène est calculé en présence ou en l'absence du substrat bicouche COF-1/graphène (~-0.2 eV, voir le Tableau 1). Ces résultats indiquent que les molécules de décalage R1 C₆₀ sont stabilisées par des interactions vdW avec le

fullerène du site T sous-jacent, excluant les effets électrostatiques anisotropes potentiellement provoqués par la présence du substrat.^{75, 169-170}

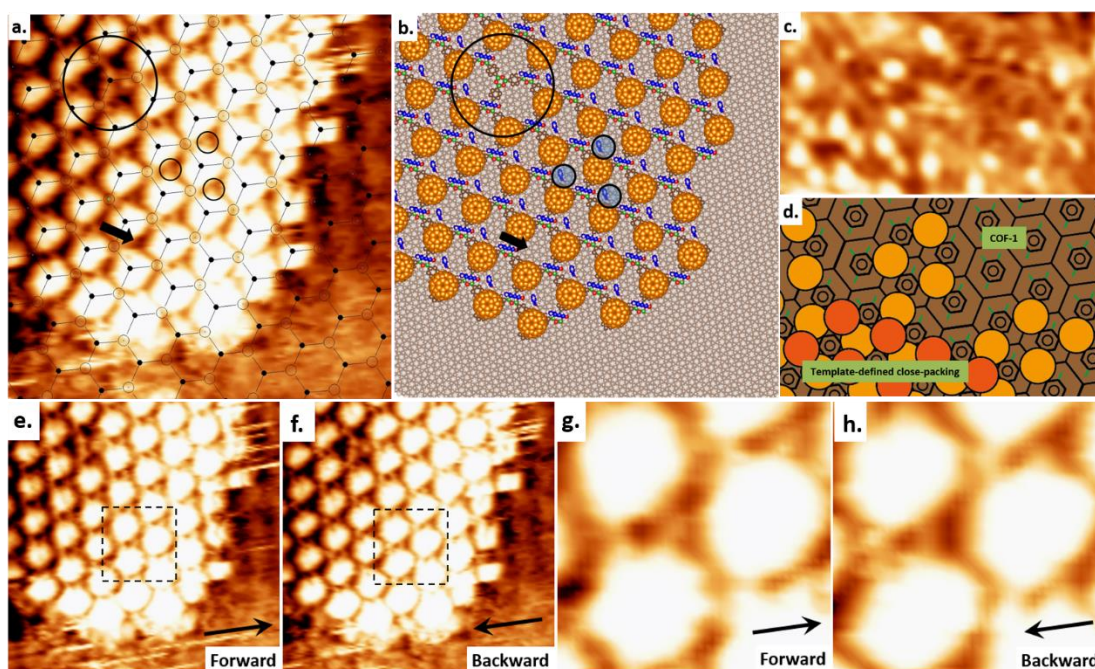


Figure 6 (a) Image STM montrant la co-adsorption de l'acide heptanoïque et de la couche T C_{60} recueillies à l'interface acide heptanoïque/HOPG. Conditions de scan: $V=-1000$ mV, $I=50$ pA. Dimensions de l'image: 12×12 nm². Le réseau hexagonal représente le substrat COF-1. Un seul C_{60} manquant est marqué par un grand cercle noir. Les structures situées en bas du site C_{60} manquant sont considérées comme étant le substrat COF-1. Trois petites tâches lumineuses sont attribuées aux molécules de solvant et sont marquées par de petits cercles noirs; une adsorption similaire se produit dans tout le réseau, mais n'a pas été indiquée pour permettre une visualisation plus claire de la modulation de contraste associée à ces structures. Un site sans cette petite structure lumineuse est marqué par une flèche noire. (b) Structure optimisée de la couche T C_{60} avec co-adsorption de l'acide heptanoïque à la fois au site P et au site T

(Tableau 3). Les molécules d'acide heptanoïque du site T apparaissent sur chacun des trois cycles boroxine dans la matrice COF-1. Un seul acide heptanoïque adsorbé sur le site P par pore apparaît, ce qui correspond à l'adsorption légèrement décentrée de la molécule C₆₀ du site T. Pour une meilleure illustration du modèle correspondant aux données expérimentales, le schéma (b) a été modifié à partir des données DFT réelles en retirant les structures manquantes de l'image STM (a). (c) Image STM collectée à l'interface surnageant (TCB)/HOPG. Dimensions de l'image: 9.6 × 5.4 nm². Conditions de balayage: V = -1000 mV, I = 50 pA. Ici, R1 C₆₀ s'adsorbe dans une géométrie compacte imposée par le substrat. (d) Schéma de (c) avec des molécules de TCB dans les pores de la matrice COF-1. Les images STM (e et f) montrent la co-adsorption de l'acide heptanoïque dans la couche T C₆₀ obtenue dans une même collection. (e) est l'image de balayage vers l'avant et (f) est l'image de balayage vers l'arrière. Conditions de balayage: V=-1000 mV, I=50 pA. Dimensions de l'image: 11.72 × 11.72 nm². (g, h) sont des images agrandies correspondant aux régions marquées par des carrés noirs en pointillés dans (e) et (f) respectivement. Dimensions de l'image: 2.8 × 2.8 nm². Les flèches noires dans les images indiquent la direction du balayage. (f) est également indiqué en (a).

Sur la Figure 6a, quelques points lumineux plus petits sont visibles dans la couche T. La taille de ces structures (~ 0.39 nm) est en accord avec les observations précédentes de l'acide heptanoïque (~ 0.35 nm),¹⁷¹ suggérant la possibilité d'une co-adsorption des molécules de solvant dans les espaces interstitiels. La position d'une petite structure

lumineuse à l'intérieur d'un pore est également influencée par la direction de balayage du STM. Dans le cas du balayage vers l'avant, le petit point lumineux s'est situé au centre de trois molécules C_{60} de site T (*Figure 6g*). Mais dans le balayage vers l'arrière, le petit point lumineux s'est situé asymétriquement dans l'un des trois coins équivalents (*Figure 6h*). Ainsi la position de ce petit point lumineux est associée à la direction du balayage de la pointe STM. Cette observation confirme notre hypothèse selon laquelle ces petites structures lumineuses sont des molécules d'acide heptanoïque orientées vers le haut et la flexibilité de la molécule d'acide heptanoïque permet d'expliquer les différentes positions observés pour les structures lumineuses, en fonction de la direction de balayage du STM.

Par conséquent, nous proposons que la formation de R1 C_{60} décalée peut être attribuée à la co-adsorption de l'acide heptanoïque dans les espaces vides entre les molécules C_{60} dans la couche T (*Figure 6b*).³⁵ Les molécules d'acide heptanoïque sont connues pour s'orienter avec leurs groupes carboxyle dirigés vers la surface et leurs chaînes alkyles pointant hors de la surface; les chaînes sont susceptibles d'être désordonnées.¹⁷¹ Les molécules d'acide heptanoïque peuvent également s'orienter avec leurs groupes carboxyle vers le haut, formant un dimère avec une autre molécule de solvant.¹⁷² Puisque la longueur de l'acide heptanoïque (~1.0 nm pour le monomère et 2.1 nm pour le dimère) est comparable au (plus grand) diamètre de C_{60} , les chaînes alkyles protubérantes empêcheraient l'adsorption du R1 C_{60} dans une structure compacte. Dans les images STM, l'arrangement des molécules de solvant alkylées

coadsorbées ne peut pas être clairement résolu en 2D généralement,^{159-160, 173} et encore moins dans notre cas de co-adsorption dans l'espace 3D. Ainsi, aucune conclusion ne peut être tirée sur l'arrangement d'adsorption ou la conformation précise des molécules de solvant dans les espaces créés par les molécules C₆₀. Cependant, même en l'absence d'une compréhension détaillée de la géométrie d'adsorption, les calculations DFT dans lesquels des molécules d'acide heptanoïque ont été ajoutées aux cellules unitaires des structures décalées suggèrent que la présence des molécules de solvant incorporées stabilise ces dernières (Tableau 3).

Pour tester l'hypothèse de coadsorption de solvant, nous avons effectué la même expérience en utilisant un solvant différent. Au lieu de l'acide heptanoïque, nous avons appliqué le surnageant de C₆₀ dans du TCB, un solvant aromatique planaire sans chaînes alkyle, à une monocouche de COF-1 préfabriquée. Sur la base de nos travaux antérieurs, nous nous attendons à ce que le TCB s'adsorbe au plat dans les pores COF-1.⁵⁶ En utilisant du TCB en tant que solvant, nous avons obtenu le motif de R1 C₆₀, contraint par le substrat, et favorable au niveau enthalpique, comme le montre la *Figure 6c*. Le modèle de Moiré formé par la rotation n'a pas été observé, indiquant l'absence de la structure de décalage R1. De plus, le film C₆₀ dans TCB est moins stable sous balayage de STM que les couches C₆₀ dans l'acide heptanoïque. En considérant uniquement l'énergie des fullerènes, cette observation est contre-intuitive, puisque le R1 C₆₀ dense défini par le substrat est plus stable que le R1 C₆₀ décalé (Tableau 1). Cependant, en tenant compte de la coadsorption des molécules de solvant,

cette observation est en accord avec la stabilité importante de la couche de fullerène grâce aux interactions avec les molécules d'acide heptanoïque pendantes (Tableau 3). Le TCB planaire à pores confinés ne peut pas interagir avec des couches surélevées et n'offre donc aucune stabilisation.

Nous suggérons que la co-adsorption des molécules de solvant est responsable du polymorphisme observé: l'acide heptanoïque co-adsorbé inhibe stériquement la formation de la structure fullerène compacte, qui est plutôt permise par les plus petites molécules planaires de solvant TCB. Sans la matrice COF-1, les molécules C₆₀ se cristallisent dans un cristal compact C₆₀ standard CFC (cubique à faces centrées) sur HOPG, plutôt que de former des phases pseudopolymorphiques incorporant de l'acide heptanoïque.^{165, 174-175}

Conclusions

COF-1 a été utilisé comme une hôte robuste pour les molécules invité fullerène C₆₀ à l'interface d'entre solution/solide et dans les conditions ambiantes. La couche de COF-1 a été synthétisée de manière routinière sur HOPG et les structures H/G peuvent être produites par l'introduction d'une solution de C₆₀ dans différents solvants et concentrations.

Les études de STM ont démontré la possibilité de former des architectures H/G à base de COF avec une épaisseur de la monocouche. A la fois à l'interface heptanoïque/HOPG et dans les couches séchées, COF-1 présente un réseau avec deux

sites distincts d'adsorption pour la molécule fullerène: un site de pore, où la molécule C_{60} est adsorbée sur le HOPG sous-jacent, et un site en haut, où le fullerène est adsorbé sur le cycle boroxine. Des couches de COF-1/fullerène séchés peuvent être produits soit par le dépôt de goutte à goutte, soit en trempant le COF-1 supporté par HOPG dans la solution de fullerène.

La méthode de synthèse de la couche de COF-1 poreuse sur HOPG à partir de la solution dans le TCB a également été développée. Les images de STM recueillies à l'interface de TCB/solide révèlent l'adsorption de TCB dans les pores hexagonaux de la matrice COF-1. Les calculs DFT suggèrent que cette structure de hôte/invité est stabilisée par une liaison d'hydrogène Cl...H. L'inclusion de C_{60} dans la solution TCB nous a permis d'étudier la reconnaissance moléculaire du modèle. Lorsque les deux C_{60} et TCB sont présents à l'interface de solution/solide, les molécules TCB sont sélectivement piégés dans les pores de la matrice COF-1, alors que les fullerènes adsorbent sur le COF-1 dans les sites identifiés comme sites supérieurs.

Le réseau COF-1 de monocouche s'est également avéré capable d'induire l'auto-assemblage du fullerène en structures multicouches à l'interface de solution/solide. L'assemblage contraint par le substrat diffère de l'assemblage ordinaire celui-ci dépend du solvant pour les molécules de fullerène: un motif compacte défini par le substrat obtenu en utilisant le TCB comme solvant, tandis que des polymorphes de densité plus faible sont observés lorsque l'on utilise l'acide heptanoïque comme solvant. Le polymorphisme et les morphologies dépendants du

solvant peuvent être décrits en termes d'effet de co-adsorption de solvant entraîné par un substrat. Les résultats présentés ici mettent en évidence le rôle important du solvant, non seulement pour influencer l'auto-assemblage 2D, mais aussi pour définir les architectures 3D. Grâce à une combinaison judicieuse de solvant et de matrice, des couches (pseudo) polymorphes peuvent être formés avec des géométries d'assemblage qui n'ont pas été observées dans d'autres conditions. Cela offre une voie prometteuse vers l'utilisation de la combinaison de la matrice 2D et des effets de solvant pour contrôler l'auto-assemblage moléculaire avec précision dans la troisième dimension, même en l'absence d'interactions directionnelles soluté-soluté ou soluté-solvant.

Dans cette thèse, le piégeage prévisible de molécules de fullerène utilisant COF-1 a été montré comme un exemple de preuve de principe de l'utilité des COF à base d'acide boronique 2D pour des applications dans la détection ou le piégeage de molécules cibles dans lesquelles le COF est exposé. L'adsorption sélective de TCB et C₆₀ dans COF-1 suggère que les différents sites d'adsorption dans le réseau COF-1 peuvent être utilisés pour séparer les molécules invitées par différentes interactions, ouvrant des opportunités pour des applications dans la structuration moléculaire et la reconnaissance. La combinaison de deux paramètres de réglage indépendants, le substrat COF-1 et le solvant, suggère un meilleur contrôle des différentes phases, ce qui pourrait donner lieu à des phases non-observées auparavant dans une gamme de matériaux avancés apparentés.²⁰⁴

References

1. Feynman, R. P., There's plenty of room at the bottom. *Engineering and science* **1960**, *23* (5), 22-36.
2. Cao, G., Nanostructures and nanomaterials: synthesis, properties and applications. *Imperial College: London* **2004**; p 110.
3. Whitesides, G. M.; Kriebel, J. K.; Mayers, B. T., Self-assembly and nanostructured materials. In *Nanoscale Assembly, Springer: New York* **2005**; p 217-239.
4. Alivisatos, A. P., Semiconductor clusters, nanocrystals, and quantum dots. *Science* **1996**, *271* (5251), 933-937.
5. Barth, J. V.; Costantini, G.; Kern, K., Engineering atomic and molecular nanostructures at surfaces. *Nature* **2005**, *437* (7059), 671-679.
6. Gates, B. D.; Xu, Q.; Stewart, M.; Ryan, D.; Willson, C. G.; Whitesides, G. M., New approaches to nanofabrication: molding, printing, and other techniques. *Chem. Rev.* **2005**, *105* (4), 1171-1196.
7. Broers, A.; Hoole, A.; Ryan, J., Electron beam lithography—Resolution limits. *Microelectron. Eng.* **1996**, *32* (1), 131-142.
8. Schulz, M., The end of the road for silicon? *Nature* **1999**, *399* (6738), 729-730.
9. Lu, W.; Lieber, C. M., Nanoelectronics from the bottom up. *Nat. Mater.* **2007**, *6* (11), 841-850.
10. Ariga, K.; Hill, J. P.; Lee, M. V.; Vinu, A.; Charvet, R.; Acharya, S., Challenges and breakthroughs in recent research on self-assembly. *Sci. Technol. Adv. Mat.* **2008**, *9* (1), 014109.
11. Whitesides, G. M.; Grzybowski, B., Self-assembly at all scales. *Science* **2002**, *295* (5564), 2418-2421.
12. Otero, R.; Gallego, J. M.; de Parga, A. L. V.; Martín, N.; Miranda, R., Molecular Self-Assembly at Solid Surfaces. *Adv. Mater.* **2011**, *23* (44), 5148-5176.
13. Sun, J.; Lu, Y.; Chen, W.; Feng, Y.; Wee, A., Linear tuning of charge carriers in graphene by organic molecules and charge-transfer complexes. *Phys. Rev. B* **2010**, *81* (15), 155403.
14. Tseng, T.-C.; Urban, C.; Wang, Y.; Otero, R.; Tait, S. L.; Alcamí, M.; Écija, D.; Trelka, M.; Gallego, J. M.; Lin, N., Charge-transfer-induced structural rearrangements at both sides of organic/metal interfaces. *Nat. Chem.* **2010**, *2* (5), 374-379.
15. Plass, K. E.; Grzesiak, A. L.; Matzger, A. J., Molecular packing and symmetry of two-dimensional crystals. *Accounts Chem. Res.* **2007**, *40* (4), 287-293.
16. Ahn, S.; Matzger, A. J., Six different assemblies from one building block: Two-dimensional crystallization of an amide amphiphile. *J. Am. Chem. Soc.* **2010**, *132* (32), 11364-11371.
17. De Feyter, S.; De Schryver, F. C., Two-dimensional supramolecular self-assembly probed by scanning tunneling microscopy. *Chem. Soc. Rev.* **2003**, *32* (3), 139-150.
18. De Feyter, S.; De Schryver, F. C., Self-assembly at the liquid/solid interface: STM reveals. *J. Phys. Chem. B* **2005**, *109*, 4290-4302.
19. Li, J.; Gottardi, S.; Soliany, L.; Moreno López, J. C.; Stöhr, M., 1, 3, 5-Benzenetribenzoic Acid on Cu (111) and Graphene/Cu (111): A Comparative STM Study. *J. Phys. Chem. C* **2016**, *120*, 18093-18098.

20. Macleod, J. M.; Lipton-Duffin, J.; Cui, D.; De Feyter, S.; Rosei, F., Substrate effects in the supramolecular assembly of 1, 3, 5-benzene tricarboxylic acid on graphite and graphene. *Langmuir* **2015**, *31* (25), 7016–7024.
21. Lu, J.; Yeo, P. S. E.; Zheng, Y.; Yang, Z.; Bao, Q.; Gan, C. K.; Loh, K. P., Using the graphene moiré pattern for the trapping of C₆₀ and homoepitaxy of graphene. *ACS Nano* **2011**, *6* (1), 944-950.
22. Teyssandier, J.; De Feyter, S.; Mali, K. S., Host–guest chemistry in two-dimensional supramolecular networks. *Chem. Commun.* **2016**, *52* (77), 11465-11487.
23. Rochford, L. A.; Jones, T. S.; Nielsen, C. B., Epitaxial Templating of C₆₀ with a Molecular Monolayer. *J. Phys. Chem. Lett.* **2016**, *7* (17), 3487-3490.
24. Faul, C. F.; Antonietti, M., Ionic self-assembly: Facile synthesis of supramolecular materials. *Adv. Mater.* **2003**, *15* (9), 673-683.
25. MacLeod, J.; Ivashenko, O.; Perepichka, D.; Rosei, F., Stabilization of exotic minority phases in a multicomponent self-assembled molecular network. *Nanotechnology* **2007**, *18* (42), 424031.
26. Blunt, M. O.; Adisoejoso, J.; Tahara, K.; Katayama, K.; Van der Auweraer, M.; Tobe, Y.; De Feyter, S., Temperature-induced structural phase transitions in a two-dimensional self-assembled network. *J. Am. Chem. Soc.* **2013**, *135* (32), 12068-12075.
27. Gutzler, R.; Fu, C.; Dadvand, A.; Hua, Y.; MacLeod, J. M.; Rosei, F.; Perepichka, D. F., Halogen bonds in 2D supramolecular self-assembly of organic semiconductors. *Nanoscale* **2012**, *4* (19), 5965-5971.
28. Sirtl, T.; Schlögl, S.; Rastgoo-Lahrood, A.; Jelic, J.; Neogi, S.; Schmittel, M.; Heckl, W. M.; Reuter, K.; Lackinger, M., Control of intermolecular bonds by deposition rates at room temperature: hydrogen bonds versus metal coordination in trinitrile monolayers. *J. Am. Chem. Soc.* **2013**, *135* (2), 691-695.
29. Diercks, C. S.; Yaghi, O. M., The atom, the molecule, and the covalent organic framework. *Science* **2017**, *355* (6328), eaal1585.
30. Perepichka, D. F.; Rosei, F., Extending polymer conjugation into the second dimension. *Science* **2009**, *323* (5911), 216-217.
31. Si, S. K.; Gewirth, A. A., Solvent organization above metal surfaces: Ordering of DMSO on Au. *J. Phys. Chem. B* **2000**, *104* (46), 10775-10782.
32. Hibino, M.; Sumi, A.; Hatta, I., Atomic images of saturated and unsaturated fatty acids at liquid/graphite interface and difference of tunneling currents between them observed by scanning tunneling microscopy. *Jpn. J. Appl. Phys.* **1995**, *34*, 610.
33. Vanoppen, P.; Grim, P.; Rücker, M.; De Feyter, S.; Moessner, G.; Valiyaveetil, S.; Müllen, K.; De Schryver, F., Solvent Codeposition and Cis– Trans Isomerization of Isophthalic Acid Derivatives Studied by STM. *J. Phys. Chem.* **1996**, *100* (50), 19636-19641.
34. Mazur, U.; Hipps, K., Kinetic and thermodynamic processes of organic species at the solution–solid interface: the view through an STM. *Chem. Commun.* **2015**, *51* (23), 4737-4749.
35. Yang, Y.; Wang, C., Solvent effects on two-dimensional molecular self-assemblies investigated by using scanning tunneling microscopy. *Curr. Opin. Colloid In.* **2009**, *14* (2), 135-147.
36. Griessl, S.; Lackinger, M.; Edelwirth, M.; Hietschold, M.; Heckl, W. M., Self-assembled two-dimensional molecular host-guest architectures from trimesic acid. *Single Mol.* **2002**, *3* (1), 25-31.

37. Kampschulte, L.; Lackinger, M.; Maier, A.-K.; Kishore, R. S.; Griessl, S.; Schmittel, M.; Heckl, W. M., Solvent induced polymorphism in supramolecular 1, 3, 5-benzenetribenzoic acid monolayers. *J. Phys. Chem. B* **2006**, *110* (22), 10829-10836.
38. Lackinger, M.; Griessl, S.; Heckl, W. M.; Hietschold, M.; Flynn, G. W., Self-assembly of trimesic acid at the liquid– solid interface a study of solvent-induced polymorphism. *Langmuir* **2005**, *21* (11), 4984-4988.
39. Cote, A. P.; Benin, A. I.; Ockwig, N. W.; O’Keeffe, M.; Matzger, A. J.; Yaghi, O. M., Porous, crystalline, covalent organic frameworks. *Science* **2005**, *310* (5751), 1166-1170.
40. Lipton-Duffin, J.; Ivasenko, O.; Perepichka, D.; Rosei, F., Synthesis of polyphenylene molecular wires by surface-confined polymerization. *Small* **2009**, *5* (5), 592-597.
41. Weigelt, S.; Busse, C.; Bombis, C.; Knudsen, M. M.; Gothelf, K. V.; Lægsgaard, E.; Besenbacher, F.; Linderoth, T. R., Surface synthesis of 2D branched polymer nanostructures. *Angew. Chem. Int. Edit.* **2008**, *47* (23), 4406-4410.
42. Liu, X. H.; Guan, C. Z.; Wang, D.; Wan, L. J., Graphene-Like Single-Layered Covalent Organic Frameworks: Synthesis Strategies and Application Prospects. *Adv. Mater.* **2014**, *26* (40), 6912-6920.
43. Zwaneveld, N. A.; Pawlak, R.; Abel, M.; Catalin, D.; Gimes, D.; Bertin, D.; Porte, L., Organized formation of 2D extended covalent organic frameworks at surfaces. *J. Am. Chem. Soc.* **2008**, *130* (21), 6678-6679.
44. Korich, A. L.; Iovine, P. M., Boroxine chemistry and applications: A perspective. *Dalton T.* **2010**, *39* (6), 1423-1431.
45. Clair, S.; Ourdjini, O.; Abel, M.; Porte, L., Tip-or electron beam-induced surface polymerization. *Chem. Commun.* **2011**, *47* (28), 8028-8030.
46. Ourdjini, O.; Pawlak, R.; Abel, M.; Clair, S.; Chen, L.; Bergeon, N.; Sassi, M.; Oison, V.; Debierre, J.-M.; Coratger, R., Substrate-mediated ordering and defect analysis of a surface covalent organic framework. *Phys. Rev. B* **2011**, *84* (12), 125421.
47. Sassi, M.; Oison, V.; Debierre, J. M.; Humbel, S., Modelling the Two-Dimensional Polymerization of 1, 4-Benzene Diboronic Acid on a Ag Surface. *ChemPhysChem* **2009**, *10* (14), 2480-2485.
48. Guan, C.-Z.; Wang, D.; Wan, L.-J., Construction and repair of highly ordered 2D covalent networks by chemical equilibrium regulation. *Chem. Commun.* **2012**, *48* (24), 2943-2945.
49. Dienstmaier, J. r. F.; Gigler, A. M.; Goetz, A. J.; Knochel, P.; Bein, T.; Lyapin, A.; Reichlmaier, S.; Heckl, W. M.; Lackinger, M., Synthesis of well-ordered COF monolayers: Surface growth of nanocrystalline precursors versus direct on-surface polycondensation. *ACS Nano* **2011**, *5* (12), 9737-9745.
50. Dienstmaier, J. r. F.; Medina, D. D.; Dogru, M.; Knochel, P.; Bein, T.; Heckl, W. M.; Lackinger, M., Isorecticular two-dimensional covalent organic frameworks synthesized by on-surface condensation of diboronic acids. *ACS Nano* **2012**, *6* (8), 7234-7242.
51. Colson, J. W.; Dichtel, W. R., Rationally synthesized two-dimensional polymers. *Nat. Chem.* **2013**, *5* (6), 453-465.
52. Spitzer, S.; Rastgoo-Lahrood, A.; Macknapp, K.; Ritter, V.; Sotier, S.; Heckl, W. M.; Lackinger, M., Solvent-free on-surface synthesis of boroxine COF monolayers. *Chem. Commun.* **2017**, *53*, 5147-5150.

53. Davis, M. E., Ordered porous materials for emerging applications. *Nature* **2002**, *417* (6891), 813-821.
54. Mena-Osteritz, E.; Bäuerle, P., Complexation of C₆₀ on a cyclothiophene monolayer template. *Adv. Mater.* **2006**, *18* (4), 447-451.
55. Griessl, S. J.; Lackinger, M.; Jamitzky, F.; Markert, T.; Hietschold, M.; Heckl, W. M., Room-temperature scanning tunneling microscopy manipulation of single C₆₀ molecules at the liquid-solid interface: playing nanosoccer. *J. Phys. Chem. B* **2004**, *108* (31), 11556-11560.
56. Cui, D.; MacLeod, J.; Ebrahimi, M.; Rosei, F., Selective binding in different adsorption sites of a 2D covalent organic framework. *CrystEngComm* **2017**, *19*, 4927-4932.
57. Pan, G.-B.; Cheng, X.-H.; Höger, S.; Freyland, W., 2D supramolecular structures of a shape-persistent macrocycle and co-deposition with fullerene on HOPG. *J. Am. Chem. Soc.* **2006**, *128* (13), 4218-4219.
58. Rosei, F.; Schunack, M.; Naitoh, Y.; Jiang, P.; Gourdon, A.; Laegsgaard, E.; Stensgaard, I.; Joachim, C.; Besenbacher, F., Properties of large organic molecules on metal surfaces. *Prog. Sur. Sci.* **2003**, *71* (5), 95-146.
59. Griessl, S. J.; Lackinger, M.; Jamitzky, F.; Markert, T.; Hietschold, M.; Heckl, W. M., Incorporation and manipulation of coronene in an organic template structure. *Langmuir* **2004**, *20* (21), 9403-9407.
60. Li, M.; Deng, K.; Lei, S. B.; Yang, Y. L.; Wang, T. S.; Shen, Y. T.; Wang, C. R.; Zeng, Q. D.; Wang, C., Site-Selective Fabrication of Two-Dimensional Fullerene Arrays by Using a Supramolecular Template at the Liquid-Solid Interface. *Angew. Chem. Ger. Edit.* **2008**, *120* (35), 6819-6823.
61. Tahara, K.; Nakatani, K.; Iritani, K.; De Feyter, S.; Tobe, Y., Periodic Functionalization of Surface-Confined Pores in a Two-Dimensional Porous Network Using a Tailored Molecular Building Block. *ACS Nano* **2016**, *10* (2), 2113-2120.
62. Adisoejoso, J.; Tahara, K.; Okuhata, S.; Lei, S.; Tobe, Y.; De Feyter, S., Two-Dimensional Crystal Engineering: A Four-Component Architecture at a Liquid-Solid Interface. *Angew. Chem. Ger. Edit.* **2009**, *121* (40), 7489-7493.
63. Shen, Y.-T.; Li, M.; Guo, Y.-Y.; Deng, K.; Zeng, Q.-D.; Wang, C., The site-selective molecular recognition of ternary architectures by using supramolecular nanoporous networks at a liquid-solid interface. *Chem.-Asian J.* **2010**, *5* (4), 787.
64. Ghijssens, E.; Cao, H.; Noguchi, A.; Ivasenko, O.; Fang, Y.; Tahara, K.; Tobe, Y.; De Feyter, S., Towards enantioselective adsorption in surface-confined nanoporous systems. *Chem. Commun.* **2015**, *51* (23), 4766-4769.
65. Tahara, K.; Katayama, K.; Blunt, M. O.; Iritani, K.; De Feyter, S.; Tobe, Y., Functionalized surface-confined pores: guest binding directed by lateral noncovalent interactions at the solid-liquid interface. *ACS Nano* **2014**, *8* (8), 8683-8694.
66. Bonifazi, D.; Mohnani, S.; Llanes-Pallas, A., Supramolecular chemistry at interfaces: molecular recognition on nanopatterned porous surfaces. *Chem.-Eur. J.* **2009**, *15* (29), 7004-7025.
67. Iritani, K.; Tahara, K.; De Feyter, S.; Tobe, Y., Host-Guest Chemistry in Integrated Porous Space Formed by Molecular Self-Assembly at Liquid-Solid Interfaces. *Langmuir* **2017**, *33* (19), 4601-4618.

68. Pfeiffer, C. R.; Pearce, N.; Champness, N. R., Complexity of Two-Dimensional Self-Assembled Arrays at Surfaces. *Chem. Commun.* **2017**, 53, 11528-11539.
69. Lei, S.; Surin, M.; Tahara, K.; Adisoejoso, J.; Lazzaroni, R.; Tobe, Y.; Feyter, S. D., Programmable Hierarchical Three-Component 2D Assembly at a Liquid– Solid Interface: Recognition, Selection, and Transformation. *Nano Lett.* **2008**, 8 (8), 2541-2546.
70. Yeung, M. C.-L.; Yam, V. W.-W., Luminescent cation sensors: from host–guest chemistry, supramolecular chemistry to reaction-based mechanisms. *Chem. Soc. Rev.* **2015**, 44, 4192-4202.
71. Zhu, C.; Fang, L., Mingling Electronic Chemical Sensors with Supramolecular Host-Guest Chemistry. *Curr. Org. Chem.* **2014**, 18 (15), 1957-1964.
72. Huang, J.; Sun, J.; Katz, H. E., Monolayer-Dimensional 5, 5'-Bis (4-hexylphenyl)-2, 2'-bithiophene Transistors and Chemically Responsive Heterostructures. *Adv. Mater.* **2008**, 20 (13), 2567-2572.
73. Ciesielski, A.; Cadeddu, A.; Palma, C.-A.; Gorczyński, A.; Patroniak, V.; Cecchini, M.; Samorì, P., Self-templating 2D supramolecular networks: a new avenue to reach control over a bilayer formation. *Nanoscale* **2011**, 3 (10), 4125-4129.
74. Ivasenko, O.; MacLeod, J. M.; Chernichenko, K. Y.; Balenkova, E. S.; Shpanchenko, R. V.; Nenajdenko, V. G.; Rosei, F.; Perepichka, D. F., Supramolecular assembly of heterocirculenes in 2D and 3D. *Chem. Commun.* **2009**, (10), 1192-1194.
75. Yoshimoto, S.; Tsutsumi, E.; Narita, R.; Murata, Y.; Murata, M.; Fujiwara, K.; Komatsu, K.; Ito, O.; Itaya, K., Epitaxial supramolecular assembly of fullerenes formed by using a coronene template on a Au (111) surface in solution. *J. Am. Chem. Soc.* **2007**, 129 (14), 4366-4376.
76. Theobald, J. A.; Oxtoby, N. S.; Phillips, M. A.; Champness, N. R.; Beton, P. H., Controlling molecular deposition and layer structure with supramolecular surface assemblies. *Nature* **2003**, 424 (6952), 1029-1031.
77. Wei, Y.; Reutt-Robey, J. E., Directed Organization of C₇₀ Kagome Lattice by Titanyl Phthalocyanine Monolayer Template. *J. Am. Chem. Soc.* **2011**, 133 (39), 15232-15235.
78. González, J. D. C.; Iyoda, M.; Rabe, J. P., Templated bilayer self-assembly of fully conjugated π -expanded macrocyclic oligothiophenes complexed with fullerenes. *Nat. Commun.* **2017**, 8, 14717.
79. Blunt, M. O.; Russell, J. C.; del Carmen Gimenez-Lopez, M.; Taleb, N.; Lin, X.; Schröder, M.; Champness, N. R.; Beton, P. H., Guest-induced growth of a surface-based supramolecular bilayer. *Nat. Chem.* **2011**, 3 (1), 74-78.
80. Cui, D.; MacLeod, J.; Ebrahimi, M.; Perepichka, D.; Rosei, F., Solution and air stable host/guest architectures from a single layer covalent organic framework. *Chem. Commun.* **2015**, 51 (92), 16510-16513.
81. den Boer, D.; Han, G. D.; Swager, T. M., Templating Fullerenes by Domain Boundaries of a Nanoporous Network. *Langmuir* **2014**, 30 (3), 762-767.
82. Blunt, M. O.; Russell, J. C.; Champness, N. R.; Beton, P. H., Templating molecular adsorption using a covalent organic framework. *Chem. Commun.* **2010**, 46 (38), 7157-7159.
83. MacLeod, J. M.; Ivasenko, O.; Fu, C.; Taerum, T.; Rosei, F.; Perepichka, D. F., Supramolecular Ordering in Oligothiophene– Fullerene Monolayers. *J. Am. Chem. Soc.* **2009**, 131 (46), 16844-16850.

84. Kroto, H. W.; Heath, J. R.; O'Brien, S. C.; Curl, R. F.; Smalley, R. E., C₆₀: Buckminsterfullerene. *Nature* **1985**, *318* (6042), 162-163.
85. Prato, M., [60] Fullerene chemistry for materials science applications. *J. Mater. Chem.* **1997**, *7* (7), 1097-1109.
86. Itaka, K.; Yamashiro, M.; Yamaguchi, J.; Haemori, M.; Yaginuma, S.; Matsumoto, Y.; Kondo, M.; Koinuma, H., High-Mobility C₆₀ Field-Effect Transistors Fabricated on Molecular-Wetting Controlled Substrates. *Adv. Mater.* **2006**, *18* (13), 1713-1716.
87. Sullivan, P.; Jones, T. S.; Ferguson, A.; Heutz, S., Structural templating as a route to improved photovoltaic performance in copper phthalocyanine/fullerene (C₆₀) heterojunctions. *Appl. Phys. Lett.* **2007**, *91* (23), 233114.
88. Binnig, G.; Rohrer, H.; Gerber, C.; Weibel, E., 7 × 7 reconstruction on Si (111) resolved in real space. *Phys. Rev. Lett.* **1983**, *50* (2), 120.
89. Binnig, G.; Rohrer, H., Scanning tunneling microscopy—from birth to adolescence. *Rev. Mod. Phys.* **1987**, *59* (3), 615.
90. Chen, C. J., Introduction to scanning tunneling microscopy. *Oxford University Press on Demand: New York*, **1993**; Vol. 4.
91. Bardeen, J., Tunnelling from a many-particle point of view. *Phys. Rev. Lett.* **1961**, *6* (2), 57.
92. Ding, S.-Y.; Wang, W., Covalent organic frameworks (COFs): from design to applications. *Chem. Soc. Rev.* **2013**, *42* (2), 548-568.
93. Zou, X.; Ren, H.; Zhu, G., Topology-directed design of porous organic frameworks and their advanced applications. *Chem. Commun.* **2013**, *49* (38), 3925-3936.
94. Tilford, R. W.; Mugavero, S. J.; Pellechia, P. J.; Lavigne, J. J., Tailoring Microporosity in Covalent Organic Frameworks. *Adv. Mater.* **2008**, *20* (14), 2741-2746.
95. Yu, J.-T.; Chen, Z.; Sun, J.; Huang, Z.-T.; Zheng, Q.-Y., Cyclotricatechylene based porous crystalline material: Synthesis and applications in gas storage. *J. Mater. Chem.* **2012**, *22* (12), 5369-5373.
96. Furukawa, H.; Yaghi, O. M., Storage of Hydrogen, Methane, and Carbon Dioxide in Highly Porous Covalent Organic Frameworks for Clean Energy Applications. *J. Am. Chem. Soc.* **2009**, *131* (25), 8875-8883.
97. Han, S. S.; Furukawa, H.; Yaghi, O. M.; Goddard III, W. A., Covalent organic frameworks as exceptional hydrogen storage materials. *J. Am. Chem. Soc.* **2008**, *130* (35), 11580-11581.
98. Wan, S.; Guo, J.; Kim, J.; Ihee, H.; Jiang, D., A Photoconductive Covalent Organic Framework: Self-Condensed Arene Cubes Composed of Eclipsed 2D Polypyrene Sheets for Photocurrent Generation. *Angew. Chem. Int. Edit.* **2009**, *48* (30), 5439-5442.
99. Ding, X.; Chen, L.; Honsho, Y.; Feng, X.; Saengsawang, O.; Guo, J.; Saeki, A.; Seki, S.; Irle, S.; Nagase, S.; Parasuk, V.; Jiang, D., An n-Channel Two-Dimensional Covalent Organic Framework. *J. Am. Chem. Soc.* **2011**, *133* (37), 14510-14513.
100. Chen, L.; Furukawa, K.; Gao, J.; Nagai, A.; Nakamura, T.; Dong, Y.; Jiang, D., Photoelectric Covalent Organic Frameworks: Converting Open Lattices into Ordered Donor–Acceptor Heterojunctions. *J. Am. Chem. Soc.* **2014**, *136* (28), 9806-9809.

101. Dogru, M.; Handloser, M.; Auras, F.; Kunz, T.; Medina, D.; Hartschuh, A.; Knochel, P.; Bein, T., A Photoconductive Thienothiophene-Based Covalent Organic Framework Showing Charge Transfer Towards Included Fullerene. *Angew. Chem. Ger. Edit.* **2013**, *125* (10), 2992-2996.
102. Koo, B. T.; Clancy, P., Towards optimal packing and diffusion of fullerene molecules in the Pc-PBBA covalent organic framework. *Mol. Simulat.* **2014**, *40* (1-3), 58-70.
103. Koo, B. T.; Berard, P. G.; Clancy, P., A Kinetic Monte Carlo Study of Fullerene Adsorption within a Pc-PBBA Covalent Organic Framework and Implications for Electron Transport. *J. Chem. Theory Comput.* **2015**, *11* (3), 1172-1180.
104. Lukose, B.; Kuc, A.; Heine, T., The Structure of Layered Covalent-Organic Frameworks. *Chem.–Eur. J.* **2011**, *17* (8), 2388-2392.
105. Novoselov, K. S.; Geim, A. K.; Morozov, S.; Jiang, D.; Zhang, Y.; Dubonos, S. a.; Grigorieva, I.; Firsov, A., Electric field effect in atomically thin carbon films. *Science* **2004**, *306* (5696), 666-669.
106. Perepichka, D. F.; Rosei, F., Chemistry. Extending polymer conjugation into the second dimension. *Science (New York, NY)* **2009**, *323* (5911), 216-217.
107. Berlanga, I.; Ruiz-González, M. L.; González-Calbet, J. M.; Fierro, J. L. G.; Mas-Ballesté, R.; Zamora, F., Delamination of Layered Covalent Organic Frameworks. *Small* **2011**, *7* (9), 1207-1211.
108. Berlanga, I.; Mas-Ballesté, R.; Zamora, F., Tuning delamination of layered covalent organic frameworks through structural design. *Chem. Commun.* **2012**, *48* (64), 7976-7978.
109. Chandra, S.; Kandambeth, S.; Biswal, B. P.; Lukose, B.; Kunjir, S. M.; Chaudhary, M.; Babarao, R.; Heine, T.; Banerjee, R., Chemically Stable Multilayered Covalent Organic Nanosheets from Covalent Organic Frameworks via Mechanical Delamination. *J. Am. Chem. Soc.* **2013**, *135* (47), 17853-17861.
110. Colson, J. W.; Dichtel, W. R., Rationally synthesized two-dimensional polymers. *Nat. Chem.* **2013**, *5* (6), 453-465.
111. Cai, S.-L.; Zhang, W.-G.; Zuckermann, R. N.; Li, Z.-T.; Zhao, X.; Liu, Y., The Organic Flatland—Recent Advances in Synthetic 2D Organic Layers. *Adv. Mater.* **2015**, *27*, 5762-5770.
112. Liu, X.-H.; Guan, C.-Z.; Ding, S.-Y.; Wang, W.; Yan, H.-J.; Wang, D.; Wan, L.-J., On-surface synthesis of single-layered two-dimensional covalent organic frameworks via solid–vapor interface reactions. *J. Am. Chem. Soc.* **2013**, *135* (28), 10470-10474.
113. Clair, S.; Abel, M.; Porte, L., Growth of boronic acid based two-dimensional covalent networks on a metal surface in ultrahigh vacuum. *Chem. Commun.* **2014**, *50*, 9627 -- 9635.
114. Cote, A. P.; El-Kaderi, H. M.; Furukawa, H.; Hunt, J. R.; Yaghi, O. M., Reticular synthesis of microporous and mesoporous 2D covalent organic frameworks. *J. Am. Chem. Soc.* **2007**, *129* (43), 12914-12915.
115. Spillmann, H.; Kiebele, A.; Stöhr, M.; Jung, T. A.; Bonifazi, D.; Cheng, F.; Diederich, F., A Two-Dimensional Porphyrin-Based Porous Network Featuring Communicating Cavities for the Templated Complexation of Fullerenes. *Adv. Mater.* **2006**, *18* (3), 275-279.
116. Stepanow, S.; Lingenfelder, M.; Dmitriev, A.; Spillmann, H.; Delvigne, E.; Lin, N.; Deng, X.; Cai, C.; Barth, J. V.; Kern, K., Steering molecular organization and host–guest interactions using two-dimensional nanoporous coordination systems. *Nat. Mater.* **2004**, *3* (4), 229-233.
117. Gutzler, R.; Sirtl, T.; Dienstmaier, J. r. F.; Mahata, K.; Heckl, W. M.; Schmittel, M.; Lackinger, M., Reversible Phase Transitions in Self-Assembled Monolayers at the Liquid– Solid Interface:

- Temperature-Controlled Opening and Closing of Nanopores. *J. Am. Chem. Soc.* **2010**, *132* (14), 5084-5090.
118. Semenov, K.; Charykov, N.; Pyartman, A.; Keskinov, V.; Lishchuk, V.; Arapov, O.; Alekseev, N., Solubility of fullerenes in n-alkanoic acids C₂–C₉. *J. Appl. Chem.* **2007**, *80* (3), 456-460.
119. Horcas, I.; Fernández, R.; Gomez-Rodriguez, J.; Colchero, J.; Gómez-Herrero, J.; Baro, A., WSXM: a software for scanning probe microscopy and a tool for nanotechnology. *Rev. Sci. Instrum.* **2007**, *78* (1), 013705.
120. Cicoira, F.; Santato, C.; Rosei, F., Two-dimensional nanotemplates as surface cues for the controlled assembly of organic molecules. *Top. Curr. Chem.* **2008**, *285*, 203-267.
121. Lei, S.; Tahara, K.; Feng, X.; Furukawa, S.; De Schryver, F. C.; Müllen, K.; Tobe, Y.; De Feyter, S., Molecular clusters in two-dimensional surface-confined nanoporous molecular networks: Structure, rigidity, and dynamics. *J. Am. Chem. Soc.* **2008**, *130* (22), 7119-7129.
122. Plas, J.; Ivasenko, O.; Martsinovich, N.; Lackinger, M.; De Feyter, S., Nanopatterning of a covalent organic framework host–guest system. *Chem. Commun.* **2016**, *52* (1), 68-71.
123. Sun, J.; Zhou, X.; Lei, S., Host–guest architectures with a surface confined imine covalent organic framework as two-dimensional host networks. *Chem. Commun.* **2016**, *52* (56), 8691-8694.
124. Bonifazi, D.; Mohnani, S.; Llanes-Pallas, A., Supramolecular chemistry at interfaces: molecular recognition on nanopatterned porous surfaces. *Chem.–Eur. J.* **2009**, *15* (29), 7004-7025.
125. Li, M.; Zeng, Q.; Wang, C., Self-assembled supramolecular networks at interfaces: Molecular immobilization and recognition using nanoporous templates. *China Phys. Chem.* **2011**, *54* (10), 1739-1748.
126. Tahara, K.; Katayama, K.; Blunt, M. O.; Iritani, K.; De Feyter, S.; Tobe, Y., Functionalized Surface-Confined Pores: Guest Binding Directed by Lateral Noncovalent Interactions at the Solid-Liquid Interface. *ACS Nano* **2014**, *8* (8), 8683-8694.
127. Ma, J.; Alfe, D.; Michaelides, A.; Wang, E., Stone-Wales defects in graphene and other planar sp²-bonded materials. *Phys. Rev. B* **2009**, *80* (3), 033407.
128. Kurasch, S.; Kotakoski, J.; Lehtinen, O.; Skákalová, V.; Smet, J.; Krill III, C. E.; Krasheninnikov, A. V.; Kaiser, U., Atom-by-atom observation of grain boundary migration in graphene. *Nano Lett.* **2012**, *12* (6), 3168-3173.
129. MacLeod, J.; Rosei, F., Molecular Self-Assembly on Graphene. *Small* **2014**, *10* (6), 1038-1049.
130. Cockayne, E.; Rutter, G. M.; Guisinger, N. P.; Crain, J. N.; First, P. N.; Stroscio, J. A., Grain boundary loops in graphene. *Phys. Rev. B* **2011**, *83* (19), 195425.
131. Xu, L.; Zhou, X.; Tian, W. Q.; Gao, T.; Zhang, Y. F.; Lei, S.; Liu, Z. F., Surface-Confined Single-Layer Covalent Organic Framework on Single-Layer Graphene Grown on Copper Foil. *Angew. Chem.* **2014**, *53*, 9564-9568.
132. Gutzler, R.; Ivasenko, O.; Fu, C.; Brusso, J. L.; Rosei, F.; Perepichka, D. F., Halogen bonds as stabilizing interactions in a chiral self-assembled molecular monolayer. *Chem. Commun.* **2011**, *47* (33), 9453-9455.
133. Gatti, R.; MacLeod, J. M.; Lipton-Duffin, J. A.; Moiseev, A. G.; Perepichka, D. F.; Rosei, F., Substrate, Molecular Structure, and Solvent Effects in 2D Self-Assembly via Hydrogen and Halogen Bonding. *J. Phys. Chem. C* **2014**, *118* (44), 25505-25516.

134. Gutiérrez, I. S.; Lin, F.-Y.; Vanommeslaeghe, K.; Lemkul, J. A.; Armacost, K. A.; Brooks, C. L.; MacKerell, A. D., Parametrization of halogen bonds in the CHARMM general force field: Improved treatment of ligand–protein interactions. *Bioorgan. Med. Chem.* **2016**, *24* (20), 4812-4825.
135. Cavallo, G.; Metrangolo, P.; Milani, R.; Pilati, T.; Priimagi, A.; Resnati, G.; Terraneo, G., The halogen bond. *Chem. Rev.* **2016**, *116* (4), 2478-2601.
136. Lackinger, M.; Griessl, S.; Kampschulte, L.; Jamitzky, F.; Heckl, W. M., Dynamics of Grain Boundaries in Two-Dimensional Hydrogen-Bonded Molecular Networks. *Small* **2005**, *1* (5), 532-539.
137. Gutzler, R.; Lappe, S.; Mahata, K.; Schmittel, M.; Heckl, W. M.; Lackinger, M., Aromatic interaction vs. hydrogen bonding in self-assembly at the liquid–solid interface. *Chem. Commun.* **2009**, (6), 680-682.
138. Frisch, M. J.; Trucks, G. W.; Schlegel, H. B.; Scuseria, G. E.; Robb, M. A.; Cheeseman, J. R.; Scalmani, G.; Barone, V.; Mennucci, B.; Petersson, G. A.; Nakatsuji, H.; Caricato, M.; Li, X.; Hratchian, H. P.; Izmaylov, A. F.; Bloino, J.; Zheng, G.; Sonnenberg, J. L.; Hada, M.; Ehara, M.; Toyota, K.; Fukuda, R.; Hasegawa, J.; Ishida, M.; Nakajima, T.; Honda, Y.; Kitao, O.; Nakai, H.; Vreven, T.; Montgomery, J. A.; Peralta, J. E.; Ogliaro, F.; Bearpark, M.; Heyd, J. J.; Brothers, E.; Kudin, K. N.; Staroverov, V. N.; Kobayashi, R.; Normand, J.; Raghavachari, K.; Rendell, A.; Burant, J. C.; Iyengar, S. S.; Tomasi, J.; Cossi, M.; Rega, N.; Millam, J. M.; Klene, M.; Knox, J. E.; Cross, J. B.; Bakken, V.; Adamo, C.; Jaramillo, J.; Gomperts, R.; Stratmann, R. E.; Yazyev, O.; Austin, A. J.; Cammi, R.; Pomelli, C.; Ochterski, J. W.; Martin, R. L.; Morokuma, K.; Zakrzewski, V. G.; Voth, G. A.; Salvador, P.; Dannenberg, J. J.; Dapprich, S.; Daniels, A. D.; Farkas; Foresman, J. B.; Ortiz, J. V.; Cioslowski, J.; Fox, D. J., *Gaussian 09, Revision B.01*. Wallingford CT, **2009**.
139. Zhao, Y.; Truhlar, D. G., The M06 suite of density functionals for main group thermochemistry, thermochemical kinetics, noncovalent interactions, excited states, and transition elements: two new functionals and systematic testing of four M06-class functionals and 12 other functionals. *Theor. Chem. Acc.* **2008**, *120* (1), 215-241.
140. Bondi, A., van der Waals volumes and radii. *J. Phys. Chem.* **1964**, *68* (3), 441-451.
141. Li, H.; Giri, G.; Tok, J. B.-H.; Bao, Z., Toward high-mobility organic field-effect transistors: Control of molecular packing and large-area fabrication of single-crystal-based devices. *MRS bull.* **2013**, *38* (01), 34-42.
142. Kwon, O.-P.; Jazbinsek, M.; Yun, H.; Seo, J.-I.; Kim, E.-M.; Lee, Y.-S.; Günter, P., Pyrrole-based hydrazone organic nonlinear optical crystals and their polymorphs. *Cryst. Growth Des.* **2008**, *8* (11), 4021-4025.
143. Rodríguez-Spong, B.; Price, C. P.; Jayasankar, A.; Matzger, A. J.; Rodríguez-Hornedo, N. r., General principles of pharmaceutical solid polymorphism: a supramolecular perspective. *Adv. Drug Deliver Rev.* **2004**, *56* (3), 241-274.
144. Bernardes, C. E.; Lopes, M. L. M.; Ascenso, J. R.; da Piedade, M. E. M., From molecules to crystals: the solvent plays an active role throughout the nucleation pathway of molecular organic crystals. *Cryst. Growth Des.* **2014**, *14* (11), 5436-5441.

145. Chen, J.; Trout, B. L., Computational study of solvent effects on the molecular self-assembly of tetrolic acid in solution and implications for the polymorph formed from crystallization. *J. Phys. Chem. B* **2008**, *112* (26), 7794-7802.
146. Hiremath, R.; Basile, J. A.; Varney, S. W.; Swift, J. A., Controlling molecular crystal polymorphism with self-assembled monolayer templates. *J. Am. Chem. Soc.* **2005**, *127* (51), 18321-18327.
147. Cicoira, F.; Rosei, F., Playing Tetris at the nanoscale. *Surf. Sci.* **2006**, *600* (1), 1-5.
148. Ahn, S.; Matzger, A. J., Additive perturbed molecular assembly in two-dimensional crystals: differentiating kinetic and thermodynamic pathways. *J. Am. Chem. Soc.* **2012**, *134* (6), 3208-3214.
149. Lu, B.; Iimori, T.; Sakamoto, K.; Nakatsuji, K.; Rosei, F.; Komori, F., Fullerene on nitrogen-adsorbed Cu (001) nanopatterned surfaces: From preferential nucleation to layer-by-layer growth. *J. Phys. Chem. C* **2008**, *112* (27), 10187-10192.
150. Koepf, M.; Chérioux, F.; Wytko, J. A.; Weiss, J., 1D and 3D surface-assisted self-organization. *Coordin. Chem. Rev.* **2012**, *256* (23), 2872-2892.
151. Yang, J.; Yan, D.; Jones, T. S., Molecular template growth and its applications in organic electronics and optoelectronics. *Chem. Rev.* **2015**, *115* (11), 5570-5603.
152. Aizenberg, J.; Black, A. J.; Whitesides, G. M., Control of crystal nucleation by patterned self-assembled monolayers. *Nature* **1999**, *398* (6727), 495-498.
153. Fu, C.; Lin, H.-p.; Macleod, J. M.; Krayev, A.; Rosei, F.; Perepichka, D. F., Unravelling the self-assembly of hydrogen bonded NDI semiconductors in 2D and 3D. *Chem. Mater.* **2016**, *28* (3), 951-961.
154. Beton, P.; Korolkov, V.; Taniguchi, T.; Baldoni, M.; Watanabe, K.; Besley, E., Supramolecular heterostructures formed by sequential epitaxial deposition of two-dimensional hydrogen-bonded arrays. *Nat. Chem.* **2017**, *9*, 1191-1197.
155. Li, J.; Wieghold, S.; Öner, M. A.; Simon, P.; Hauf, M. V.; Margapoti, E.; Garrido, J. A.; Esch, F.; Palma, C.-A.; Barth, J. V., Three-dimensional bicomponent supramolecular nanoporous self-assembly on a hybrid all-carbon atomically flat and transparent platform. *Nano Lett.* **2014**, *14* (8), 4486-4492.
156. De Feyter, S., Surface patterning: From 2D to 3D. *Nat. Chem.* **2011**, *3* (1), 14-15.
157. Mezour, M. A.; Choueiri, R. M.; Lukyanova, O.; Lennox, R. B.; Perepichka, D. F., Hydrogen bonding vs. molecule–surface interactions in 2D self-assembly of [C₆₀] fullerene-carboxylic acids. *Nanoscale* **2016**, *8* (38), 16955-16962.
158. Samorí, P.; Severin, N.; Simpson, C. D.; Müllen, K.; Rabe, J. P., Epitaxial composite layers of electron donors and acceptors from very large polycyclic aromatic hydrocarbons. *J. Am. Chem. Soc.* **2002**, *124* (32), 9454-9457.
159. Mamdouh, W.; Uji-i, H.; Ladislaw, J. S.; Dulcey, A. E.; Percec, V.; De Schryver, F. C.; De Feyter, S., Solvent controlled self-assembly at the liquid-solid interface revealed by STM. *J. Am. Chem. Soc.* **2006**, *128* (1), 317-325.
160. Sirtl, T.; Song, W.; Eder, G.; Neogi, S.; Schmittel, M.; Heckl, W. M.; Lackinger, M., Solvent-dependent stabilization of metastable monolayer polymorphs at the liquid–solid interface. *ACS Nano* **2013**, *7* (8), 6711-6718.
161. Nangia, A.; Desiraju, G. R., Pseudopolymorphism: occurrences of hydrogen bonding organic solvents in molecular crystals. *Chem. Commun.* **1999**, (7), 605-606.

162. Gutzler, R.; Cardenas, L.; Rosei, F., Kinetics and thermodynamics in surface-confined molecular self-assembly. *Chem. Sci.* **2011**, *2* (12), 2290-2300.
163. Jäckel, F.; Ai, M.; Wu, J.; Müllen, K.; Rabe, J. P., Solvent molecules in an epitaxially grown scaffold of star-shaped nanographenes. *J. Am. Chem. Soc.* **2005**, *127* (42), 14580-14581.
164. Kim, K.; Lee, T. H.; Santos, E. J.; Jo, P. S.; Salleo, A.; Nishi, Y.; Bao, Z., Structural and Electrical Investigation of C₆₀–Graphene Vertical Heterostructures. *ACS Nano* **2015**, *9* (6), 5922-5928.
165. Rey, C.; Garcia-Rodeja, J.; Gallego, L.; Alonso, J., Clusters and layers of C₆₀ molecules supported on a graphite substrate. *Phys. Rev. B* **1997**, *55* (11), 7190.
166. Kitaigorodskii, A., The principle of close packing and the condition of thermodynamic stability of organic crystals. *Acta Crystallogr.* **1965**, *18* (4), 585-590.
167. Jung, J.; Raoux, A.; Qiao, Z.; MacDonald, A. H., Ab initio theory of moiré superlattice bands in layered two-dimensional materials. *Phys. Rev. B* **2014**, *89* (20), 205414.
168. Abdurakhmanova, N.; Floris, A.; Tseng, T.-C.; Comisso, A.; Stepanow, S.; De Vita, A.; Kern, K., Stereoselectivity and electrostatics in charge-transfer Mn-and Cs-TCNQ4 networks on Ag (100). *Nat. Commun.* **2012**, *3*, 940.
169. Jin, J.; Song, X.; Wang, Z.; Liu, X.; Wang, L., Self-organized patterns of fullerene on molecular nanotemplate. *J. Appl. Phys.* **2017**, *121* (5), 054305.
170. Mezour, M. A.; Voznyy, O.; Sargent, E. H.; Lennox, R. B.; Perepichka, D. F., Controlling C₆₀ organization through dipole-induced band alignment at self-assembled monolayer interfaces. *Chem.Mater.* **2016**, *28* (22), 8322-8329.
171. Gyarfás, B. J.; Wiggins, B.; Zosel, M.; Hipps, K., Supramolecular Structures of Coronene and Alkane Acids at the Au (111)– Solution Interface: A Scanning Tunneling Microscopy Study. *Langmuir* **2005**, *21* (3), 919-923.
172. Zhang, S.; Zhang, J.; Deng, K.; Xie, J.; Duan, W.; Zeng, Q., Solution concentration controlled self-assembling structure with host–guest recognition at the liquid–solid interface. *Phys. Chem. Chem. Phys.* **2015**, *17* (37), 24462-24467.
173. Tahara, K.; Furukawa, S.; Uji-i, H.; Uchino, T.; Ichikawa, T.; Zhang, J.; Mamdouh, W.; Sonoda, M.; De Schryver, F. C.; De Feyter, S., Two-dimensional porous molecular networks of dehydrobenzo [12] annulene derivatives via alkyl chain interdigitation. *J. Am. Chem. Soc.* **2006**, *128* (51), 16613-16625.
174. Shin, H. S.; Yoon, S. M.; Tang, Q.; Chon, B.; Joo, T.; Choi, H. C., Highly selective synthesis of C₆₀ disks on graphite substrate by a vapor–solid process. *Angew. Chem. Int. Edit.* **2008**, *47* (4), 693-696.
175. Suto, S.; Kasuya, A.; Hu, C.-W.; Wawro, A.; Sakamoto, K.; Goto, T.; Nishina, Y., Initial stage of C₆₀ film growth and reaction on Si (111) 7× 7 and graphite surfaces studied by HREELS–STM. *Thin Solid Films* **1996**, *281*, 602-605.
176. Reinke, P.; Feldermann, H.; Oelhafen, P., C₆₀ bonding to graphite and boron nitride surfaces. *J. Chem. Phys.* **2003**, *119* (23), 12547-12552.
177. Shin, H.; O'Donnell, S.; Reinke, P.; Ferralis, N.; Schmid, A.; Li, H.; Novaco, A. D.; Bruch, L.; Diehl, R., Floating two-dimensional solid monolayer of C₆₀ on graphite. *Phys. Rev. B* **2010**, *82* (23), 235427.
178. Liu, H.; Lin, Z.; Zhigilei, L. V.; Reinke, P., Fractal structures in fullerene layers: simulation of the growth process. *J. Phys. Chem. C* **2008**, *112* (12), 4687-4695.

179. Liu, H.; Reinke, P., C₆₀ thin film growth on graphite: Coexistence of spherical and fractal-dendritic islands. *J. Chem. Phys.* **2006**, *124* (16), 164707-164707.
180. Kenny, D.; Palmer, R., Nucleation and growth of C₆₀ thin films on graphite. *Surf. Sci.* **2000**, *447* (1), 126-132.
181. Luo, M.; Li, Z.; Allison, W., Initial stages of C₆₀ thin film growth on graphite. *Surf. Sci.* **1998**, *402*, 437-440.
182. Sato, K.; Tanaka, T.; Akaike, K.; Kanai, K., Morphological phase diagrams of C₆₀ and C₇₀ films on graphite. *Surf. Sci.* **2017**, *664*, 222-225.
183. Szuba, S.; Czajka, R.; Kasuya, A.; Wawro, A.; Rafii-Tabar, H., Observation of C₆₀ film formation on a highly oriented pyrolytic graphite substrate via scanning tunnelling microscopy. *Appl. Surf. Sci.* **1999**, *144*, 648-652.
184. Li, Z., Orientational order of ultrathin C₆₀ films on graphite. *Surf. Sci.* **1999**, *441* (2), 366-372.
185. Davey, R.; Blagden, N.; Potts, G.; Docherty, R., Polymorphism in molecular crystals: stabilization of a metastable form by conformational mimicry. *J. Am. Chem. Soc.* **1997**, *119* (7), 1767-1772.
186. Semenov, K. N.; Charykov, N. A.; Keskinov, V. A.; Piartman, A. K.; Blokhin, A. A.; Kopyrin, A. A., Solubility of light fullerenes in organic solvents. *J. Chem. Eng. Data* **2009**, *55* (1), 13-36.
187. Evans, J.; Thiel, P.; Bartelt, M. C., Morphological evolution during epitaxial thin film growth: Formation of 2D islands and 3D mounds. *Surf. Sci. Rep.* **2006**, *61* (1), 1-128.
188. Vekilov, P. G., What determines the rate of growth of crystals from solution? *Cryst. Growth Des.* **2007**, *7* (12), 2796-2810.
189. Baker, R. T.; Mougous, J. D.; Brackley, A.; Patrick, D. L., Competitive Adsorption, Phase Segregation, and Molecular Motion at a Solid– Liquid Interface Studied by Scanning Tunneling Microscopy. *Langmuir* **1999**, *15* (14), 4884-4891.
190. Nečas, D.; Klapetek, P., Gwyddion: an open-source software for SPM data analysis. *Open Physics* **2012**, *10* (1), 181-188.
191. dos Santos, J. L.; Peres, N.; Neto, A. C., Continuum model of the twisted graphene bilayer. *Phys. Rev. B* **2012**, *86* (15), 155449.
192. Kresse, G.; Hafner, J., Ab initio molecular dynamics for liquid metals. *Phys. Rev. B* **1993**, *47* (1), 558.
193. Kresse, G.; Furthmüller, J., Efficient iterative schemes for ab initio total-energy calculations using a plane-wave basis set. *Phys. Rev. B* **1996**, *54* (16), 11169.
194. Loken, C.; Gruner, D.; Groer, L.; Peltier, R.; Bunn, N.; Craig, M.; Henriques, T.; Dempsey, J.; Yu, C.-H.; Chen, J. In *SciNet: lessons learned from building a power-efficient top-20 system and data centre*, *J. Phys. Conf. Ser.* **2010**, *256*, 012026.
195. Perdew, J. P.; Ernzerhof, M.; Burke, K., Rationale for mixing exact exchange with density functional approximations. *J. Chem. Phys.* **1996**, *105* (22), 9982-9985.
196. Blöchl, P. E., Projector augmented-wave method. *Phys. Rev. B* **1994**, *50* (24), 17953.
197. Kresse, G.; Joubert, D., From ultrasoft pseudopotentials to the projector augmented-wave method. *Phys. Rev. B* **1999**, *59* (3), 1758.
198. Grimme, S., Semiempirical GGA-type density functional constructed with a long-range dispersion correction. *J. Comput. Chem.* **2006**, *27* (15), 1787-1799.

199. Grimme, S.; Antony, J.; Ehrlich, S.; Krieg, H., A consistent and accurate ab initio parametrization of density functional dispersion correction (DFT-D) for the 94 elements H-Pu. *J. Chem. Phys.* **2010**, *132* (15), 154104.
200. Henkelman, G.; Arnaldsson, A.; Jónsson, H., A fast and robust algorithm for Bader decomposition of charge density. *Comp. Mater. Sci.* **2006**, *36* (3), 354-360.
201. Sanville, E.; Kenny, S. D.; Smith, R.; Henkelman, G., Improved grid-based algorithm for Bader charge allocation. *J. Comput. Chem.* **2007**, *28* (5), 899-908.
202. Tang, W.; Sanville, E.; Henkelman, G., A grid-based Bader analysis algorithm without lattice bias. *J. Phys. Condens. Mat.* **2009**, *21* (8), 084204.
203. Yu, M.; Trinkle, D. R., Accurate and efficient algorithm for Bader charge integration. *J. Chem. Phys.* **2011**, *134* (6), 064111.
204. Yethiraj, A.; van Blaaderen, A., A colloidal model system with an interaction tunable from hard sphere to soft and dipolar. *Nature* **2003**, *421* (6922), 513.
205. Compagnon, I.; Antoine, R.; Broyer, M.; Dugourd, P.; Lermé, J.; Rayane, D., Electric polarizability of isolated C 70 molecules. *Phys. Rev. A* **2001**, *64* (2), 025201.
206. Lu, J.; Lei, S.-b.; Zeng, Q.-d.; Kang, S.-z.; Wang, C.; Wan, L.-j.; Bai, C.-l., Template-induced inclusion structures with copper (II) phthalocyanine and coronene as guests in two-dimensional hydrogen-bonded host networks. *J. Phys. Chem. B* **2004**, *108* (17), 5161-5165.
207. Schull, G.; Douillard, L.; Fiorini-Debuisschert, C.; Charra, F.; Mathevet, F.; Kreher, D.; Attias, A.-J., Single-molecule dynamics in a self-assembled 2D molecular sieve. *Nano Lett.* **2006**, *6* (7), 1360-1363.
208. Xiao, W.; Passerone, D.; Ruffieux, P.; Aït-Mansour, K.; Gröning, O.; Tosatti, E.; Siegel, J. S.; Fasel, R., C60/corannulene on Cu (110): a surface-supported bistable buckyowl-buckyball host-guest system. *J. Am. Chem. Soc.* **2008**, *130* (14), 4767-4771.